

5-2013

Investigation of Perforated Ducted Propellers to use with a UAV

Krishna Regmi

Follow this and additional works at: https://scholarworks.uno.edu/honors_theses

Recommended Citation

Regmi, Krishna, "Investigation of Perforated Ducted Propellers to use with a UAV" (2013). *Senior Honors Theses*. 45.

https://scholarworks.uno.edu/honors_theses/45

This Honors Thesis-Unrestricted is protected by copyright and/or related rights. It has been brought to you by ScholarWorks@UNO with permission from the rights-holder(s). You are free to use this Honors Thesis-Unrestricted in any way that is permitted by the copyright and related rights legislation that applies to your use. For other uses you need to obtain permission from the rights-holder(s) directly, unless additional rights are indicated by a Creative Commons license in the record and/or on the work itself.

This Honors Thesis-Unrestricted has been accepted for inclusion in Senior Honors Theses by an authorized administrator of ScholarWorks@UNO. For more information, please contact scholarworks@uno.edu.

Investigation of Perforated Ducted Propellers to use with a UAV

An Honors Thesis

Presented to

the Department of Mechanical Engineering

of the University of New Orleans

In Partial Fulfillment

Of the Requirements for the Degree of

Bachelor of Science, with University Honors

And Honors in Mechanical Engineering

by

Krishna Regmi

May 2013

Acknowledgement

I would like to thank my advisor, Professor Ting Wang, for his continuous support throughout this year. Also thanks to Professor Martin Guillot for reading the thesis and providing me with valuable feedback. I would like to thank the Honors Department for creating this opportunity to perform independent research. It was one of the most valuable experiences in my undergraduate career. This acknowledgement wouldn't be complete if I didn't thank graduate students of Dr. Ting Wang, especially Scott Richard for all his editorial support and advice, Xijia Lu for help with ICEM and Fluent, Henry Long for support with computer setup, and Rada Ragab for his excellent feedback during the midterm and end of semester presentations.

CONTENTS

CONTENTS.....	iii
ABSTRACT.....	viii
Chapter 1 : INTRODUCTION	1
History of small UAVs.....	2
Classification of UAVs	3
Fixed Wing UAVs.....	4
Rotorcraft UAVs.....	8
Flapping Wing UAVs.....	12
Unconventional UAV:.....	14
Ducted fan.....	15
Motivation	18
Objectives	19
Approach.....	19
Chapter 2 : SOFTWARE TRAINING	20
Case 1: Laminar Channel Flow	20
Case 2: Laminar Pipe Flow with a constant heat flux at the surface	23
Chapter 3 : THEORY.....	26
Formulation of Momentum Equation:.....	26
Modified Thrust Coefficient.....	31
Efficiency of Duct	31
Navier-Stokes Equations	32
Chapter 4 : MODELING AND SIMULATION OF AIRFLOW	34
3-D propeller to 2-D Disc	34
Infinite Domain to Finite Domain	35
Sensitivity of the size of control volume:.....	37
Wall Functions	39
Pressure inlet/outlet Boundary Conditions:	39
Choosing Pressure Difference.....	41
Choosing Overall Dimensions	42
Perforations	43
Verification of Symmetry: 2-D Modeling.....	46
Axisymmetrical Modeling	48
Grid Independent Study.....	48

Chapter 5 : RESULTS, DISCUSSIONS AND CONCLUSIONS	50
Case 1: 2-D Duct with no Perforation	50
2-D Duct with 4 Perforations	53
2-D Duct with 6 Pores:	57
8-Perforations	59
Results.....	60
Conclusions:	69
BIBLIOGRAPHY	71
Chapter 6 : APPENDICES	74
Appendix I: Different Cases.....	74
Part 1: Laminar Channel Flow	78
Part 2.1: Steady, Laminar Flow in Circular Tubes and no Heat source.	93
Nusselt’s Number.....	105
Part 3: Turbulent Pipe Flow with Constant Temperature on the walls	110

List of Figures

Figure 1-1: Incredible HLQ Quad rotor (Nick, 2013)	1
Figure 1-2 PARS Aerial Rescue Bot (Solon, 2013)	2
Figure 1-3 Lockheed RX-170 Sentinel (The Muslim Observer, 2010)	5
Figure 1-4 NASA Pathfinder (Galante, 2001)	6
Figure 1-5 Theory of Fixed Winged UAV (MIT, 1997)	6
Figure 1-6 Full Sized helicopter UAV called Hummingbird (Trimble, 2009)	9
Figure 1-7 Miniature Quadcopter (Joblin, 2010)	9
Figure 1-8 Actuator Disc Theory (Seddon and Newman, 2011)	10
Figure 1-9 Festo Smart-Bird (robot bird, 2011)	12
Figure 1-10 Robot Bird (Airforce, 2012).....	13
Figure 1-11 UAV that uses helium and Inversion technology to fly (Forman, 2012).....	14
Figure 1-12 Examples of un-ducted and ducted propellers, and a perforated duct	16
Figure 1-13: Thrust coefficient vs. Rotor RPM from an experiment done by NASA (Martin, 2004)	17
Figure 2-1 Problem Statement for Laminar channel flow	20
Figure 2-2 x-velocity vs. y-coordinate for laminar channel flow.....	21
Figure 2-3 skin Friction coefficient for laminar channel flow	22
Figure 2-4 Problem Statement for Laminar Pipe flow with a constant heat flux	23
Figure 2-5 Ideal velocity vs. velocity profile obtained from fluent	24
Figure 2-6 skin friction coefficient vs x-coordinate.....	24
Figure 2-7 Development of Dimensionless Temperature profile	25
Figure 2-8 Variation of Nusselt's number with x-coordinate.....	25
Figure 3-1: Conservation of momentum.....	28
Figure 3-2 Forces in x-direction in an infinitesimally small, moving fluid element (Anderson CFD)	32
Figure 4-1 Actuator Disc Theory (Scott, 2011).....	35
Figure 4-2 Case 1 - Pressure boundary conditions	40
Figure 4-3 Case 2 - Pressure boundary conditions	40
Figure 4-4 Case 3 - Pressure boundary conditions	41
Figure 4-5: 3-D Translation of an axis-symmetrical plane with 4 Pores	44
Figure 4-6: 2-D Duct with four Pores	45
Figure 4-7: Contours of Static Pressure in a 2-D model.....	47
Figure 4-8: Contours of velocity magnitude in a 2-D model	47
Figure 4-9: Axisymmetrical modeling.....	48
Figure 5-1 Case 1: Duct with no perforations - velocity vectors overlaid on pressure contour	51
Figure 5-2 Recirculation near tip gap.....	52
Figure 5-3 Contours of Static pressure - case 2	53
Figure 5-4 velocity vectors - case 1.....	54
Figure 5-5 velocity vectors superimposed on pressure contour - case 1	55
Figure 5-6 Closer look at the velocity vectors superimposed on pressure contour - case 2	56
Figure 5-7 Case 3 - velocity vectors on pressure contour.....	57
Figure 5-8 case 3: closer look inside the duct.....	58
Figure 5-9 case 4 Duct Area	59
Figure 5-10 Case 4 - closer look inside the duct	60
Figure 5-11 variation of net Thrust with % of open area in the duct for cases with 6000 Pa after duct weight is subtracted from the thrust.....	64
Figure 5-12 variation of net Thrust with % of Open Area for cases with 3000 Pa after duct weight is subtracted from the thrust	65

Figure 5-13 Variation of net Thrust with % of Open Area for cases with 60 Pa after duct weight is subtracted from the thrust	66
Figure 5-14: Thrust Coefficient vs Open Area %	67
Figure 5-15: Different types of Duct Shape (Wright Jr and Piolene 2002)	68
Figure 6-1 Duct with no Pores.....	75
Figure 6-2: Duct with four 0.1" Pores	75
Figure 6-3 Duct with six 0.1" Diameter Pores	75
Figure 6-4 Eight 0.1" Diameter Pores.....	75
Figure 6-5: Duct with four 0.3" Pores	76
Figure 6-6: Duct with four 0.3" Pores	76
Figure 6-7 Duct with six 0.3" Pores.....	76
Figure 6-8 Duct with Eight 0.3" Diameter Pores	76
Figure 6-9 Duct with four 0.5" Pores	77
Figure 6-10 Duct with six 0.5" Pores.....	77
Figure 6-11: Duct with eight 0.5" Diameter Pores	77
Figure 6-12 Propeller with no duct	77
Figure 6-13: Channel Flow with Boundary Conditions at T=20°C.....	78
Figure 6-14: Channel geometry to calculate the velocity profile.....	80
Figure 6-15: Channel Flow with Boundary Conditions	83
Figure 6-16 : Approximate shape of converging Boundary Layers.	84
Figure 6-17 :The velocity Profile develops into parabolic velocity profile.....	85
Figure 6-18: Comparison of Ideal velocity profile vs. the velocity profile from Fluent	86
Figure 6-19 : Skin friction-coefficient.....	86
Figure 6-20 : Channel Flow with Boundary Conditions.....	87
Figure 6-21 : Development of flow.	87
Figure 6-22 : Velocity profiles at different locations for a channel flow	88
Figure 6-23 : Comparison of theoretical velocity profile with the one from Fluent.....	89
Figure 6-24 : Skin Friction Coefficient.....	89
Figure 6-25 : A close look at the skin friction coefficient.....	90
Figure 6-26 : Comparison with Ideal case for velocity profile	91
Figure 6-27 : Skin Friction Coefficient of $f = 0.057$ was found.	92
Figure 6-28 : Channel Flow with Boundary Conditions.....	93
Figure 6-29 : Solution with only 500 elements	97
Figure 6-30 : Results from refined mesh.....	98
Figure 6-31 : Velocity Profile at inlet, exit and at $x=2m$	100
Figure 6-32 : Comparison of velocity Profile at $x=2m$ with the Ideal velocity profile.....	100
Figure 6-33 : Channel Flow with Boundary Conditions.....	101
Figure 6-34 : Pipe Flow meshing	102
Figure 6-35 : Comparison of Ideal vs. Fluent's velocity Profile.....	103
Figure 6-36 : Increasing Temperature.....	104
Figure 6-37 : Temperature Profiles.....	105
Figure 6-38 : Skin friction coefficient with Axial Coordinate	106
Figure 6-39 : Channel Flow with Boundary Conditions.....	107
Figure 6-40 : Development of velocity profile	107
Figure 6-41 : Comparison of ideal vs. Fluent's velocity profile.	108
Figure 6-42 : Skin Friction Coefficient of 0.0392	108
Figure 6-43 : Thermal Profile Developing	109
Figure 6-44 : Developing profile for Dimensionless Temperature.....	109

Figure 6-45 : Variation of surface Nusselt's number with the distance from the entrance.	110
Figure 6-46 : Pipe Flow with Boundary Conditions.....	111
Figure 6-47 : Comparison of velocity profile in laminar and turbulent flow.	114
Figure 6-48 : Velocity Profiles of a turbulent Flow	116
Figure 6-49: variation of Skin Friction Coefficient in turbulent flow	116

ABSTRACT

Unmanned Aerial Vehicle (UAV) is any flying vehicle which is not controlled by actual human pilots sitting in the cockpit but is installed with proper avionics that can either fly autonomously or by using the commands from its base. Some rotorcraft UAVs use a ducted propeller for two main reasons- safety and to increase the thrust produced by the propellers. While ducted rotors can increase the thrust produced, it also adds weight to the UAV. It was therefore hypothesized that by removing part of the duct materials (i.e. adding perforations in the duct) would benefit from both decreased duct weight and increased thrust. However, it is not clear how much trade-off would be between these two factors. Hence, the objective of this study is to explore the relationship between the change of thrust and addition of different numbers or sizes of perforations. Cases with and without duct, and duct with perforations were simulated using a commercial computational fluid dynamic (CFD) software Ansys/Fluent. The physics of the rotating propeller was modeled by a simplified disc with a pressure jump across an infinitesimal volume. Three different RPM speeds of the propellers were simulated by varying the strength of the pressure jump. The results show that the thrust decreases as the duct is added. As perforations are added, the result shows that with more perforations (i.e. more open area on the duct wall), the thrust increases accordingly until the thrust reaches a maximum value without the duct. The result is in contrast to a published experimental data stating that installation of duct can increase thrust. It is speculated that the current duct with a flat wall has caused such difference from the experimental data. Further study is recommended to continue more detailed computational simulation using a duct with cambered airfoil configuration to reduce the aerodynamic losses.

Keywords: UAV, Duct, Ducted propeller, rotor, propeller, CFD, perforations, computational simulation.

Chapter 1 : INTRODUCTION

Unmanned Aerial Vehicle (UAV) is any flying vehicle which is not controlled by actual human pilots sitting in the cockpit but is installed with proper avionics that can either fly autonomously or by using the commands from its base. A small UAV is defined as a UAV small enough to be portable by one person. UAV's can be very useful for tasks such as military reconnaissance, surveillance of a hazardous environment, information gathering in emergencies and also for providing assistance in emergencies. Small UAV's can also be used for entertainment industry such as aerial filming, aerial photography etc. as well.

One of the examples of a UAVs designed to assist in an emergencies is Incredible HLQ (pronounced Incredible hulk) Quad rotor. This UAV is currently being developed at San Hose University to deliver and retrieve medical supplies of up to 50 lbs. to the locations needing immediate medical supplies (Nick, 2013).



Figure 1-1: Incredible HLQ Quad rotor (Nick, 2013)

Another great example of how these UAVs can be used in rescue mission is Iranian lifeguard quad rotor called The Pars Aerial Rescue Bot. It is developed by RTS Labs, which is an Iranian research firm. The UAV is used to attend to people drowning or in difficulty in the ocean (Solon 2013). It is being designed to be able to carry up to 15 self-inflating rings that can be dispensed as needed.



Figure 1-2 PARS Aerial Rescue Bot (Solon, 2013)

History of small UAVs

The study of small Unmanned Aerial Vehicles known as UAVs became prominent among scientists in the early 1990s. In 1992, DARPA (Defense Advanced Research Projects) held a workshop, among which study of miniature robots was one of the major topics (Tzafestas

2007). By 1996, Lincoln research lab in MIT (Massachusetts Institute of Technology) was already developing small UAVs. DARPA first defined small/miniature UAVs as the ones that have 15-cm or less wing span. After a few years of initial research, DARPA stopped funding its MUAV programs because the weight to power stored ratios of the batteries is not enough for a useful flight.

In early 2000s, after Integrated Circuits started to be available easily and cheaply, hobbyists have been doing a lot of independent work in the field of hobby aerial vehicles, mainly aero-plane style toys and helicopter style toys. The payload capacity of most of these aircrafts are still limited to less than a kilogram and the flight endurance is very low, around 5-10 minutes on average in battery operated vehicles.

This study will focus on rotorcrafts that are small enough for a person to carry; called small UAVs hereafter.

Classification of UAVs

UAVs can be classified by two methods: namely based on the size of the total aircraft and the propulsion system the aircraft uses. The two different types of classifications are briefly discussed below:

UAVs can be classified into three category based on their total size:

- Miniature UAVs: DARPA has defined miniature UAVs as the ones that are smaller than 15 cm in all dimensions.
- Small UAVs: Small UAVs are those UAVs that are small enough for a man to carry it.
- Large UAVs: Large UAVs are those that are bigger than small UAVs i.e. they cannot be carried by a person. Large UAVs are mostly used by the military for military reconnaissance and remotely controlled attacks.

UAV's can be made to fly by using various methods. Author Ben Chen has classified UAVs into four different categories based on the propulsion system they use:

- Fixed Wing UAVs
- Rotorcraft UAVs
- Flapping Wing UAVs
- Unconventional UAVs

The different types of UAVs will be explained and discussed in details below.

Fixed Wing UAVs

Fixed wing UAVs are the most common type of UAVs used for military purposes. They are categorized by the presence of fixed wings. Fixed winged UAVs can be extremely sophisticated and have very long endurance in some cases. The development of fixed wing UAVs was accelerated by the technology from already existing commercial aircrafts. Typically a fixed winged UAV has an engine that provides thrust in the forward direction, and large wings that provide lift.

An example of a fixed wing UAV would be the Lockheed RX-170 Sentinel (Figure 4.1).



Figure 1-3 Lockheed RX-170 Sentinel (The Muslim Observer, 2010)

Although details of military aircraft such as RX-170 are not released for the public audience, it is supposed to be a stealth aircraft used for military reconnaissance. According to the website theatlantic.com, this UAV was used to gather intelligence about the location of Bin Laden. One of the RX-170s was captured by Iranian army in 2011, exposing the little known information about the UAV. RX-170 has wingspan of about 27 meters.

Another equally fascinating example of fixed winged aircraft is the pathfinder used by NASA.



Figure 1-4 NASA Pathfinder (Galante, 2001)

It uses solar energy to charge onboard batteries to operate its flight and avionics. It was developed by NASA to use as a high altitude/high endurance vehicle for environmental research. Its wingspan is 29 meters (NASA n.d.)

Theory behind Fixed Wing UAV:

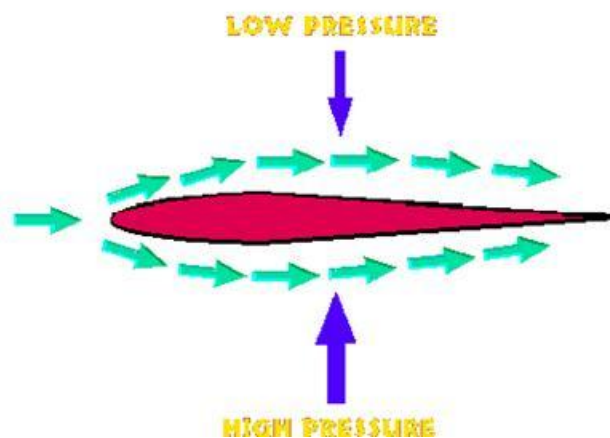


Figure 1-5 Theory of Fixed Winged UAV (MIT, 1997)

Fixed winged aircraft make use of the difference in pressure created by the camber in the airfoil (wing). Bernoulli's equation states that

$$P + \frac{1}{2}\rho V^2 = \text{Constant}$$

(1)

And Continuity Equation states that

$$\rho AV = \text{Constant}$$

(2)

Where,

P=pressure

P= density of the air

V=velocity of the moving air

A= cross sectional area of flow

The surface area of the top of the airfoil is greater than the bottom. When the air flows over the airflow, assuming the density of the air remains unchanged, the air on the top of the wing moves faster than the air on the bottom (by Continuity). Since the velocity of the air is greater on the top, the pressure has to be low (by Bernoulli's equation). Because there is a pressure difference on the top and the bottom, there is an upward pressure force applied to the airfoil (pressure on the top is lower). This creates lift. To move the aircraft forward, the

fixed wing aircraft has an engine to provide thrust forward. This thrust has to overcome the drag provided by air (mit.edu, 1997).

Rotorcraft UAVs

Rotorcrafts are defined as those aircrafts that can fly by the lift created by one or more rotating blades. Rotorcrafts are very popular in applications such as rescue mission, resupply mission etc., because of their unique ability to hover, take off and land vertically. Rotorcrafts are very useful because they can fly to and from any kind of terrain, making them very useful in emergencies, scientific studies and entertainment industry (eg. aerial filming).

Rotorcrafts ranges from very small (2/3 inches) to big full sized helicopters. Small rotorcrafts can be designed to be battery operated and whisper quiet increasing its usefulness in stealth operation. Small rotorcrafts are ideal in confined spaces for example, inside the buildings and caves (for scientific research or emergency operations) etc.

An example of a full sized rotorcraft is Boeing's Hummingbird (picture below). It is a completely autonomous UAV with flight time of up to 20 hours.



Figure 1-6 Full Sized helicopter UAV called Hummingbird (Trimble, 2009)

An example of a small rotorcraft is a miniature quad-copter (picture below). The miniature quad-copter is only 15grams and has all its components embedded in the printed board/frame. Many military bases around the world have been building some form of similar UAVs with more technology packed in a small size.



Figure 1-7 Miniature Quadcopter (Joblin, 2010)

Theory of Rotorcrafts:

Rotorcrafts use rotors to create lift. Rotors are the blades that are connected to a rotating shaft. The lifting force created by a rotor can be described by a simple theory called actuator disc theory (or momentum theory). Actuator Disc Theory states that lift is achieved by the change in momentum. The Actuator Disc Theory for hovering flight is derived below:

Assumptions: air is incompressible, and the flow is one-dimensional, existence of a stream-tube which is an asymmetric surface passing through the rotor disc perimeter which isolates the flow through the rotor.

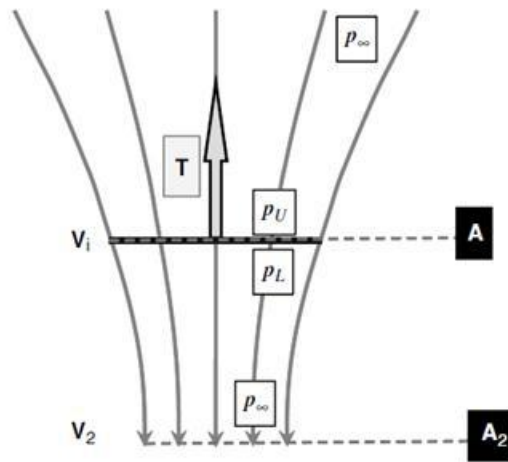


Figure 1-8 Actuator Disc Theory (Seddon and Newman, 2011)

The flow enters the stream tube, is accelerated through the rotor disc increasing the velocity and exits the stream-tube. The continuity equation of the flow can be represented by the following:

$$\rho AV = \text{Constant}$$

So, $\rho AV_i = \rho AV_2$ (3)

The rate of change of momentum gives the thrust of the rotors:

$$T = \rho AV_i \cdot V_2 \quad (4)$$

Thrust can also be represented in the form of pressure difference as follow:

$$T = A (p_L - p_U) \quad (5)$$

Now by Bernoulli's equation. Assuming that the velocity of the air in infinite distance upstream of the rotor is 0, above the rotor, the Bernoulli's equation takes the form of:

$$P_\infty = P_u + \frac{1}{2} \rho V_i^2 \quad (6)$$

Below the rotor the Bernoulli's equation looks like

$$P_L + \frac{1}{2} \rho V_i^2 = P_\infty + \frac{1}{2} \rho V_2^2 \quad (7)$$

Subtracting these gives:

$$P_L - P_U = \frac{1}{2} \rho V_2^2 \quad (8)$$

Since,

$$T = \rho AV_i \cdot V_2 = A (p_L - p_U) = A \frac{1}{2} \rho V_2^2$$

$$V_2 = 2V_i$$

So,

$$V_i = \sqrt{\frac{T}{2\rho A}} \quad (9)$$

The power of the rotors to produce given thrust can now be written as

$$P_i = \sqrt{\frac{T^3}{2\rho A}} \quad (10)$$

Flapping Wing UAVs

We human beings have been long intrigued by the way birds fly. In fact when Leonardo Da-Vinci (1452-1519) made one of the early aircrafts, it was modeled after a bird. Although that aircraft was not successfully built during that period, modern technology has allowed us to create an aircraft with flapping wings at present. A flapping Wing UAV is identified as an aircraft that uses flapping wings as the propulsion system. It may also use airfoil style wings to perform gliding motion along with the flapping to rise up.

One of the best examples of a flapping wing UAV is the Smart-bird designed by a German company called Festo (robot bird 2011).



Figure 1-9 Festo Smart-Bird (robot bird, 2011)

The Smart-bird can fly just like a real bird, and can be made to look like a real bird when looking from the bottom, thus can serve as a valuable tool for military intelligence gathering.

Another very good example of a flapping wing UAV is the robot birds being developed in Wright-Patterson Air Force Base. (Airforce 2012)



Figure 1-10 Robot Bird (Airforce, 2012)

The bird like robot flies by flapping its wings and is designed to use to gather intelligence. In the picture above the bird is sitting on the wire monitoring the door for suspicious activity.

Unconventional UAV:

A UAV that uses propulsion system other than the fixed wings, rotorcraft or flapping wings fall under this category. For example people have been using helium (lighter than air) as a means of flying. Another unconventional flight system is using inversion to fly.

German inventor Paul Schatz has invented a “six-sided articulated rings of prisms that attached to a cube, and when it is unleashed, it can start unfolding into new geometric shapes. As it turns inside out, it moves forward. This property of kinematics is called inversion.” The flying object uses helium to float in the air and inversion to move forward.



Figure 1-11 UAV that uses helium and Inversion technology to fly (Forman, 2012)

Ducted fan

A ducted fan or ducted propeller is comprised of two components- the first one is the fan or propeller. Propeller is a device that converts rotational motion produced by the engine (or electric motor) into thrust. The second component is the duct. Duct can be defined as a channel or tube that can be used to convey particularly fluid. Ducts, or shrouds is used along with the propellers in a UAV for mainly two purposes:

1. It provides protection to the propellers against collision with the wall or contact with external things including human beings. This protects the propellers, from breaking in case of a crash or hurting people.
2. Ducts can increase the thrust produced. Most studies suggest that ducts increase the static thrust produced. If not optimized, the ducts could also lead to excessive losses.

The figure below helps clarify what the duct is. In the picture, the helicopter has two propellers. The big propellers (also called rotors), doesn't have any duct. The small propeller on the rear end of the helicopter is encased by a duct.

The two figures below the helicopter show a regular duct and the duct with perforations – the interest of this study.

Helicopter with both free(un-ducted) and ducted propellers (Piasecki, 2009)



Un-perforated Duct

Perforated Duct

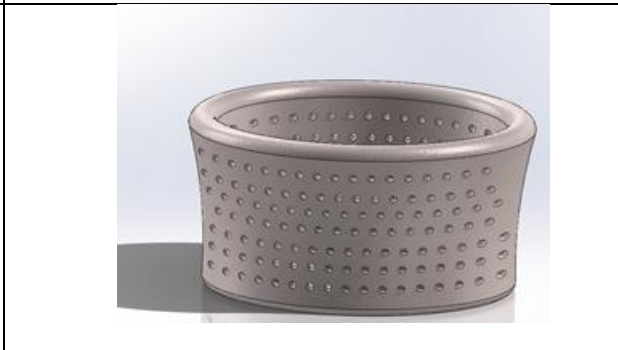
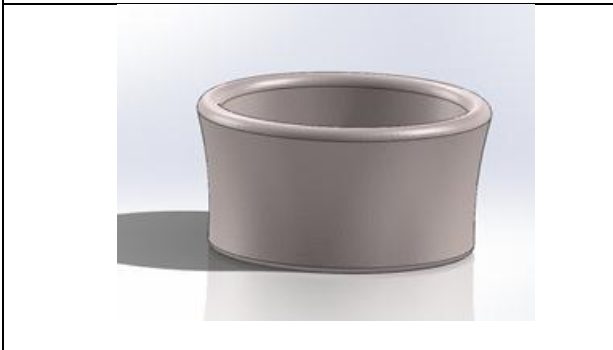


Figure 1-12 Examples of un-ducted and ducted propellers, and a perforated duct

Ducts are traditionally known to increase the net thrust produced by the propellers at high speeds. According to Raphael Yoli the ducts can create up to 30% more thrust over free propellers for some optimized conditions.

From a scientific study conducted by NASA on ducted rotors, it was found out that the Ducts increase the thrust in higher RPMs (>4000) of propellers. In relatively lower RPMs however, there were more losses due to the addition of duct (high internal duct drag). It was also found from the same study that as the tip gap was reduced, some gain in thrust was seen even in smaller RPMs (Martin,2004). Please note that the study doesn't relate RPM with

pressure difference created by the rotor fans. The figure below shows the results.

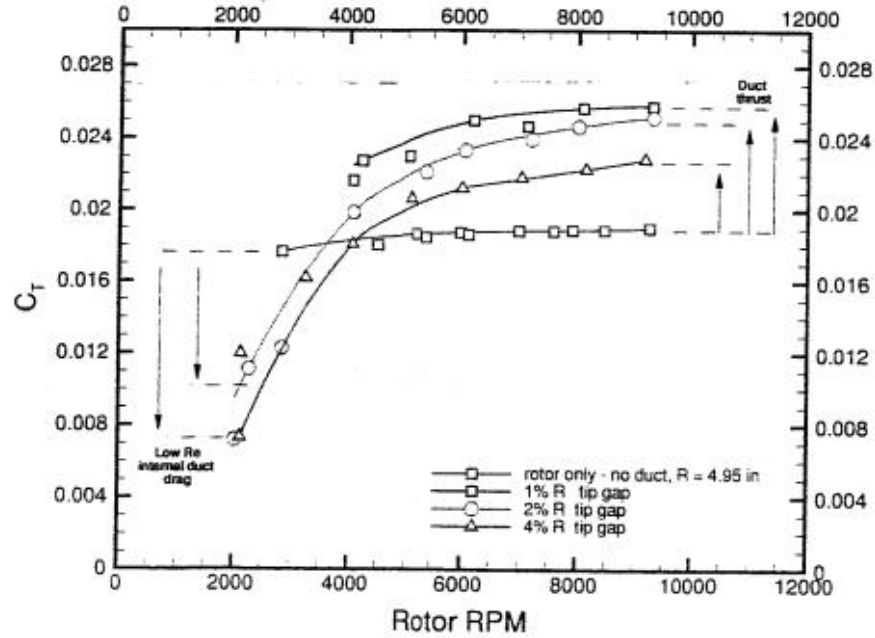


Figure 1-13: Thrust coefficient vs. Rotor RPM from an experiment done by NASA (Martin, 2004)

The ordinate axis represents the thrust coefficient defined as:

$$C_{t, \text{text}} = \frac{\text{Thrust}}{\rho AV^2} \quad (11)$$

Where,

$C_{t, \text{text}}$ is the thrust coefficient as defined by Dixon and Hall (2010), ρ is the density of the fluid. A is the area covered by the propeller, and V is the velocity of the tip of the propeller.

The abscissa shows RPM of the propeller blade.

In Figure 1-13, the ducts start showing increased thrust only after the propeller speed is faster than 4000 RPM. This transition speed changes depending upon the duct material, the size of the rotor, tip gap etc.

Motivation

Ducted propellers can be essential to some UAVs more than others. Take for example Incredible HLQ from Figure 1. In such rescue UAVs that needs to operate in confined or crowded areas, a duct may be necessary for public safety and the UAV's own safety. Additionally, ducted propellers are known to increase the efficiency up to 30% as compared to a free propeller (Martin, 2004). In a study performed in 2004 by NASA scientists, ducted propellers provided higher static thrust than free propellers in high RPM of the propeller. However the thrust was found to be lower in ducted propellers in low RPM Speed. As it is obvious, addition of duct increases the overall weight of the vehicle. Added weight can be a huge penalty for small UAVs which already have a small weight. Please note that the 30% increase in static thrust as calculated by NASA scientists didn't take into account the weight of the duct. It will be interesting to find out if there is any net thrust gain when the weight of duct is included for comparison. While ducted rotors can increase the thrust produced, it also adds weight to the UAV. It was therefore hypothesized that by removing part of the duct materials (i.e. adding perforations in the duct) would benefit from both decreased duct weight and increased thrust. However, it is not clear how much trade-off would be between these two factors. The motivation of this study is to find out if optimization in thrust is possible by using perforated ducts.

Objectives

The objectives of this study are:

1. Explore how the net thrust changes in small UAVs with ducted propeller when the weight of the duct is included in net thrust calculation at different RPM speeds.
2. Explore how addition of perforations in the duct affects the thrust at various RPM speed of the propellers by using commercial computational fluid dynamics software Ansys/Fluent.

Approach

The study was done mostly using Fluent and ICEM CFD software. The real conditions were simulated as closely as possible in the software and the case solved in the software. The first step was to learn the software. This phase of study was called CFD training and literature research period. Once the software was learnt, some simple cases such as pipe flow and channel flow were ran as they had easily available analytical solutions to compare the results from the Fluent to the analytical data. This was done to be proficient in modeling, and software usage. Next the cases without duct, with duct, and different size of perforations were done. Thrust was calculated using conservation of momentum equation. At the end useful conclusions were drawn from the results.

Chapter 2 : SOFTWARE TRAINING

The study presented in this study relies heavily on the Computational Fluid Dynamics (CFD) software called Fluent and the related meshing software called ICEM-CFD. Some very simple cases were studied and compared to their corresponding analytical solutions to verify the usefulness of software, and the accuracy of the results. Two of the many cases done are presented below to provide the examples of cases studied for training. Details of all the cases are available in the appendix.

Case 1: Laminar Channel Flow

Problem Statement:

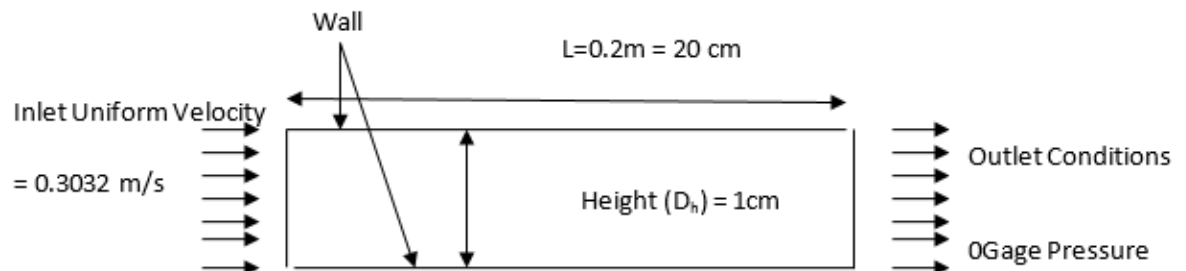


Figure 2-1 Problem Statement for Laminar channel flow

As shown in the figure above, air flows into the pipe at a uniform velocity of 0.3032 m/s and exits at atmospheric pressure.

Density used (ρ): 1.204 kg/m^3

Dynamic Viscosity (μ): $1.825 \cdot 10^{-5}\text{ kg/(m}\cdot\text{s)}$

Reynold's number based on the diameter = $Re_D = 200$

Solving Navier's Stokes Equations, it can be proved that,

$$\frac{u_{\text{avg}}}{u_{\text{max}}} = \frac{2}{3}$$

The problem was solved in Fluent. The fully developed velocity profiles are compared as follows:

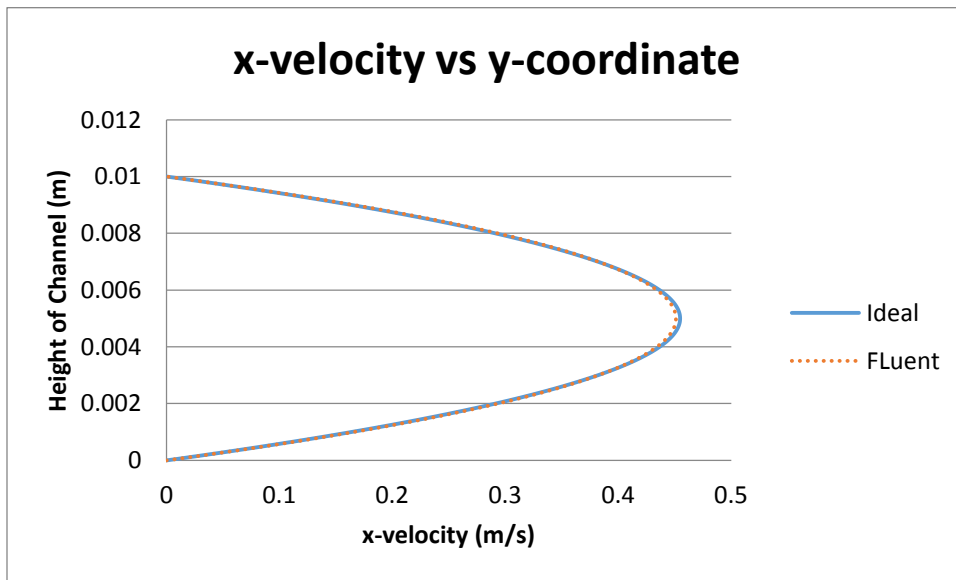


Figure 2-2 x-velocity vs. y-coordinate for laminar channel flow

The average velocity of the fully developed flow is 0.3032 m/s. From the graph above, the maximum velocity is expected to be around 0.45 m/s. The maximum velocity as obtained from the Fluent's solution is about 1.53% off of the ideal solution. The error mainly comes from lack of enough grid points.

The skin friction coefficient is plotted in the figure below showing that the skin friction coefficient remains constant once the flow is fully developed.

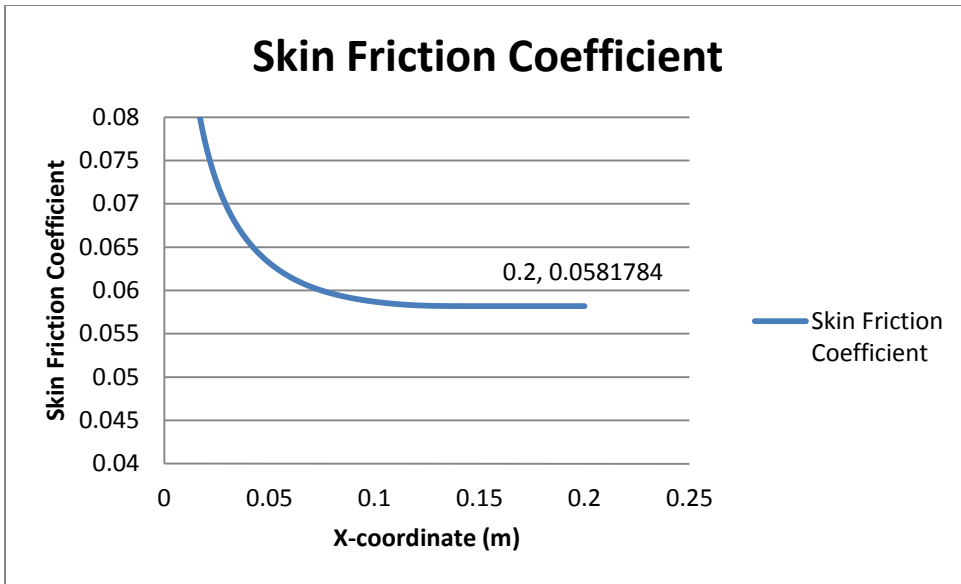


Figure 2-3 skin Friction coefficient for laminar channel flow

Case 2: Laminar Pipe Flow with a constant heat flux at the surface

Problem Statement:

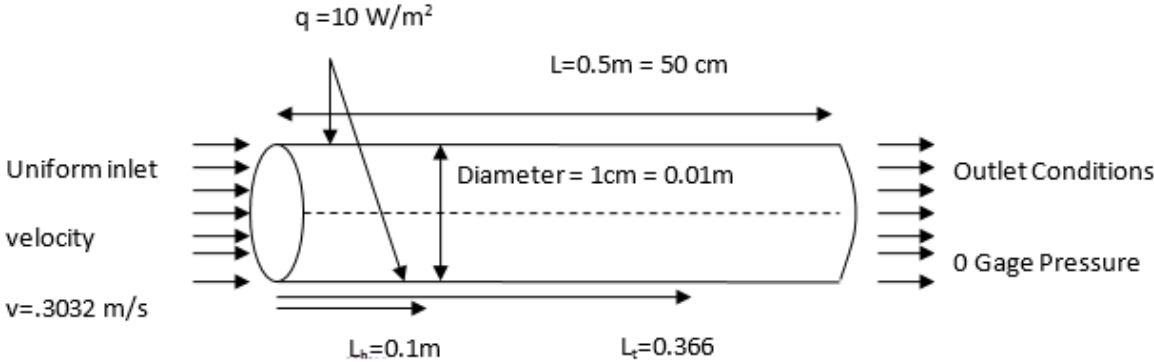


Figure 2-4 Problem Statement for Laminar Pipe flow with a constant heat flux

The flow comes in at a uniform inlet velocity of $v = 0.3032\text{ m/s}$ and exits the 50 cm long pipe at atmospheric pressure.

The fully developed velocity profile of analytical solution is compared to the solution from Fluent as follows:

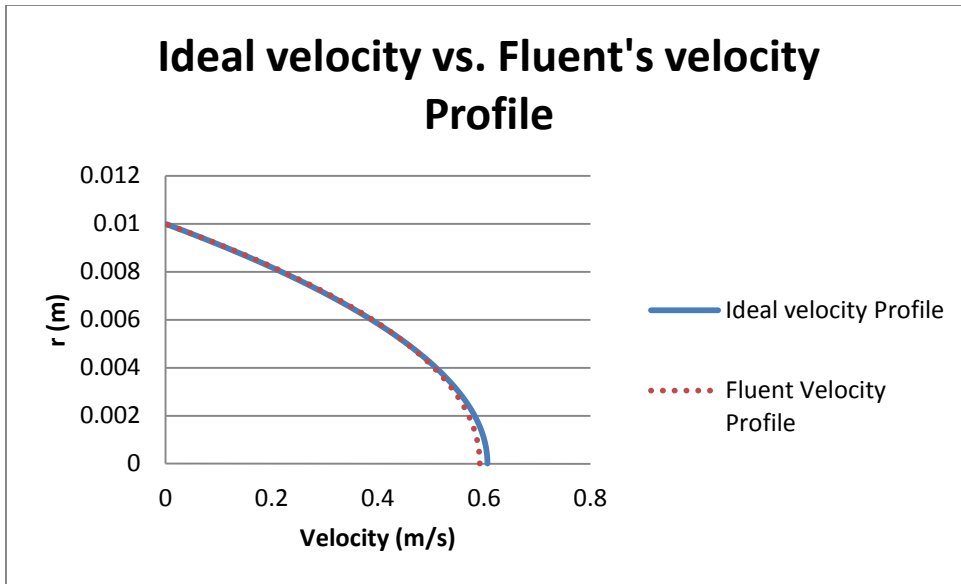


Figure 2-5 Ideal velocity vs. velocity profile obtained from fluent

As can be see, the solution from fluent was only 2.4% away from the analytical solution.

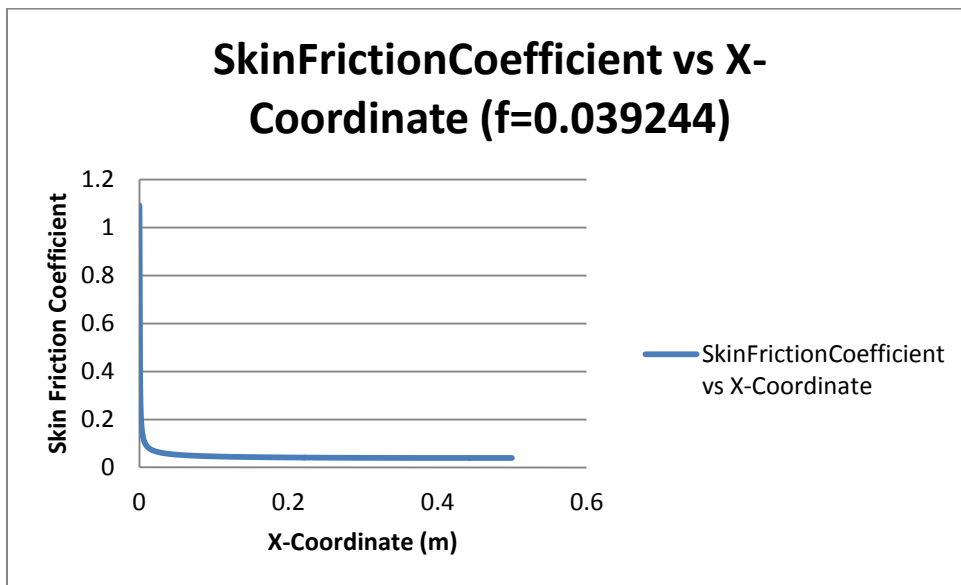


Figure 2-6 skin friction coefficient vs x-coordinate

The skin friction coefficient remains constant after a certain distance.

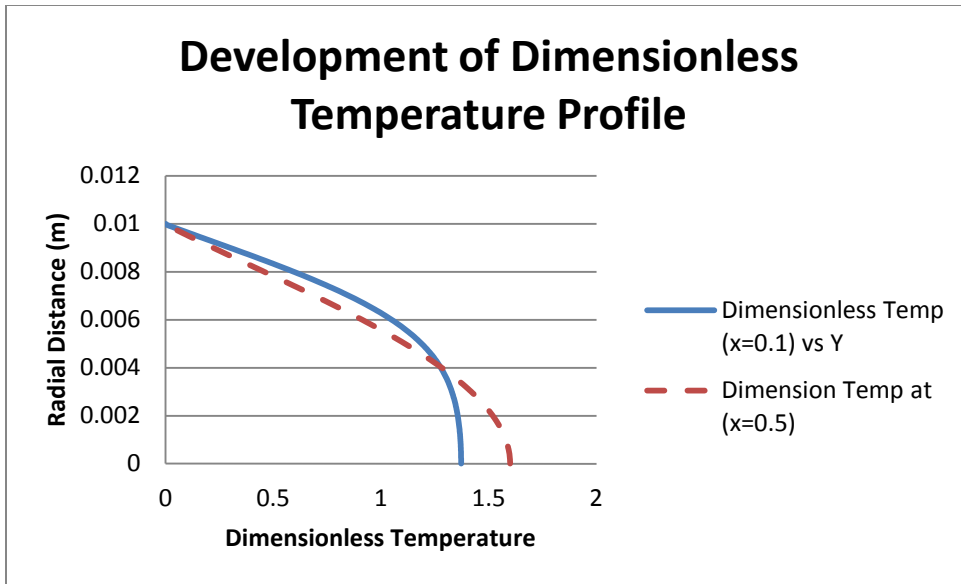


Figure 2-7 Development of Dimensionless Temperature profile

The dimensionless temperature profile develops to be fully developed as shown in the figure above.

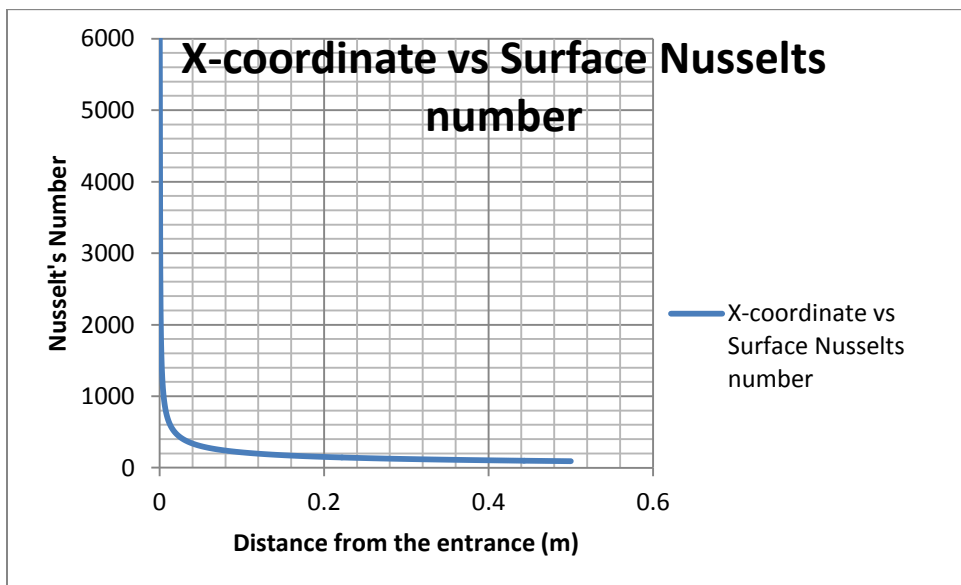


Figure 2-8 Variation of Nusselt's number with x-coordinate

The Nusselts number remains constant after a while.

Chapter 3 : THEORY

Thrust is defined as the upward force applied to the UAV, because of the momentum changed created by the propeller. To calculate Thrust, Momentum conservation equation was applied to all the surface surrounding the control volume. It is defined in much detail in the following sections.

Formulation of Momentum Equation:

The conservation of Momentum Equation (Newton's Second law) states that the force is equal to the rate of momentum change.

$$\sum F_{\text{ext}} = \frac{dP}{dt} |_{\text{sys}} \quad (3.1)$$

Where, P = Linear Momentum

Sys = system (Fixed Mass)

Before moving on, defining control volume and control mass (system) is deemed necessary.

System is any closed space, from which no mass particles is leaving or coming in. In other words, the mass of a system is constant. Eg. The air inside a soccer ball can be taken as a system, because there is no mass loss to the surrounding.

On the other hand, a control volume is any volume which is allowed to exchange both mass and energy to its surrounding. Eg. The volume around a turbine is a control volume.

For a fluid control volume, this equation for a system is related to the equation for a control volume by using Reynold's Transport Theorem, which states that:

$$\frac{dB}{dt}|_{\text{sys}} = \frac{\partial}{\partial t} \int_V \rho \beta dV + \int_A \rho \beta \vec{V} \cdot \vec{n} dA \quad (3.2)$$

Where,

B = conserved quantity

β = conserved quantity per unit mass

In our case, the conserved quantity is Momentum, set $B = P = m\vec{V}$, which makes $\beta = \vec{V}$

Hence the Reynolds's transport equation can now be written as:

$$\sum F_{\text{ext}} = \frac{dP}{dt}|_{\text{sys}} = \frac{\partial}{\partial t} \int_V \rho \vec{V} dV + \int_A \rho \vec{V} \vec{V} \cdot \vec{n} dA \quad (3.3)$$

Force = Rate of Change of Momentum = Rate of change of momentum within CV + Rate of Momentum Flux (Martin and Tung, Performance and Flowfield Measurements on a 10-inch Ducted Rotor VTOL UAV 2004)

Applying Momentum Equation to the Propeller without the duct:

An arbitrary control volume is created around the propellers and the Conservation of Momentum Equation is applied around it.

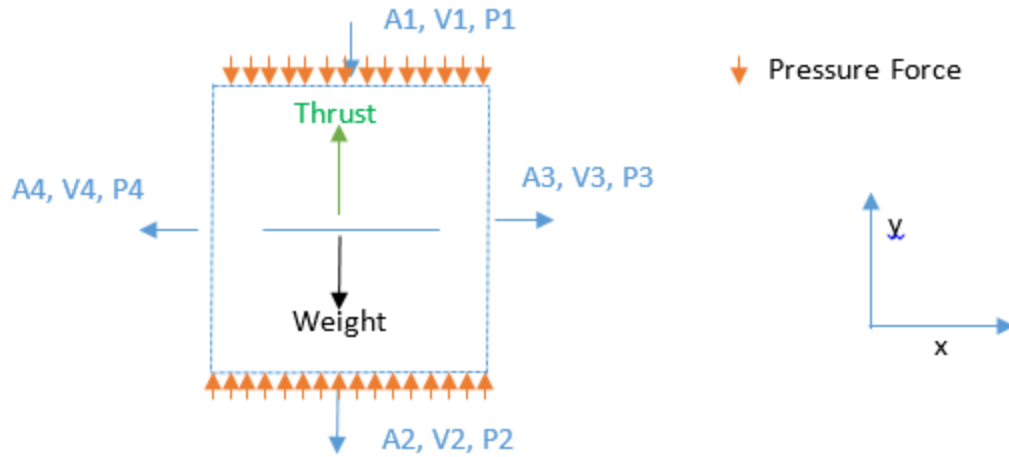


Figure 3-1: Conservation of momentum

For simplification, assume that the flow is coming in from the top, and going out from the other three sides. Let the velocities in each side be as shown in the figure above. Assume the Areas to also be as shown in the figure above. Although the velocity is not uniform throughout the Area, it was assumed that the given velocities are the average velocities, so that constant velocity assumption is valid.

Since, our interest lies in the Y-directional Forces, The equation for thrust were derived using momentum equation in Y-direction. In the equation:

$$\sum \mathbf{F}_{ext} = \frac{dP}{dt} |_{sys} = \frac{\partial}{\partial t} \int_V \rho \vec{V} dV + \int_A \rho \vec{V} \vec{V} \cdot \vec{n} dA \quad (3.4)$$

The right hand side is given by

$$\sum \mathbf{F}_{ext} = \mathbf{Thrust} - \mathbf{Weight} + \mathbf{P2A2} - \mathbf{P1A1} \quad (3.5)$$

In the left hand side, assuming steady state, the volumetric term goes to zero and the RHS gets reduced to

$$\frac{\partial}{\partial t} \int_V \rho \vec{V} dV + \int_A \rho \vec{V} \vec{V} \cdot \vec{n} dA$$

Rearranging the two terms:

$$\begin{aligned} \text{Thrust} = \text{Weight} - P_2 A_2 + P_1 A_1 + \text{Abs} \left(\int_A \rho \vec{V} \vec{V} \cdot \vec{n} dA \right)_{\text{top}} \\ - \text{Abs} \left(\int_A \rho \vec{V} \vec{V} \cdot \vec{n} dA \right)_{\text{bottom}} \end{aligned}$$

(3.6)

Simplifying the momentum flux terms by presuming a average velocity and average pressure:

For the Top,

$$\int_A \rho \vec{V} \vec{V} \cdot \vec{n} dA = \rho \cdot (-V_1)(-V_1)(1)(A_1) = \rho V_1^2 A_1$$

For the Bottom,

$$\int_A \rho \vec{V} \vec{V} \cdot \vec{n} dA = \rho \cdot (-V_2)(-V_2)(-1)(A_1) = -\rho V_2^2 A_2$$

For the Left and the Right, although, It was assumed that the flow is outwards, it needs to be noted that there is flow coming in-to the control volume in the area above the fan blade, and there is flow going out of the control volume in the area below the fan blade. Since the 2-D solution is symmetrical, the x-components should cancel out. There is going to be some y-velocity at the area of

the control volume. However, $\vec{V} \cdot \vec{n} = V \cos 90$ or $V \cos 270 = 0$ which makes our momentum flux terms to go to 0 at the control volume boundary 3 and 4.

For the sides,

$$\int_A \rho \vec{V} \vec{V} \cdot \vec{n} dA = \rho \cdot (-V_2)(-V_2)(0)(A_1) = 0$$

Thus, our Equation is reduced to

$$\sum F_{ext} = Thrust - Weight + P_2 A_2 - P_1 A_1 = \rho V_1^2 A_1 - \rho V_2^2 A_2 \quad (3.7 a)$$

Rearranging to get thrust,

$$Thrust = Weight - P_2 A_2 + P_1 A_1 + \rho V_1^2 A_1 - \rho V_2^2 A_2 \quad (3.7 b)$$

Thus, the Thrust is calculated for the given control volume. A square control volume is purposefully drawn around the propeller in cases with or without the duct to simplify the solution.

To find the actual Thrust in the results sections, the following formula is used:

$$Thrust = Weight - P_2 A_2 + P_1 A_1 + Abs\left(\int_A \rho \vec{V} \vec{V} \cdot \vec{n} dA\right)_{top} - Abs\left(\int_A \rho \vec{V} \vec{V} \cdot \vec{n} dA\right)_{bottom} \quad (3.8)$$

The momentum flux terms are in absolute values because the integrals are calculated with the direction of area towards the bottom in both cases. The absolute values help maintain our sign convention.

Modified Thrust Coefficient

Since rotor tip velocity is not available to us to define thrust coefficient as many text books do, the thrust Coefficient used in the results is redefined as:

$$C_t = \frac{\text{Thrust}}{\rho A V^2} \quad (3.9)$$

Where,

C_t is the thrust coefficient, ρ is the density of the fluid, A is the cross sectional area of the disc(that replaces propellers), and V is the maximum velocity of the air in the control volume.

Efficiency of Duct

The efficiency of the ducted fan is given by:

$$\text{Efficiency } (\eta) = \frac{\text{Thrust Output}}{\text{Pressure Force In}}$$

Thrust output is the net thrust (including the duct weight) obtained. Pressure Force in is the pressure that is put in as input in the fan blade. The Pressure Force In is calculated as

$$\text{Pressure force in} = \Delta P * A$$

ΔP is the Pressure difference that is input in the fan boundary conditions, and A is the surface area of the infinitely thin Disc that is creating the discontinuous pressure difference.

Navier-Stokes Equations

Conservation of momentum can also be written using Navier-stokes Equations. For an infinitesimally small moving fluid element, the forces applied in the x-direction can be represented as the figure below. The forces applied to the body are pressure forces, and the viscous (shear and normal shear) forces. Starting out with $F=ma$ in each of the three Cartesian directions, and with some modifications (similar to the one in thrust calculation section above) the Navier-Stokes Equations is obtained. The detailed derivation can be easily found in any Fluids or CFD text book (eg. Anderson's CFD). Fluent uses these three equations to solve for unknown quantities.

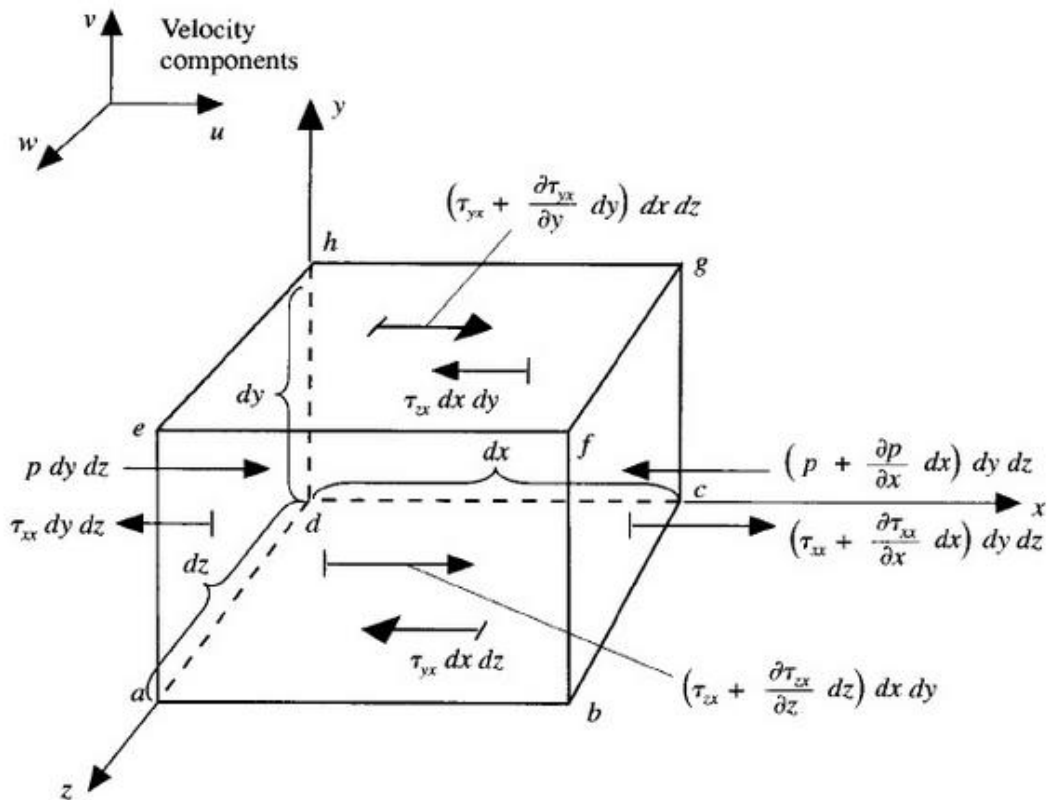


Figure 3-2 Forces in x-direction in an infinitesimally small, moving fluid element (Anderson CFD)

The Navier Stokes Equations (Munson, Young and Okiishi 2008) is given as:

$$\rho \left(\frac{\partial u}{\partial t} + u \frac{\partial u}{\partial x} + v \frac{\partial u}{\partial y} + w \frac{\partial u}{\partial z} \right) = - \frac{\partial p}{\partial x} + \rho g_x + \mu \left(\frac{\partial^2 u}{\partial x^2} + \frac{\partial^2 u}{\partial y^2} + \frac{\partial^2 u}{\partial z^2} \right) \quad (\text{x - direction})$$

$$\rho \left(\frac{\partial v}{\partial t} + u \frac{\partial v}{\partial x} + v \frac{\partial v}{\partial y} + w \frac{\partial v}{\partial z} \right) = - \frac{\partial p}{\partial y} + \rho g_y + \mu \left(\frac{\partial^2 v}{\partial x^2} + \frac{\partial^2 v}{\partial y^2} + \frac{\partial^2 v}{\partial z^2} \right) \quad (\text{y - direction})$$

$$\rho \left(\frac{\partial w}{\partial t} + u \frac{\partial w}{\partial x} + v \frac{\partial w}{\partial y} + w \frac{\partial w}{\partial z} \right) = - \frac{\partial p}{\partial z} + \rho g_z + \mu \left(\frac{\partial^2 w}{\partial x^2} + \frac{\partial^2 w}{\partial y^2} + \frac{\partial^2 w}{\partial z^2} \right) \quad (\text{z - direction})$$

(3.10)

3-D propeller to 2-D Disc

To study the effects created by a rotating propellers, a 3-D model of the propellers is ideal. However 3-D modeling is arduous and very time consuming. As an example, solving a 2-D duct with close to half a million grid points took close to 30 hours to converge. A 3-D study would have taken much longer. Secondly, the educational version of Ansys Fluent used for this study did not allow the number of grid points that would have been required for a 3-D propellers and duct. The main advantage of a 3-D model is much better swirl modeling. However, swirl was neither under the scope of this study nor did it greatly affect the thrust. Hence, the study was done in 2-D.

One major challenge was to reduce a 3-Dimensional propeller to 2-D. This was accomplished by using infinitely thin Disc (rotor disc). The thin disk creates discontinuous pressure change through it.

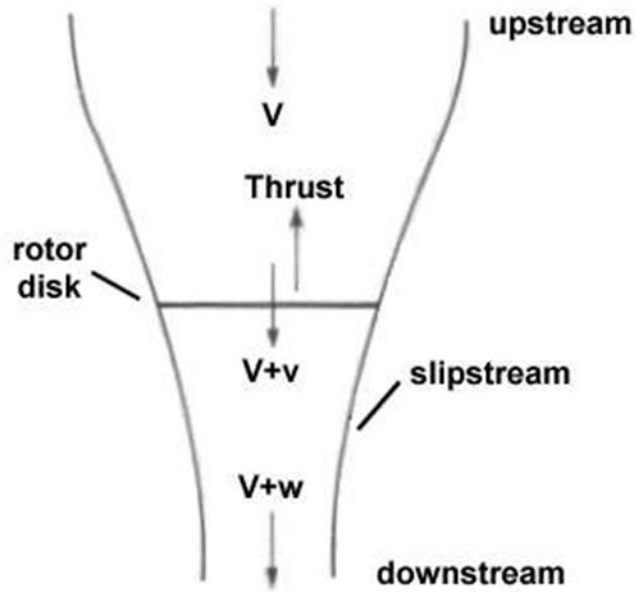


Figure 4-1 Actuator Disc Theory (Scott, 2011)

The disk can produce a constant momentum change along the axis perpendicular to the disk. Luckily, Fluent allowed modeling a fan using such a thin disk.

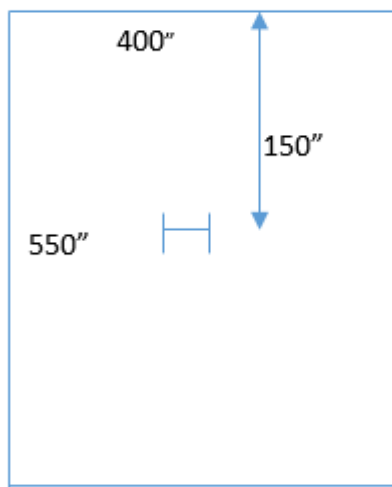
Infinite Domain to Finite Domain

The best way to model the propeller rotating is to model it with infinitely large domain around it, as it is in real life. However, only a finite volume around the propellers is affected by it, hence the propellers rotating can be modeled in a finite domain.

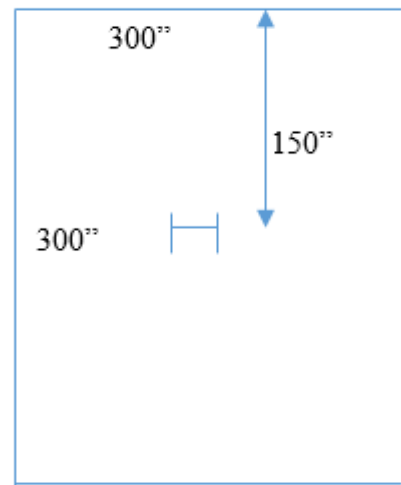
The next question that arises with using a finite domain is the size of the domain necessary to completely capture the air flow. To answer that question, a study was performed where, the domain size was varied in the increasing order and different values at the inlet and

exit of the duct were monitored. The monitored values are y-momentum flux, and Area weighted average pressure.

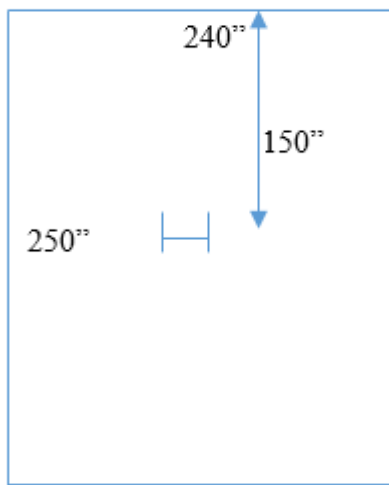
All of the domain sizes were rectangular. The four sizes are shown below. Different colors represent different sizes. Duct is always at the center in the x-axis so has not been shown in the figures. The Duct size has been exaggerated.



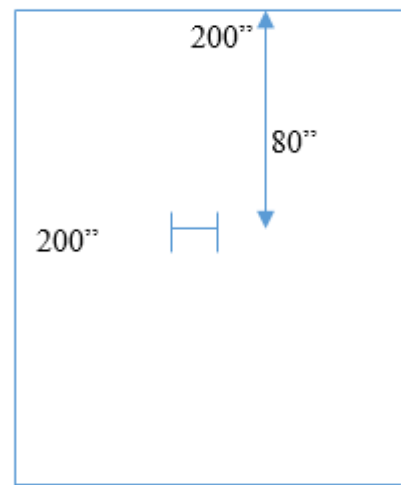
Biggest



Bigger



Big



Default

A control volume was drawn around the duct. The monitored values were monitored at duct inlet and duct outlet. They are tabulated in the following table:

Table 1 Selection of finite Domain size

Case	Top		Bottom		Thrust	% difference
	Pressure	Mom. Flux	Pressure	Mom. Flux		
Default	-674.9	36.92	-.1781	-37.72	33.15159	Datum
Big	-658.2	36.69	-1.987	-37.88	30.10817	9%
Bigger	-657.6	36.71	-1.789	-37.86	30.31583	9%
Biggest	-657.3	36.64	-1.556	-37.76	30.56366	8%

From the table, the value of thrust changed very little from around 30 N once the domain size was made one step bigger to 'big'. Since the change in Thrust for size bigger than the case 'big' did not make a significant change in thrust, domain size 'big' was selected.

Sensitivity of the size of control volume:

The first question that needed to be answered was how big to make the control volume. As explained in the theory section a cylinder extending from the top of the duct to the bottom

of the duct was chosen as the control volume. The next question that needed to be answered was what to take as the diameter of the cylinder. A study was conducted a study to see how changing diameter of the cylinder would change the thrust calculated. Our smallest diameter was the diameter of the duct which is 0.127 m, and the largest diameter was 0.3 m. The cylinder and the duct had coincident central axis. The results of the study is shown below. The datum was the Thrust calculated by using the diameter of the Duct.

	Diamter	Thrust	Remarks	% change
Duct with no pores	0.254	275.687	Datum	0%
	0.3	276.5809		0%
	0.4	278.7078		1%
	0.6	272.2305		1%
No Duct	0.254	274.3788	Datum	0%
	0.3	290.7763		6%
	0.4	297.6186		8%
	0.5	293.4466		7%
	0.6	292.8267		7%

Table 2 Sensitivity of the diameter of the control volume cylinder

From the table above, the sensitivity is very low for the duct; however it is pretty significant in the case with no duct. The thrust increases significantly when the diameter is increased from 0.127 m to 0.15 meters.

To calculate the thrust, the diameter of the cylinder was usually taken around 1.18-0.2 m, so that the maximum thrust provided by the rotors is captured. In calculating thrust for each

section, various diameters from 0.16-0.22 were tried, and the highest thrust producing diameter was selected.

This creates a source of inconsistency when comparing two thrusts, but this inconsistency was removed by using modified thrust coefficient.

Wall Functions

The wall functions in fluent are used to model the turbulent flow very close to the wall. Using wall functions allows fluent users to not have to create very fine mesh next to the wall. Wall function are usually determined by y-plus value. Y-plus value is the value calculated using the flow conditions that dictate how close the first mesh has to be to the wall. For accurate results when using standard wall functions, the y-plus value has to be around 30 – 200, closer you are to 30 the better. For all our meshes, y-plus value around the duct varied anywhere from mid 40s to ~160. Y+ values were calculated using the inbuilt y-plus calculator in Fluent.

Pressure inlet/outlet Boundary Conditions:

Fluent didn't have detailed definition of what different boundary conditions meant. To make sure, correct boundary condition was selected a study was done to verify the different boundary conditions. One boundary condition that wasn't well defined in the manual was pressure inlet/outlet boundary condition. To solve this conundrum, the case without duct was solved using three different boundary condition cases as shown in the figure below. The

pressure difference created by the disc blade was set to 3000 Pa. All the boundary conditions were 0 gage pressure. The results showed us that for our cases there is no difference in the results obtained by using either pressure inlet or outlet conditions. They meant the same thing. The three cases are shown in figures below. The comparison of results follows the figures:

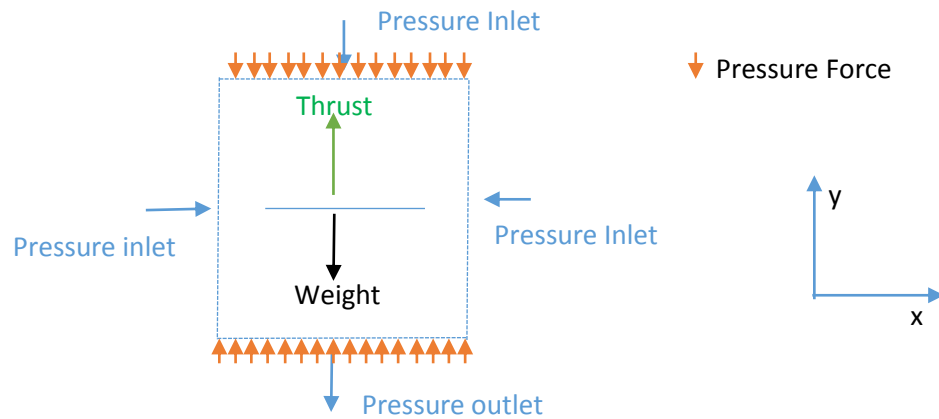


Figure 4-2 Case 1 - Pressure boundary conditions

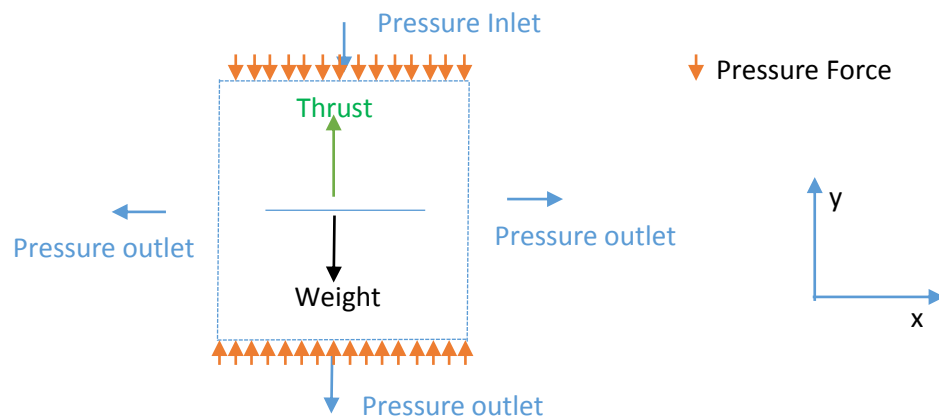


Figure 4-3 Case 2 - Pressure boundary conditions

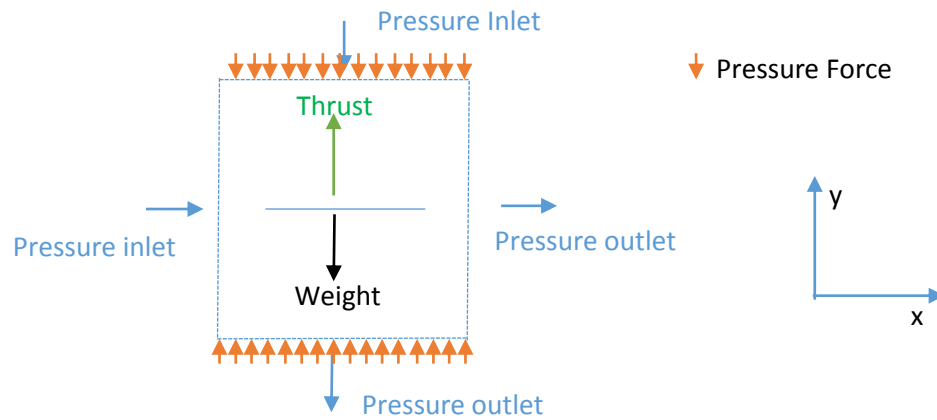


Figure 4-4 Case 3 - Pressure boundary conditions

From the table 3, there is not much difference in the results. The small differences can be ignored because that difference comes from the slightly different number of iterations while solving them using numerical method.

	Thrust Produced (N)
Case 1 (in-in)	147.518
Case 2 (out-out)	147.525
Case 3 (in-out)	147.513

Table 3 Pressure inlet and outlet boundary conditions

Choosing Pressure Difference

Calculation of Tip Velocity:

$$V_t = r\omega = \frac{r2\pi}{60} * RPM = (0.127m) * 0.10472 * 5000 RPM = 66.49 m/s$$

Velocity of Sound in air:

$$a = \sqrt{\gamma RT} = \sqrt{1.4 * 287 \frac{J}{kgK} * 293K} = 343.11 m/s$$

Mach Number is defined as the ratio of the flow velocity to the speed of sound of air.

$$M = c/a$$

Whenever the Mach Number in a flow exceed about 0.3, the flow becomes compressible, and the fluid density can no longer be taken as constant. Hence Maximum flow speed achieved without making the fluid compressible is $c = 0.3 * 343.11 m/s = 102.9 m/s$.

The pressure difference is calculated using the formula:

$$P = \frac{1}{2} \rho V^2$$

Where, V is the velocity. This formula relates the pressure to velocity in a streamline (Bernoulli's equation). Ideally, the pressure difference should translate into the increase in the velocity given by the above formula. However because of various losses, it is not the case. 60 Pa, 3000 Pa, and 6000 Pa were chosen as the working pressure for the study.

Choosing Overall Dimensions

Size: For size, I used a 700mm quad-rotor that I have been building as a reference. It has 10 inch rotors with a Turnigy motor that can go up-to 1000 rpm per volt with rotors. This brings us to about

5000 rpm in a 5Volt Power source. The max rated power is 730 (HobbyKing 2013). Hence 10-inch rotors were used to get a realistic feel.

Perforations

Many different perforations were chosen to be compared. The perforations were increased to increase the open area %, which went from 0% open area for duct with no pores to 100% area for propellers without duct. Each perforation is explained by using figures below.

1. 0% Open Area: This configuration has no open area, i.e. complete duct. The duct has no perforations included.
2. 8% Open Area: This configurations has 4 0.1" pores on the duct, two are above the propeller disc and two are below the disc as shown in the figures below. From the solid model(Figure 4-5), the pores created in 2-D translate to a duct with continuous open area. Although this is unrealistic and the real model would rather have scattered pores, our only concern is the trends in thrust, and this model provides accurate enough

information on the trends.

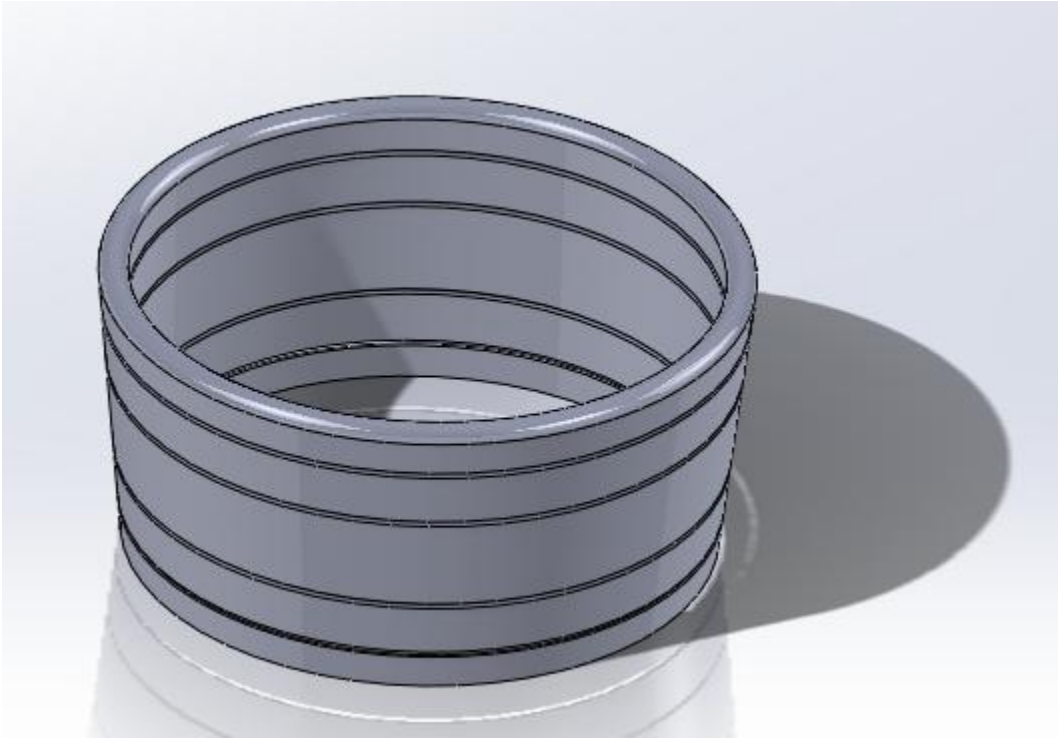


Figure 4-5: 3-D Translation of an axis-symmetrical plane with 4 Pores

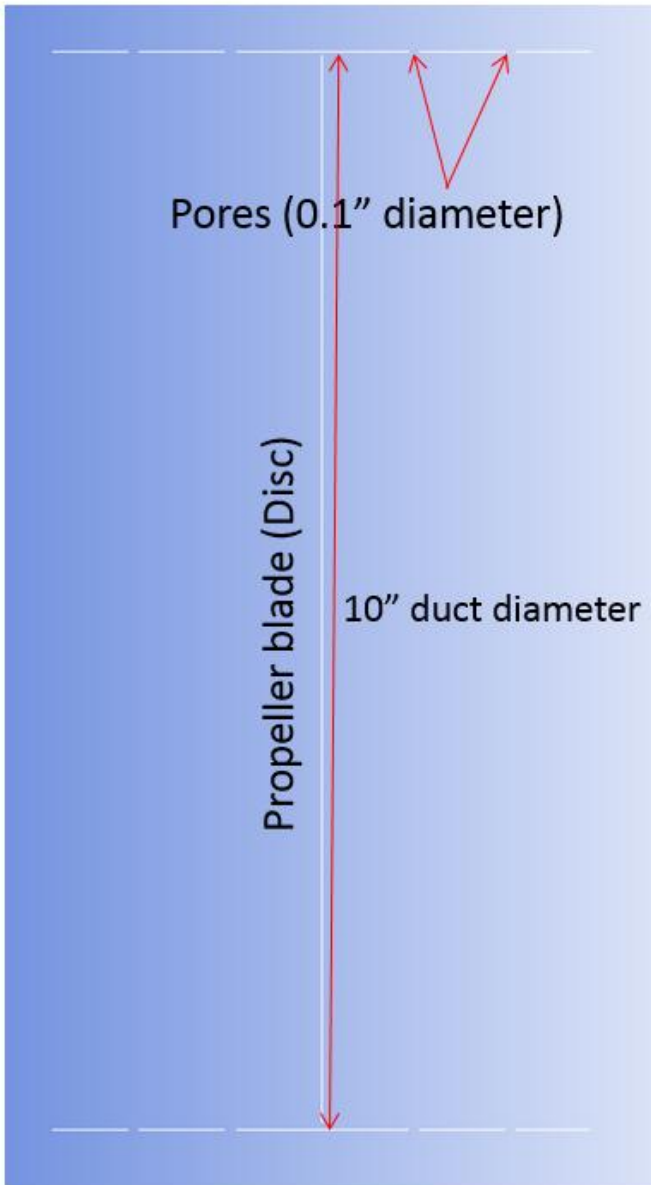


Figure 4-6: 2-D Duct with four Pores

3. 12% Open Area: This configuration is very similar to the 8% open area. The increase in % open area is obtained by increasing the number of pores from 4 to 6.
4. 16% Open Area: This configuration is also similar to the 8% and 12% open area configuration. The number of pores here is increased to 8.

5. 24% Open Area: To create a more realistic situation with the perforations, the pore diameter was increased to 0.3". This configuration has 4 pores on each side.
6. 36% Open Area: This also belongs to the family of 24%, but has 6 Pores.
7. 48% Open Area: This configuration has 6 pores on each side, the pores are 0.3" in diameter.
8. 40% Open Area: This configuration was created with 0.5" diameter pores. It has 4 pores.
9. 60% Open Area: 0.5" diameter pores, 6 pores
10. 80% Open Area: 8 0.5" diameter pores.
11. Tiniest Duct: This configurations has a very small duct surrounding it. The size of the duct is 1".

Verification of Symmetry: 2-D Modeling

The study of the ducts was done in 2-dimensional using axisymmetrical model. However, to verify the symmetry of the flow, a 2-D model of the duct, (as seen in figure above) that extended 1m behind the screen/paper was devised. The contour plots of the velocity and pressure is given below. It can be seen that both the velocity and the pressure are symmetrical in 2-D. This gave us a confirmation that the duct flow can be simulated using an axisymmetrical model. From the figures below, it is clear that both the pressure and the velocity are symmetrical.

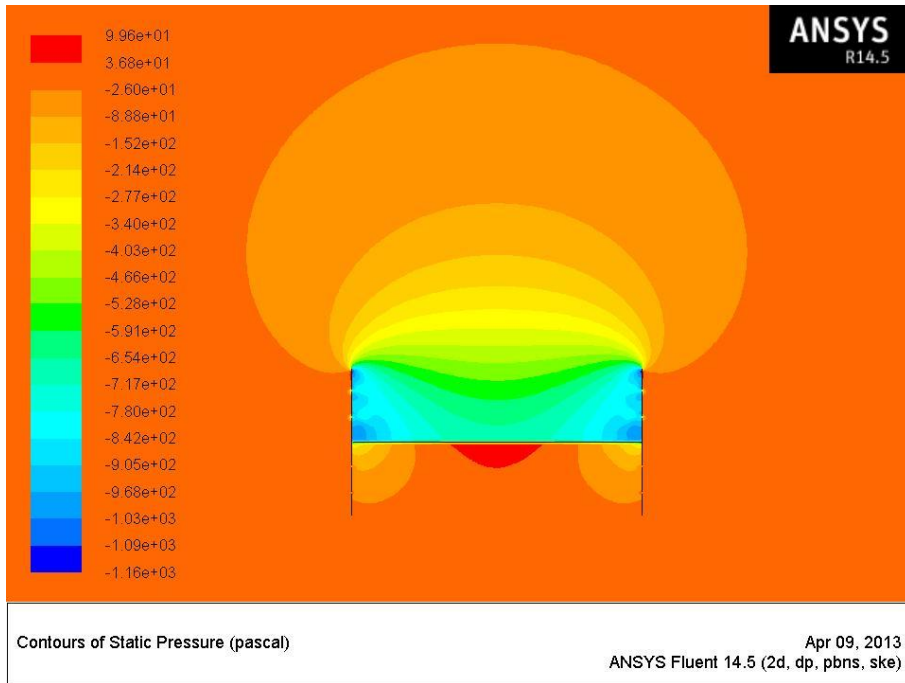


Figure 4-7: Contours of Static Pressure in a 2-D model

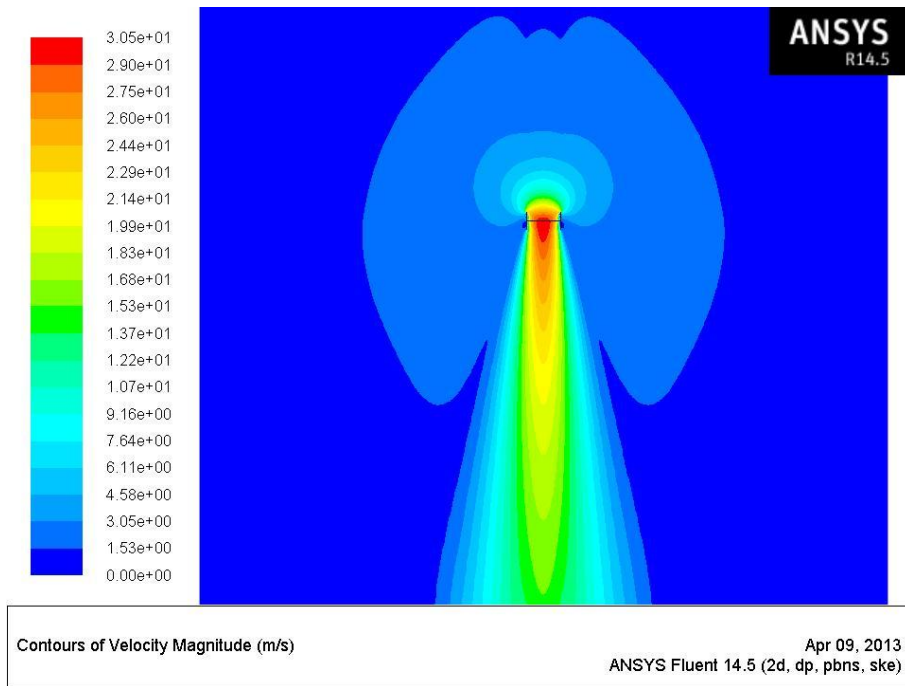


Figure 4-8: Contours of velocity magnitude in a 2-D model

Axisymmetrical Modeling

After verifying that the flow is symmetrical, it is concluded that the flow can be modeled as a axisymmetrical flow. Fluent allows the axisymmetrical modeling where you only need to model a section of the entire flow region (patterned area below). Fluent will extrapolate the results to the entire 3-D.

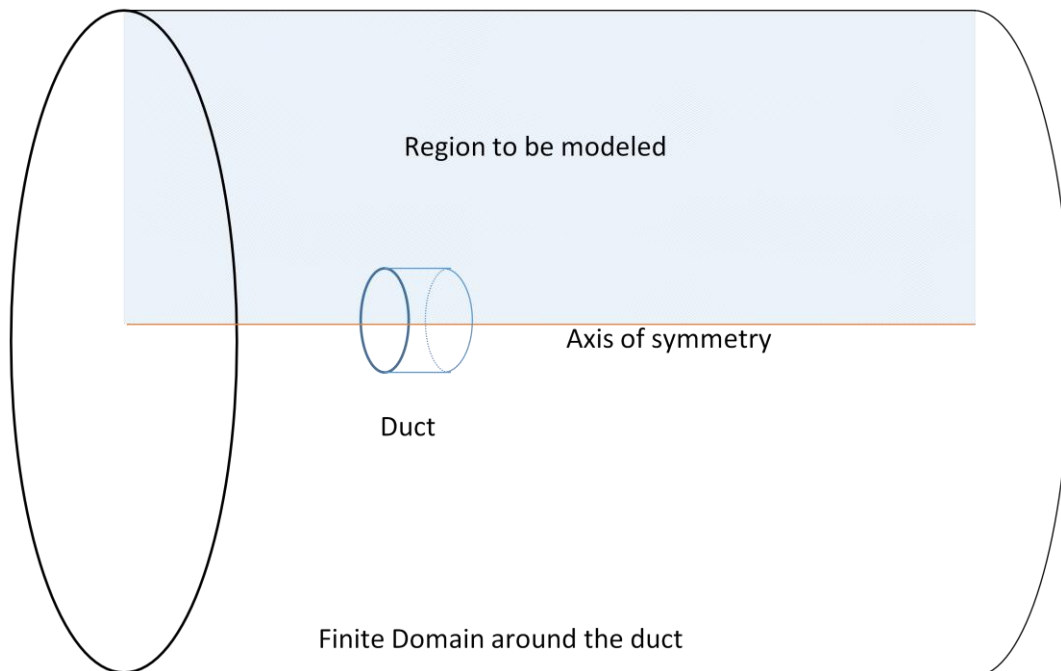


Figure 4-9: Axisymmetrical modeling

Grid Independent Study

Grid independent study aims at understanding the dependency of the mesh density with the accuracy of the solution. Each point (grid) represents the point where fluid flow is calculated. Ideally, it is preferred to have infinite number of grids. However, computation power and time is limited in any case. Grid independent study tries to find out the minimum

number of grid points necessary without sacrificing much accuracy. Our main limitation on Grid is 500000, because student version of Fluent was used to solve the flow. However, 500,000 is a lot of grids, and our flow is fairly simple. Additionally, since an axis symmetric model is used, our computational domain is reduced to half. Thus the maximum grid number chosen was 370k.

In reducing the grid points from the maximum grid points, everything was reduced in proportion. For example, the ratio of number of nodes in each section was kept almost same.

The result of the grid independent study was that the mesh density that was the ideal was more than enough. However, the maximum number of grids was selected because computer resources were available.

Number of Grid Points	Bottom		Top		Upward Pressure Force	Momentum Flux	Thrust
	Pressure Force	Mom. Flux	Pressure Force	Mom. Flux			
370 k	0.528	-297.962	-142.599	-157.909	-143.128	-140.052	-283.180
150 k	0.699	-301.557	-141.693	-161.213	-142.391	-140.345	-282.736
80 k	0.657	-302.131	-139.480	-159.475	-140.138	-142.657	-282.795

Table 4 Grid Independent Study for case 5

Chapter 5 : RESULTS, DISCUSSIONS AND CONCLUSIONS

The cases are tabulated below for easier access. Highlighted cases have been presented in the following section.

Case	Pores	Open Area
1	No Pores	0%
2	.1" 4 Pores	8%
3	.1" 6 Pores	12%
4	.1" 8 Pores	16%
5	.3" 4Pores	24%
6	.3" 6 Pores	36%
7	.5" 4 pores	40%
8	.3" 8 Pores	48%
9	.5" 6Pores	60%
10	.5 " 8 Pores	80%
11	Tiniest Duct	96%
12	No Duct	100%

Case 1: 2-D Duct with no Perforation

This case was the basic case, with which everything else was compared.

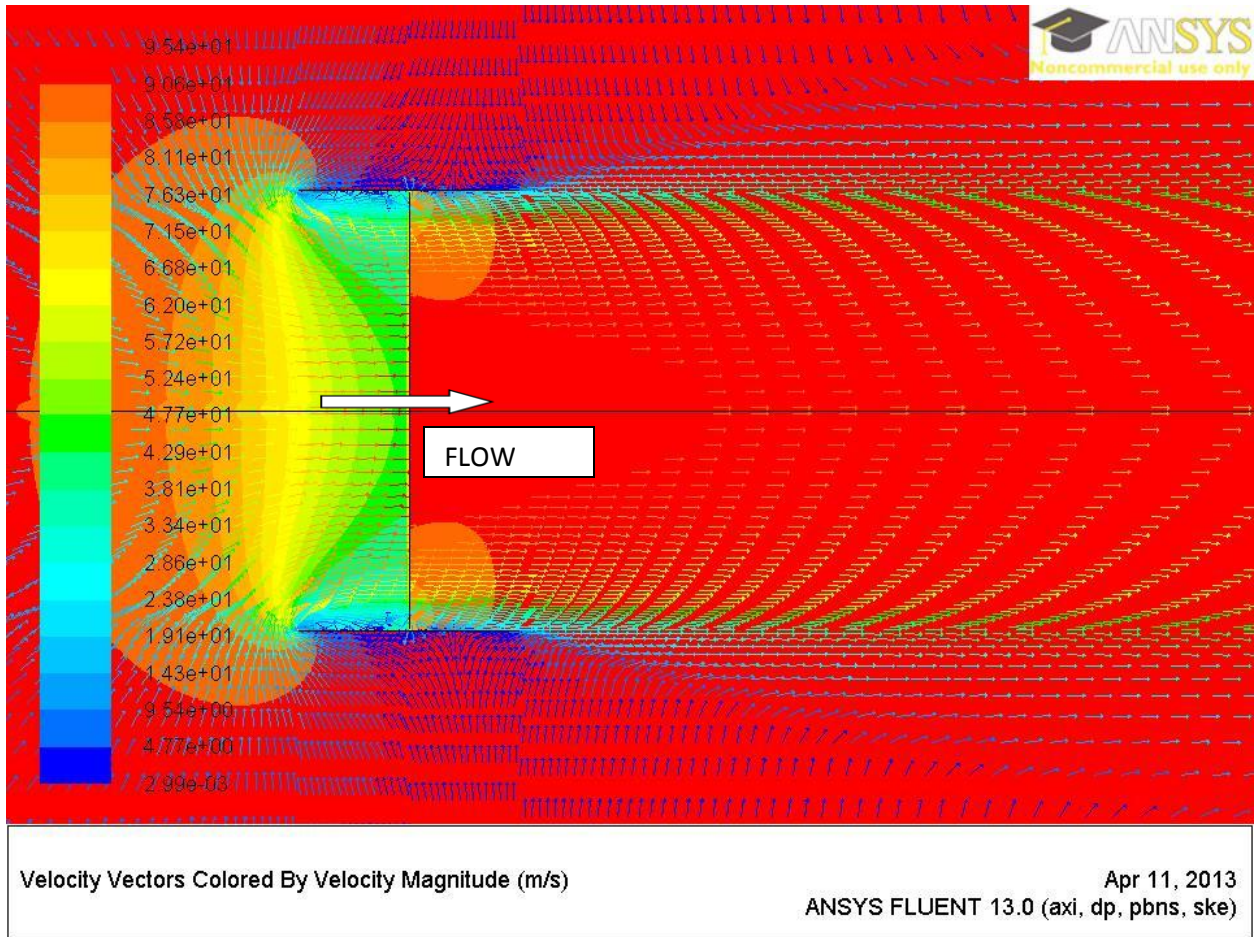


Figure 5-1 Case 1: Duct with no perforations - velocity vectors overlaid on pressure contour

If the figure above, the velocity vectors are overlaid on the Pressure Contour. The air comes in from the Top (left side), and passes through the duct. Looking closely at the area around the blades, it can be found that there is some tip loss, i.e. some air travels backwards through the tip gap. This creates a recirculation zone next to the tip gap.

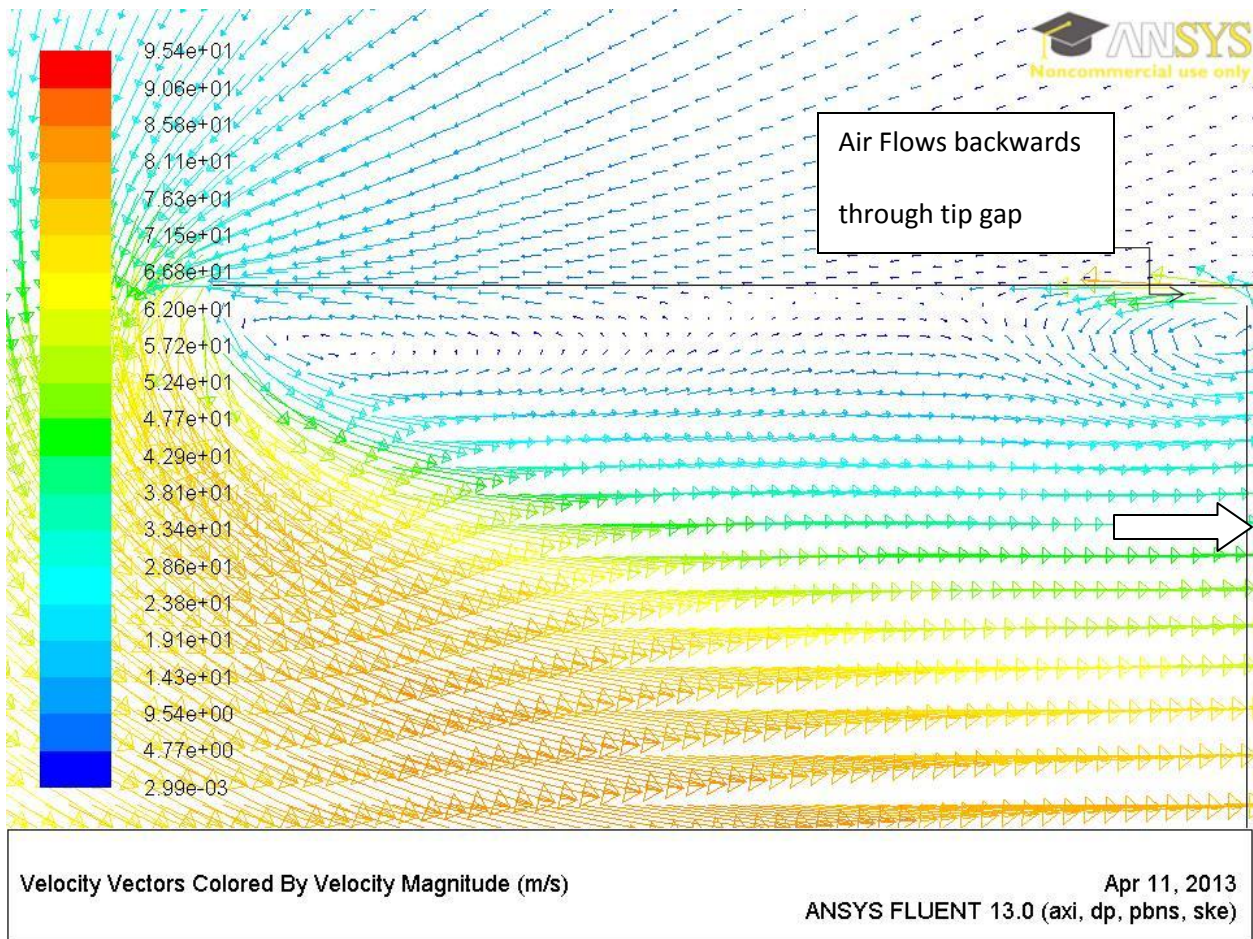


Figure 5-2 Recirculation near tip gap

In the figure above, it can be clearly seen that there is recirculation in two places. First is right above the fan. The second region is upstream from the fan. There is another flow separation (recirculation) going on below the duct inlet. This is caused by the shape of the duct inlet.

2-D Duct with 4 Perforations

In this case, duct had 4 perforations on each side, 2 on top of the blade and 2- on bottom of the blade. The picture below shows us that, there isn't too much going on most of the domain. The pressure gradient is higher closer to the duct. This was observed in all cases.

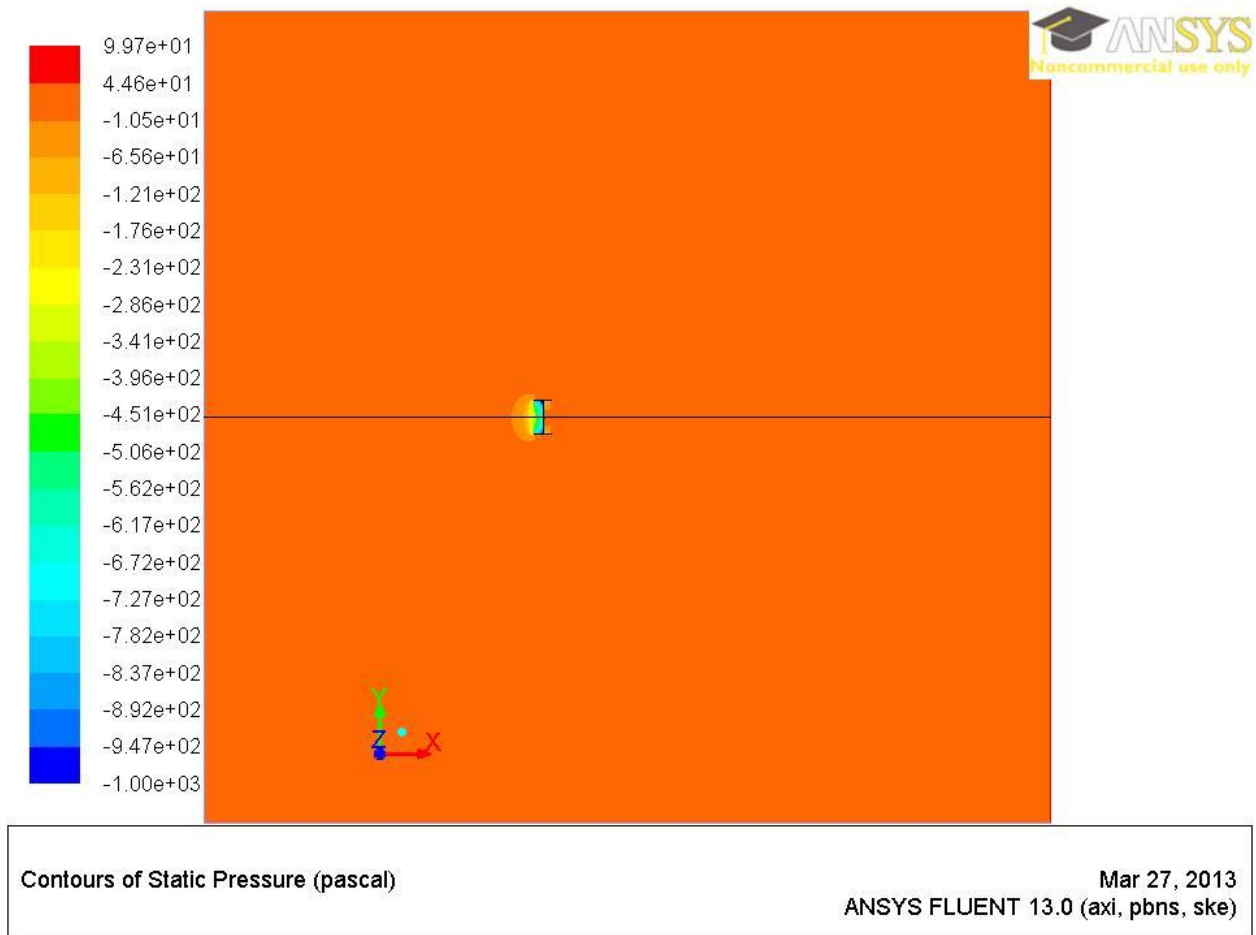


Figure 5-3 Contours of Static pressure - case 2

Significant velocity vectors, however can be noticed even far away from the duct as shown

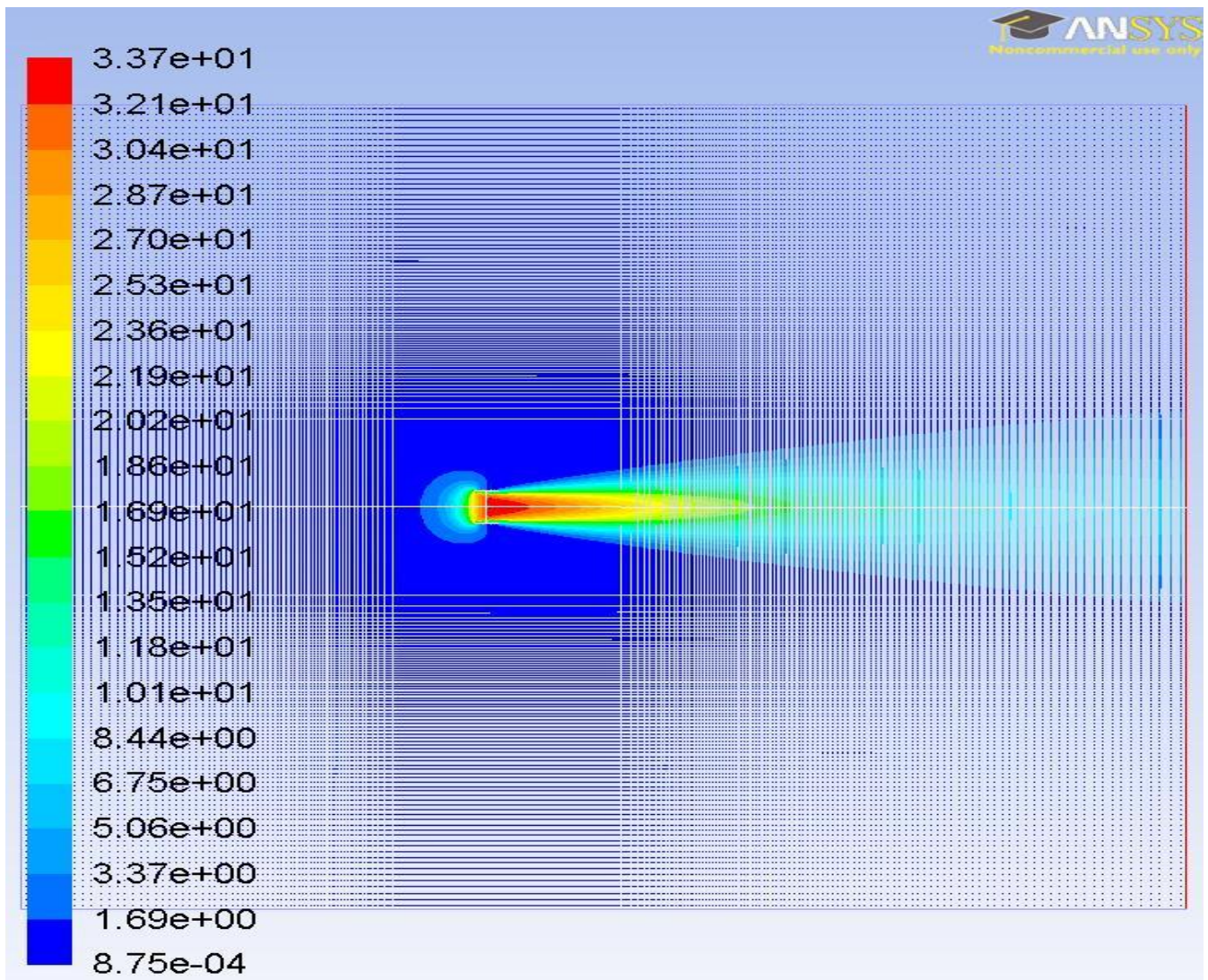


Figure 5-4 velocity vectors - case 1

in figure. The velocity magnitude is represented by the color. The maximum velocity it reached was 33.7 m/s.

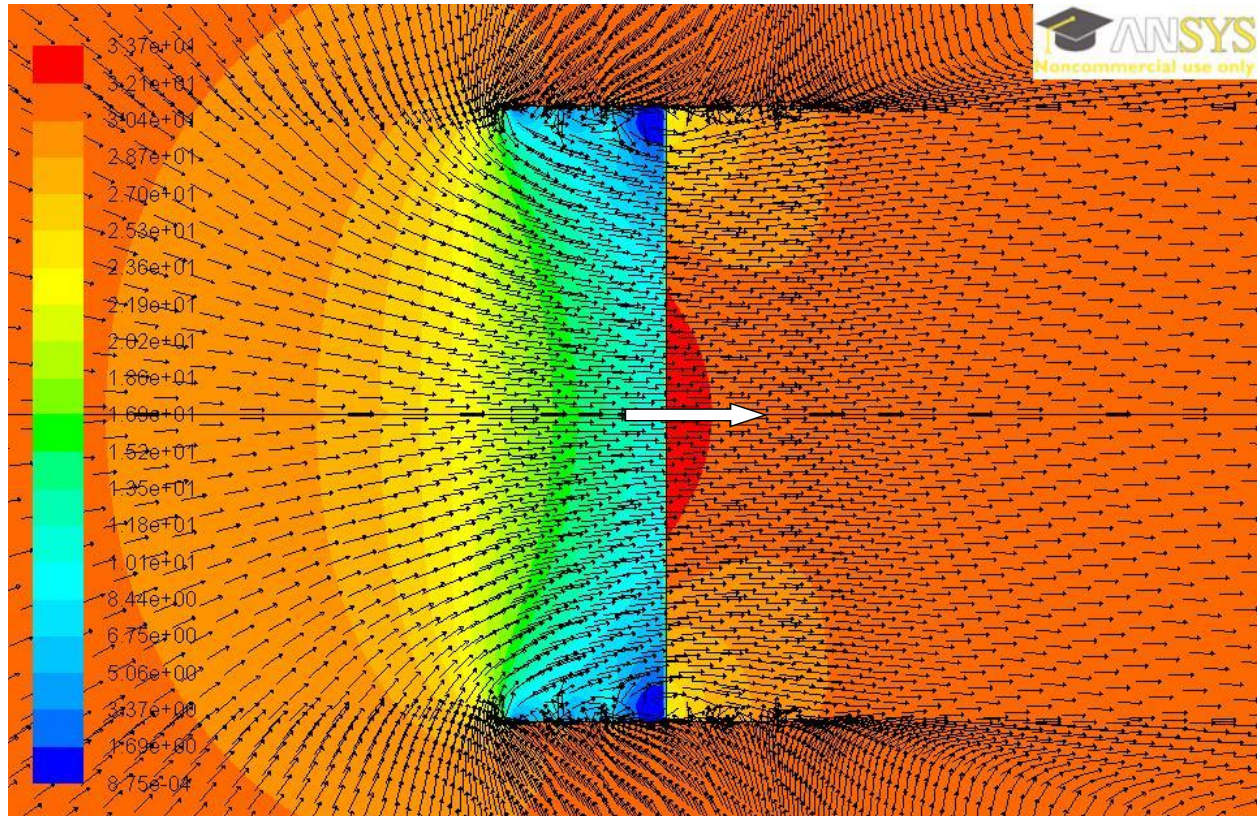


Figure 5-5 velocity vectors superimposed on pressure contour - case 1

The figure on the right shows the Pressure gradient with velocity vectors. The air comes into the duct and goes out from the bottom of the duct as expected. There is a big pressure gradient right at the duct. This is obviously the effect of the fan.

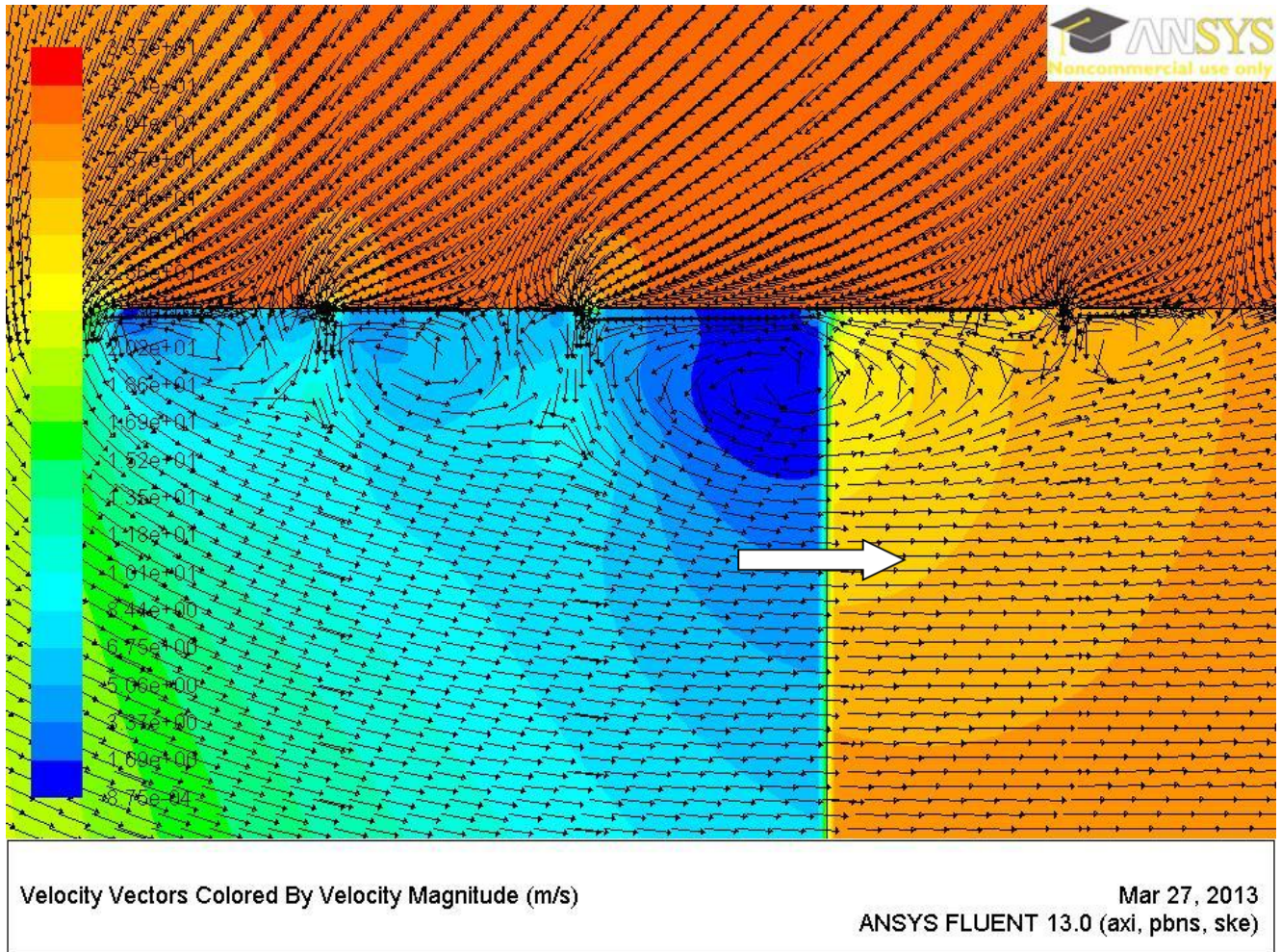


Figure 5-6 Closer look at the velocity vectors superimposed on pressure contour - case 2

A closer look at one side of the duct tells us that the air is moving in from every single pore, both at the top and the bottom of the duct. This is because the pressure outside is higher than the pressure right next to the walls inside the duct. Another effect of this is that the mass flow rate on the top of the duct is less than the mass flow rate at the bottom of the duct. In this case the mass flow rate at the top is 1.29 kg/s and the mass flow rate at the bottom is 1.42 kg/s. Additionally, there is some air going up above through the tip gap (gap between the propeller disc and the wall). This phenomenon is called tip loss. Tip loss can be avoided by manufacturing ducts and propeller with as small tip gap as possible. This includes number of

considerations such as expansion of the duct and the propeller due to temperature rise, accuracy in manufacturing processes etc. In some highly sophisticated turbo machinery, the tip gap is as small as fractions of an inch.

2-D Duct with 6 Pores:

Just Like the case discussed above, the pressure gradients were abundant near the duct, and not too much in the rest of the domain.

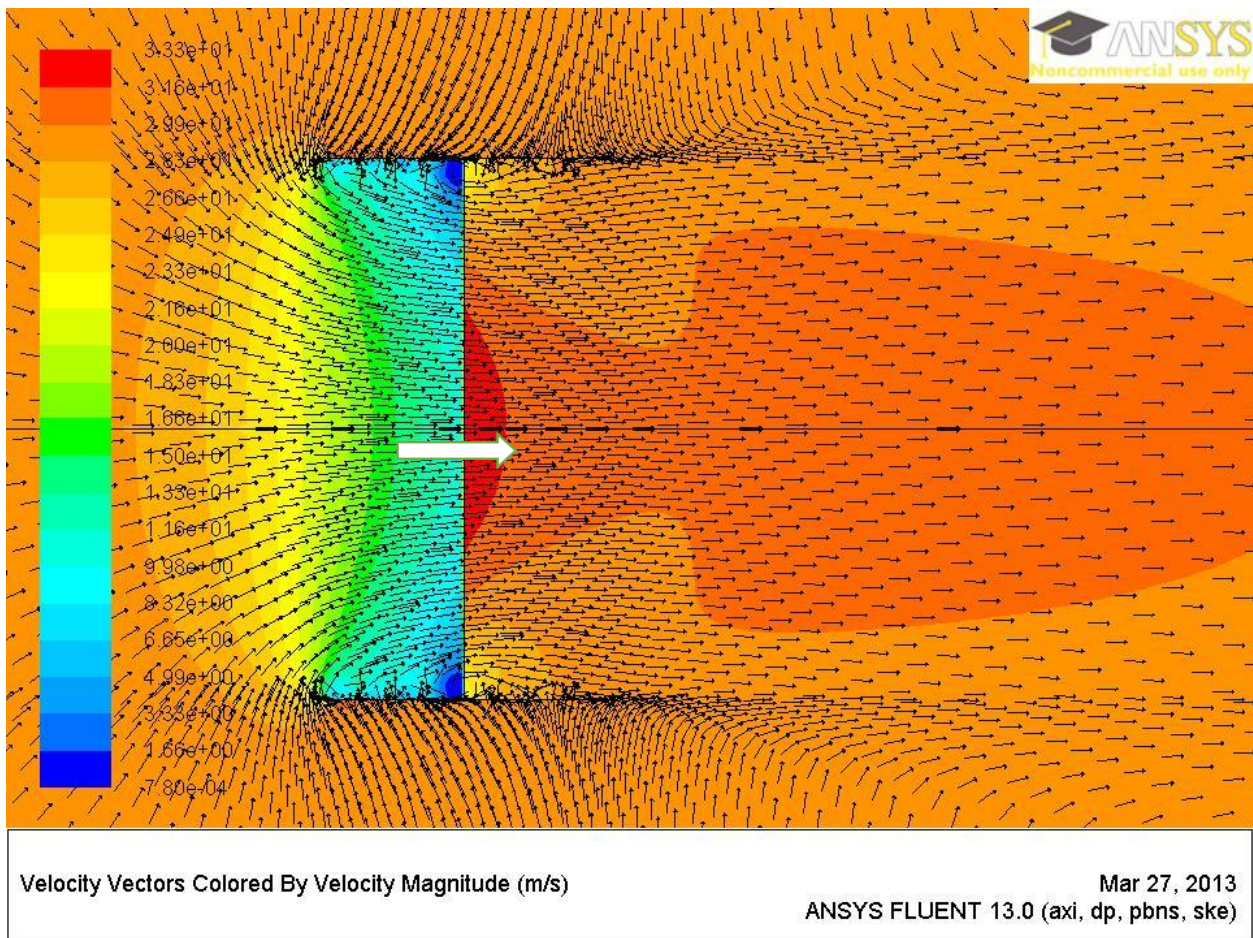


Figure 5-7 Case 3 - velocity vectors on pressure contour

As seen in the picture above, the flow is similar to the case with 4-pores. The tip loss is seen, and the flow in coming into the duct. There can be seen a huge pressure gradient right at the propeller disc.

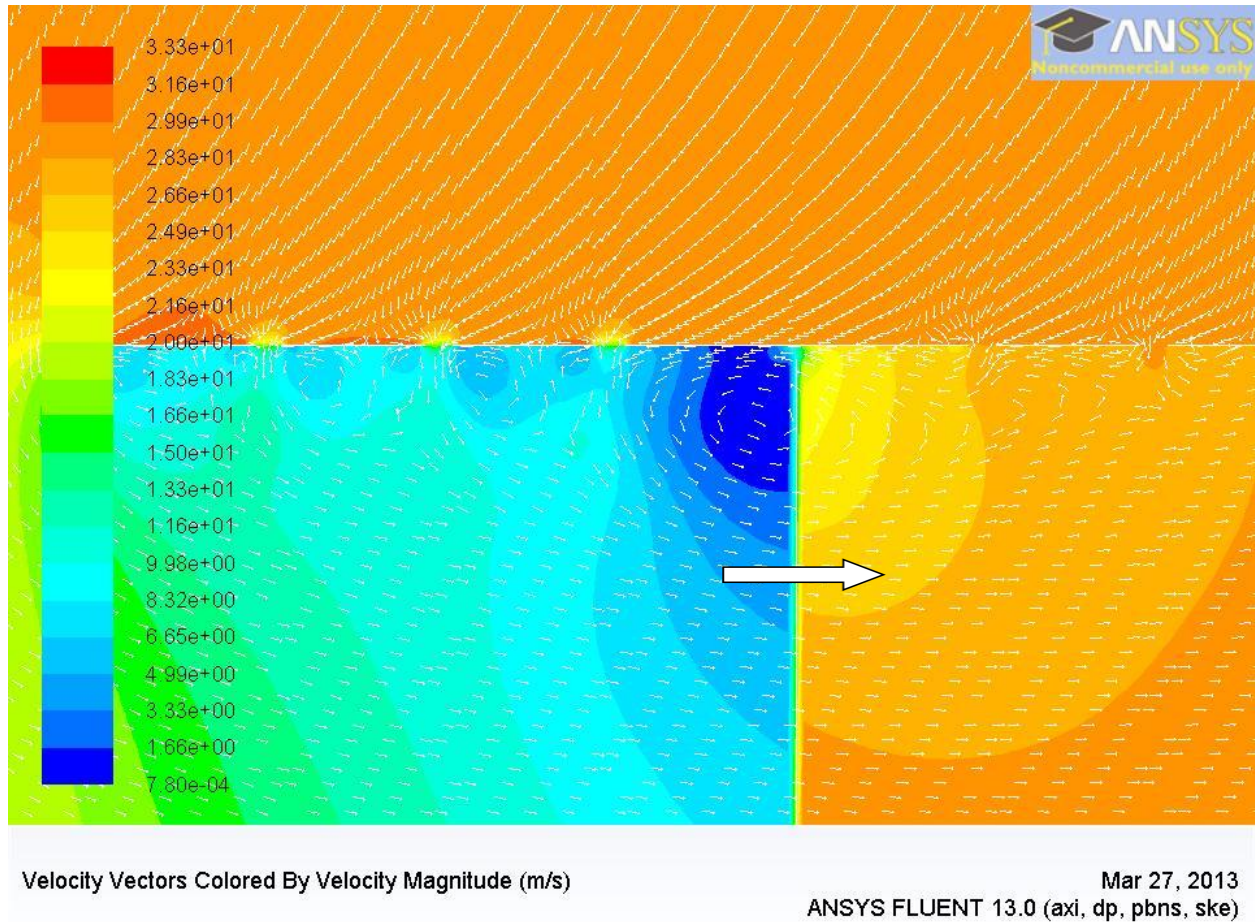


Figure 5-8 case 3: closer look inside the duct

Looking closely in one side of the duct, flow in this case is similar to the case with 4 pores. The flow is coming in through each pore. The air flows top to bottom through the fan. The mass flow rate at the top of the duct is 1.23 kg/s and the mass flow rate at the bottom is 1.41 kg/s. What is interesting here is that the mass flow rate at the top went down and the mass flow rate at the bottom remained the same. This is because the propeller have a limited energy, and the total mass it is moving per second is 1.41 kg/s.

8-Perforations

The visual results of the case with 8 pores on each side is very similar to the one with 4-pores and 6-pores. Most of the pressure gradient is around the ducts, and there isn't too much going on the rest of the domain. The fluid flow behavior similar to the above mentioned two cases with tip loss, and flow through the duct.

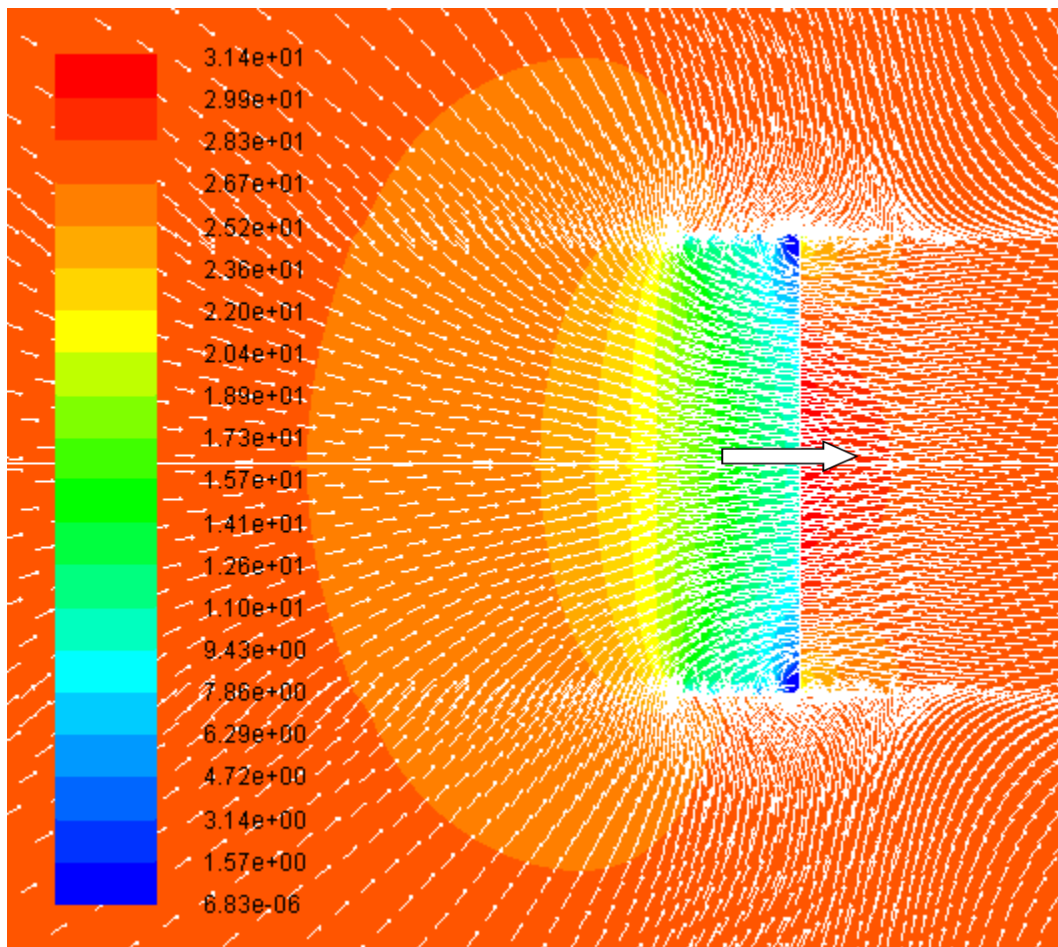


Figure 5-9 case 4 Duct Area

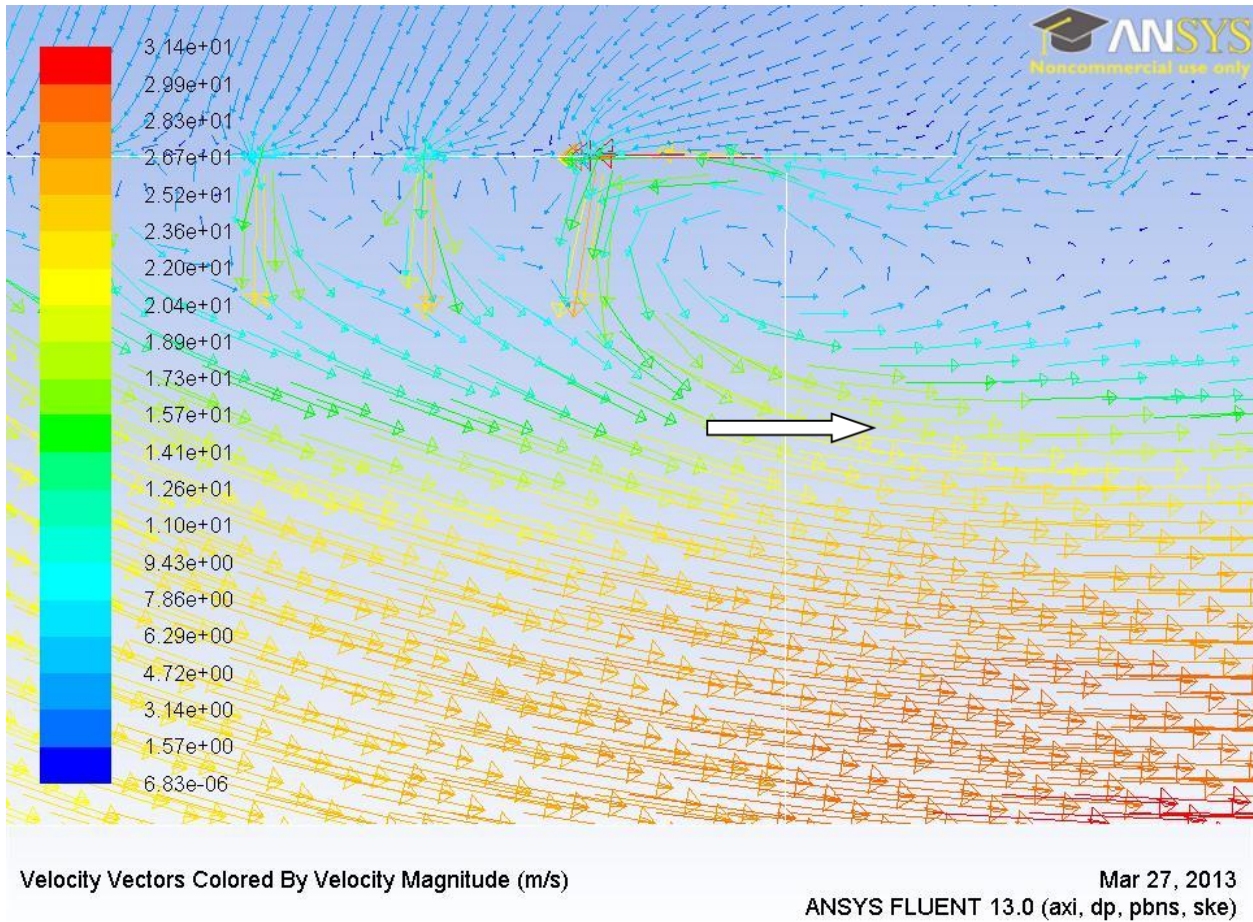


Figure 5-10 Case 4 - closer look inside the duct

The picture above shows the velocity vectors. It can be noticed that the air flow patterns are similar to the cases above.

Results

Next the results from each case described above are tabulated below.

Table 5 : Results for 6000 Pa Pressure input

Case	Open Area of the duct	Pressure input	Area for calculating thrust	Max Velocity	Pressure Force	Mom. Flux	Pressure Force	Mom. Flux	Thrust Produced	Duct Weight	Net Thrust	Efficiency	Ct
		Pa	m ²	m/s	N	N	N	N	N	N	N	%	
1	0%	6000	0.1110	95.4	-1.603	-307.604	-278.654	304.954	275.701	1.716	273.985	90%	0.223
2	8%	6000	0.1134	95.1	-4.106	-306.179	-216.997	242.166	276.905	1.579	275.326	91%	0.220
3	12%	6000	0.1075	94.4	-2.795	-305.276	-187.056	210.834	278.702	1.510	277.191	91%	0.237
4	16%	6000	0.1134	93.8	-0.873	-303.417	-164.231	186.463	280.313	1.442	278.871	92%	0.229
5	24%	6000	0.1134	93.8	0.649	-297.935	-142.073	157.902	282.756	1.304	281.451	93%	0.231
6	36%	6000	0.1110	93.2	4.283	-298.875	-99.750	121.448	283.500	1.098	282.402	93%	0.240
7	40%	6000	0.1110	93.2	3.761	-299.430	-94.691	112.381	285.500	1.030	284.470	94%	0.242
8	48%	6000	0.1110	93.1	6.674	-296.702	-76.117	96.084	286.409	0.892	285.517	94%	0.243
9	60%	6000	0.1110	93.2	7.984	-295.528	-62.912	78.218	288.206	0.687	287.519	95%	0.244
10	80%	6000	0.1075	93.5	12.903	-290.791	-44.157	57.197	290.654	0.343	290.311	95%	0.252
11	96%	6000	0.1134	92.9	16.509	-288.768	-36.440	53.721	287.996	0.069	287.927	95%	0.240
12	100%	6000	0.1257	88.5	31.188	-288.617	-46.613	71.385	297.610	0.000	297.610	98%	0.247

As it can be seen in table 5, the thrust was found to be increasing as perforations were added in the duct. The efficiency of the case with no duct was found to be the highest. The maximum velocity was around 95m/s. That is a lot of speed of air. The speed of air increased with the addition of duct.

Table 6 Results for 3000 Pa pressure input

Case	Open Area	Pressure input	Area for calculating thrust	Max Velocity	Bottom		Top		Thrust Produced	Duct Weight	Net Thrust	Efficiency	Ct
					Pressure Force	Mom. Flux	Pressure Force	Mom. Flux					
		Pa	m ²	m/s	N	N	N	N	N	N	N	%	
1	0%	3000	0.0507	67.4	-0.323	-151.448	-133.344	146.679	137.790	1.716	136.074	90%	0.230
2	8%	3000	0.1075	67.2	-2.023	-152.970	-108.431	121.094	138.284	1.579	136.705	90%	0.232
3	12%	3000	0.1075	66.7	-1.405	-152.618	-93.639	105.515	139.337	1.510	137.826	91%	0.238
4	16%	3000	0.1075	66.3	-0.426	-151.684	-82.078	93.296	140.039	1.442	138.597	91%	0.235
5	24%	3000	0.1134	66.0	0.412	-150.534	-71.060	80.853	141.152	1.304	139.847	92%	0.233
6	36%	3000	0.1257	65.8	1.749	-149.304	-52.667	61.042	142.679	1.098	141.580	93%	0.234
7	40%	3000	0.1075	65.8	1.884	-149.699	-47.442	56.359	142.665	1.030	141.635	93%	0.250
8	48%	3000	0.1122	65.7	2.983	-148.254	-40.351	48.351	143.236	0.892	142.344	94%	0.241
9	60%	3000	0.1075	65.8	4.004	-147.751	-31.531	39.257	144.029	0.687	143.343	94%	0.253
10	80%	3000	0.1075	66.1	6.438	-145.371	-22.228	28.726	145.312	0.343	144.969	95%	0.253
12	100%	3000	0.1195	62.4	15.850	-144.276	-23.154	35.763	147.518	0.000	147.518	97%	0.259

Similar effects can be observed in cases with 3000 Pa input pressure. The cases with no duct were found to be the most efficient and created the most thrust. The maximum speed of the air was seen to increase with the addition of duct.

Table 7 Results for 60 Pa Pressure input

Case	Open Area	Pressure input	Area for calculating thrust	Max Velocity	Bottom		Top		Thrust Produced	Duct Weight	Net Thrust	Efficiency	Ct
					Pressure Force	Mom. Flux	Pressure Force	Mom. Flux					
		Pa	m2	m/s	N	N	N	N	N	N	N	%	
1	0%	60	0.0507	9.37	-0.011	-3.020	-2.655	2.935	2.729	1.716	1.012	33%	0.224
2	8%	60	0.1134	9.13	-0.036	-3.016	-2.214	2.446	2.749	1.579	1.170	38%	0.237
3	12%	60	0.1099	9.36	-0.027	-3.053	-1.879	2.116	2.789	1.510	1.279	42%	0.237
4	16%	60	0.1064	9.31	-0.007	-3.034	-1.644	1.870	2.802	1.442	1.360	45%	0.248
7	40%	60	0.1075	8.98	0.030	-2.957	-1.066	1.216	2.836	1.030	1.806	59%	0.267
9	60%	60	0.1075	9.00	0.073	-2.916	-0.745	0.867	2.868	0.687	2.181	72%	0.269
10	80%	60	0.1075	9.07	0.122	-2.866	-0.544	0.636	2.897	0.343	2.554	84%	0.267
12	100%	60	0.1257	8.43	0.353	-2.865	-0.547	0.832	2.933	0.000	2.933	96%	0.268

Very similar results can be seen with the case with 60 lbs. The weight of the aluminum was a lot higher than the thrust produced. Hence the efficiency was greatly deteriorated by the addition of the thrust.

The tables in the following pages show the variation of the Thrust with increasing % Open Area for the three result cases that are tabulated above.

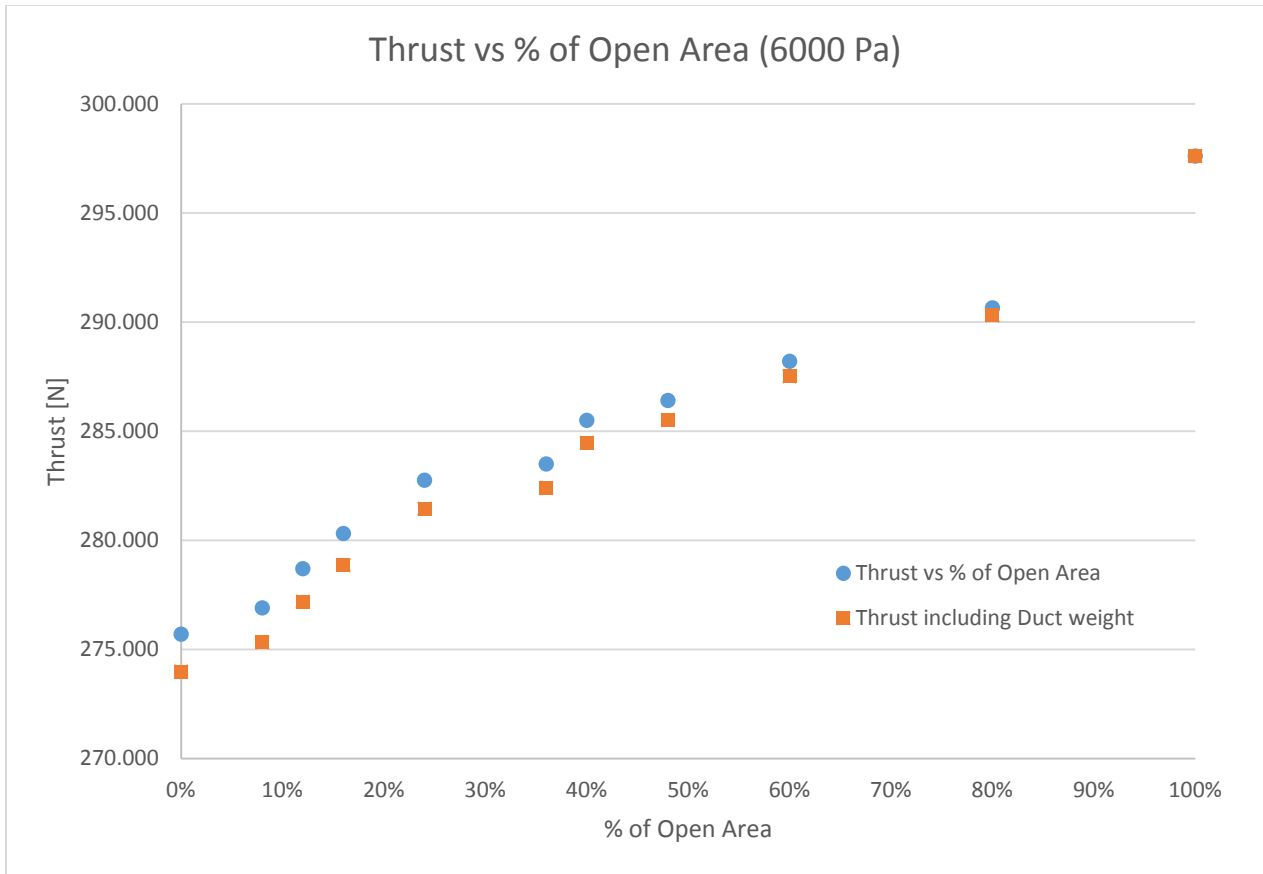


Figure 5-11 variation of net Thrust with % of open area in the duct for cases with 6000

Pa after duct weight is subtracted from the thrust

From the figure above, it can be seen that the thrust increases as the % of Open area is increased. This is because as the amount of duct surface is decreased, the drag provided by the duct decreases as well ultimately responsible decreasing the thrust. The total decrease in thrust by addition of duct was about 22N. Addition of ducts produced 7% less thrust. When the duct weight was included, from the image above, it can be seen that the thrust is lowered with the addition of duct.

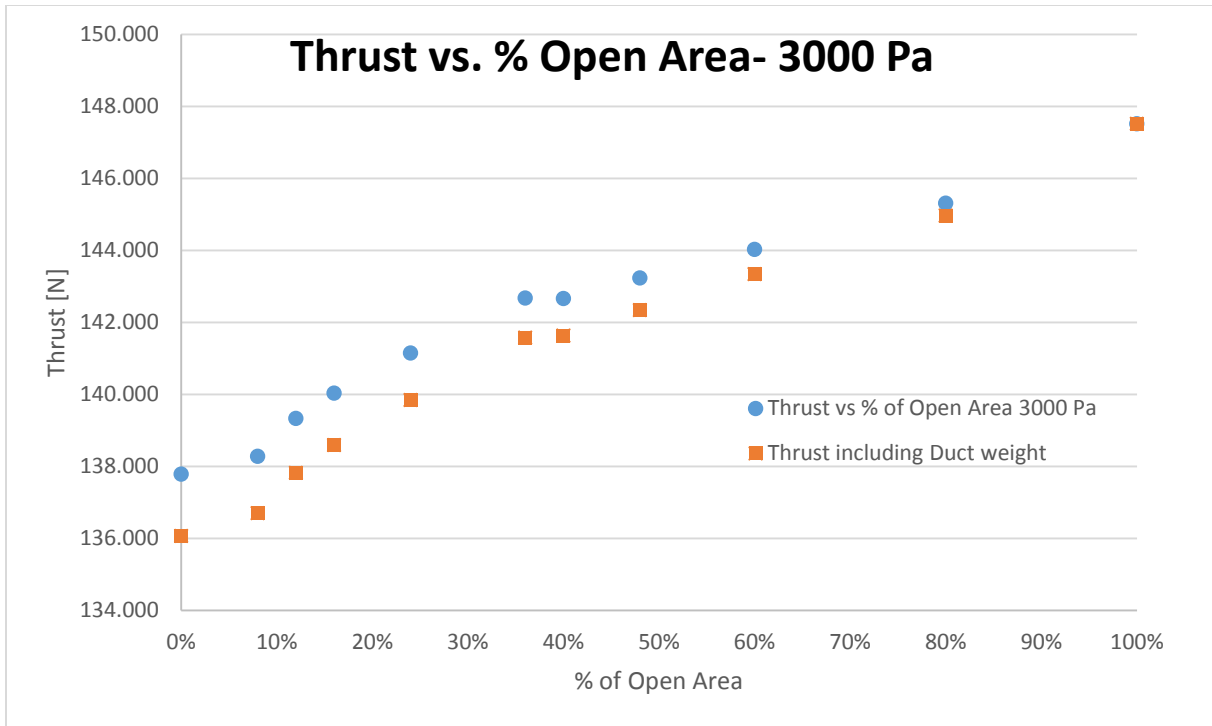


Figure 5-12 variation of net Thrust with % of Open Area for cases with 3000 Pa after duct weight is subtracted from the thrust

From the cases with 3000 Pa Pressure Difference, it can be seen that the thrust increases as the % of Open area is increased just like in the case with 6000 Pa. The loss in thrust is more when the duct weight is included. The slope of the line decreases slightly after about 30% open area here too. The total decrease in thrust by addition of duct was about 10N. The ducted propellers produce around 7% less thrust than the free propellers.

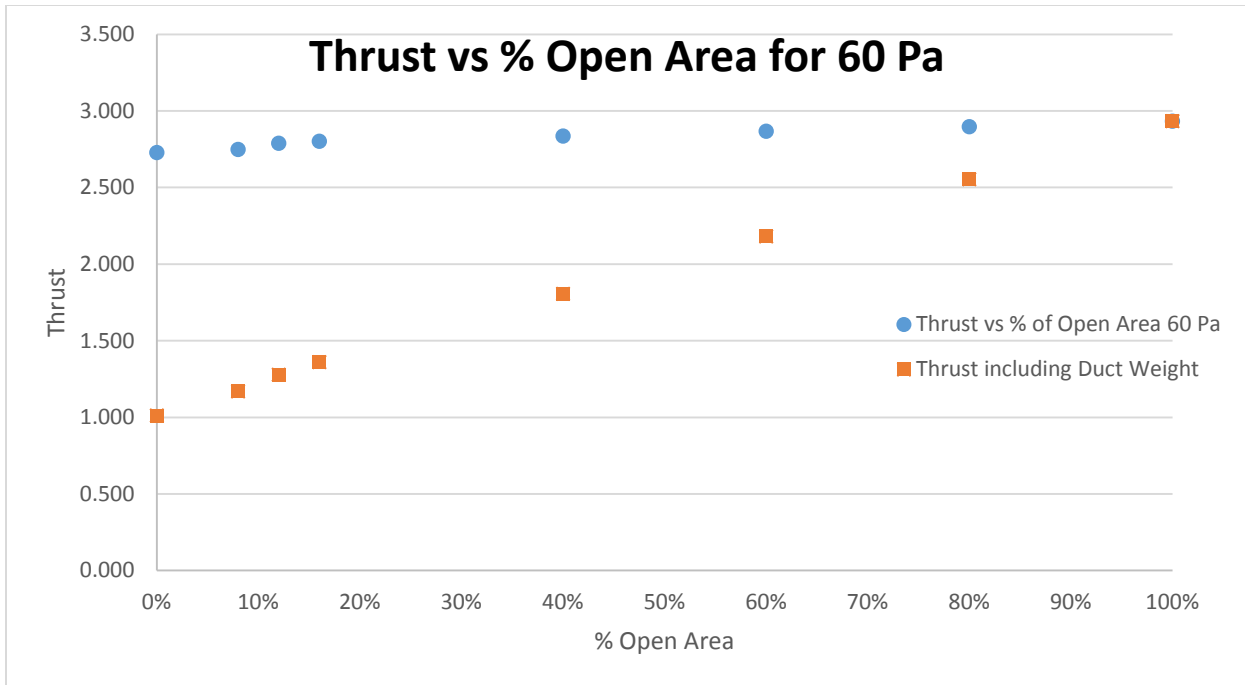


Figure 5-13 Variation of net Thrust with % of Open Area for cases with 60 Pa after duct weight is subtracted from the thrust

From the cases with 60 Pa Pressure Difference, it can be seen that the thrust increases as the % of Open area is increased just like in the case with 6000 Pa and 3000 Pa., For this case, when duct weight is included in the calculations, the difference in thrust is a lot more significant. The slope of the line decreases slightly after about 20% open area here. The total decrease in thrust by addition of duct was about 0.2 N. The ducted propellers produced around 7% less thrust than the free propellers.

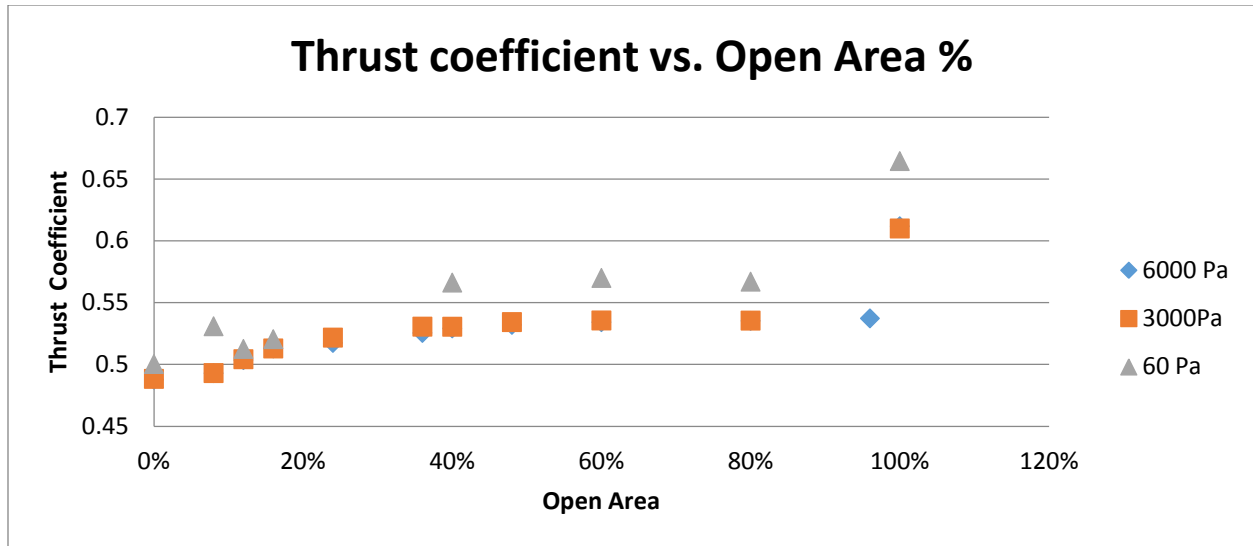


Figure 5-14: Thrust Coefficient vs Open Area %

Figure 5-14 above shows the variation of thrust coefficient with the % of Open Area. As it can be noticed in all three cases, the thrust coefficient doesn't change much between 30% to 70% open area. This area of no thrust change can be taken advantage to optimize the design, weather it is to provide more protection for the same thrust, or to decrease the material.

One of the major concerns of the results is the fact that the result shows that the thrust produced by the ducts is less than the thrust produced by the free propellers at both high speeds (6000 Pa and 3000 Pa) and low speed (60 Pa). This is counter to the past research as mentioned in Chapter 1 (Martin, 2004). This discrepancy with the past experimental data prompts a further investigation on finding the reasons that would have caused such difference. The first clue lies on the multiple flow separations occurring adjacent to the duct wall in the case of ducted fan. Since flow separation is well known as a culprit for producing entropy, resulting in increased aerodynamic losses and instability, it is then speculated that the flat geometry of the duct used in this study could be the reason causing the

discrepancy between simulation conducted by this study and the experimental result because the duct shape in the NASA experiment was based on a cambered airfoil as shown in Figure 5-15 below.

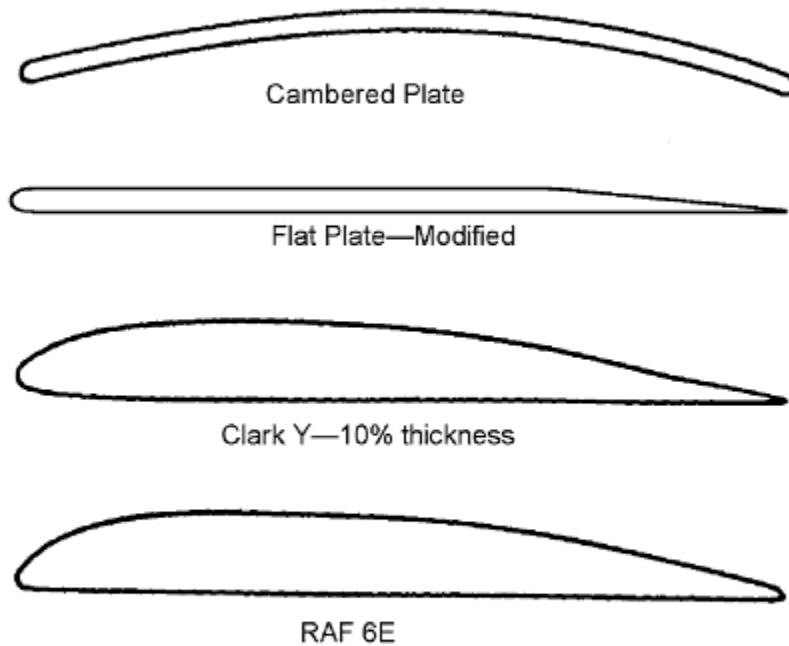


Figure 5-15: Different types of Duct Shape (Wright Jr and Piolene 2002)

In this study, a careful job was done to make sure that the results are consistent, the model is appropriate and computational uncertainties are systematically minimized by conducting the grid sensitivity, computational domain sensitivity study, boundary conditions sensitivity study, thrust calculation area sensitivity study etc. Therefore, in order to further investigate the discrepancy between

this computational simulation with the experimental data, it is recommended that ducts with various cambered airfoil configuration be conducted in future studies.

Conclusions:

A 2-D CFD simulation was conducted to investigate whether the hypothesis of adding perforations to (or removing material from) the propeller duct can benefit from a net thrust gain in comparison of no-duct free propellers. The conclusions are:

1. A computational mode was successfully developed and implemented by modeling the propeller with a pressure jump across a actuate disc with an infinitesimal small thickness.
2. In contrast to the previous experimental results, adding duct to a free propeller does not increase but reduces the thrust even when the weight is not considered.
3. Both gross and next thrusts increase as more perforations are added on the ducts. More net thrust is gained as more perforations are added (i.e. more duct weight is reduced) until the maximum thrust is achieved for the no-duct free propeller.
4. More gross thrust is gained with more perforations could be explained with the fact that small jets produced by the perforations actually reduce the adverse effect of multiple flow separations.
5. The dimensionless thrust remains almost constant between 40%-80% perforations. This region can be conveniently used during design of ducted propellers.
6. The discrepancy between the present simulation results and the previous experimental results is suspected being caused by not having the cambered airfoil duct wall configuration because NASA's experiments used cambered airfoil duct wall while the flat-wall configuration used in this study has generated multiple flow separation. Further study is recommended to continue

more detailed computational simulation using a duct with cambered airfoil configuration to reduce the aerodynamic losses.

BIBLIOGRAPHY

2011. *A robot that flies like a bird*. http://www.ted.com/talks/a_robot_that_flies_like_a_bird.html.

Airforce, Wright Patterson. 2012. *AirForce Research Laboratory*. <http://www.wpafb.af.mil/afri/>.

Ansys. 2013. "Ansys Help - Theory Manual." Ansys.

Boyle, Rebecca. 2012. *PopSci*. <http://www.popsci.com/technology/article/2012-04/video-flying-shape-thing-propels-itself-flipping-inside-out>.

Dixon, S.L, and C.A Hall. 2010. *Fluid Mechanics and Thermodynamics of Turbomachinery*. 6th. Butterworth-Heinemann .

Festo. 2012. *smart bird - bird flight deciphered*. http://www.festo.com/cms/en_corp/11369.htm.

Forman, Erick. 2012. *Eric Forman Blog*. April 25. <http://www.ericforman.com/blog/smart-inversion-flying-inflatable-shape-by-festo/>.

Galante, Nick. 2001. *Helios Prototype*. NASA. July 14. <http://www.dfrc.nasa.gov/Gallery/Photo/Helios/Large/ED01-0209-3.jpg>.

HobbyKing. 2013. 02 10. http://www.hobbyking.com/hobbyking/store/__18120__Turnigy_Aerodrive_SK3_3542_1185kv_Brushless_Outrunner_Motor.html.

James, Gregory K. 2000. "Unmanned aerial vehicles and special operations: Future direction." Masters Thesis, Aeronautics and astronautics, University of Washington.

Joblin, Steve. 2100. *RCGroups*. Jan 16. <http://www.rcgroups.com/forums/showthread.php?t=1335765&page=21>.

Martin, Preston, and Chee Tung. 2004. *Performance and Flowfield Measurements on a 10-inch Ducted Rotor VTOL UAV*. California: Ames Research Center, Moffett Field.

Martin, Preston, and Chee Tung. 2004. *Performance and Flowfield Measurements on a 10-inch Ducted Rotor VTOL UAV*. pdf document. Ca: NASA Rotorcraft Division.

MIT. 1997. "Theory of Flight." *web.mit.edu*. March 16. <http://web.mit.edu/16.00/www/aec/flight.html>.

Munson, Bruce R, Donald F Young, and Theodore H Okiishi. 2008. *Fundamentals of FLuid Mechanics*. 3e. New York: John Wiley & Sons. Inc. Accessed 01 2013.

NASA. n.d. *Nasa.gov*. <http://www.nasa.gov/centers/dryden/news/FactSheets/FS-034-DFRC.html>.

Nick, Carlos, Gabe, Chris. 2013. *kickstarter.com*. 1. <http://www.kickstarter.com/projects/1671680066/incredible-hlq-heavy-lift-quadcopter>.

n.d. *Open Course Ware MIT - Unified Propulsion*. Accessed 12 15, 2012. <http://ocw.mit.edu/ans7870/16/16.unified/propulsionS04/UnifiedPropulsion9/UnifiedPropulsion9.htm>.

Piasecki Aircraft Corporation. 2009. *X-49A SpeedHawk*. <http://www.piasecki.com/x49a.php>.

Scott, Jeff. 2001. *AeroSpaceweb.org*. July 29. <http://www.aerospaceweb.org/question/aerodynamics/q0037.shtml>.

Seddon, John, and Simon Newman. 2011. *Basic Helicopter Aerodynamivs*. John Wiley & Sons Ltd.

Solon, Olivia. 2013. *Wired.com*. 03. <http://www.wired.co.uk/news/archive/2013-03/27/iranian-rescue-robot>.

The Muslim Observer. 2010. *The Next Step: A Stealth Drone*. Washington, Jan 4.

<http://muslimmedianetwork.com/mmn/?tag=us-air-force>.

Trimble, Stephen. 2009. *Flightglobal - aviation connected*. May 6.

<http://www.flightglobal.com/news/articles/socom-reveals-plan-to-buy-20-improved-and-renamed-a160t-hummingbirds-326071/>.

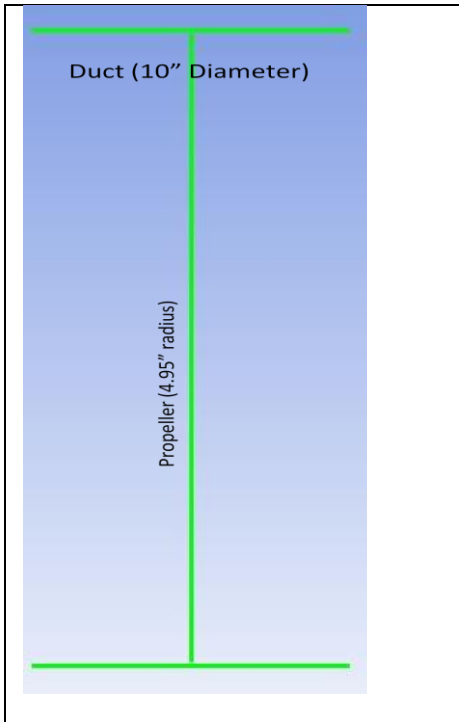
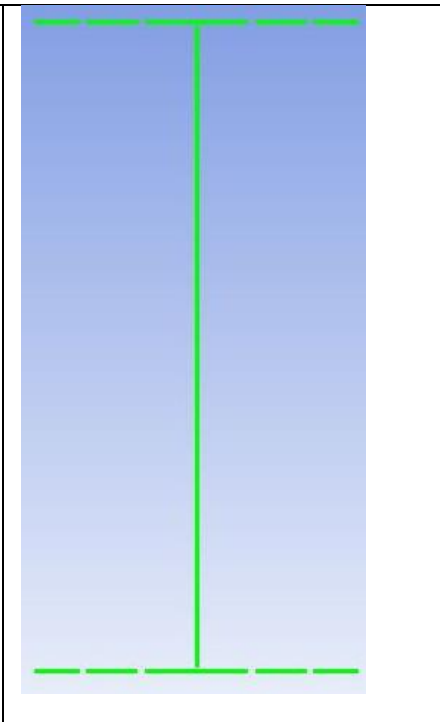
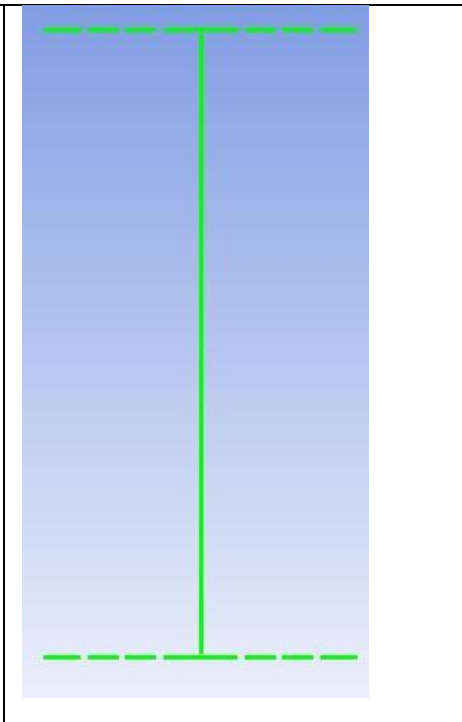
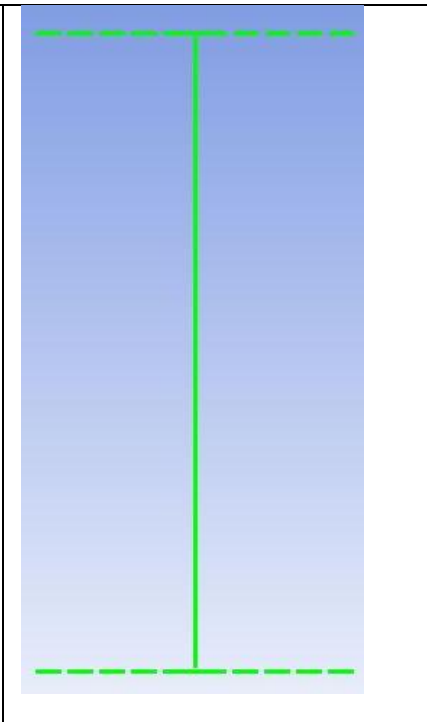
Tzafestas, S.G. 2007. "Advances in Unmanned Aerial Vehicle." *Intelligent Systems, controls, and automation: Science and Engineering*.

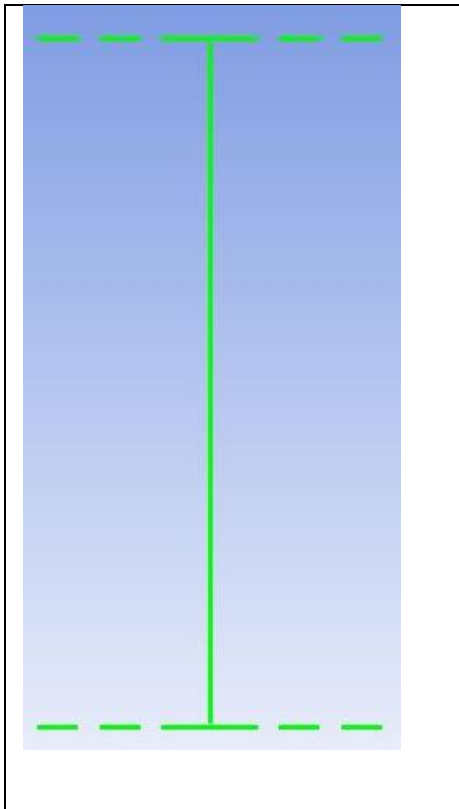
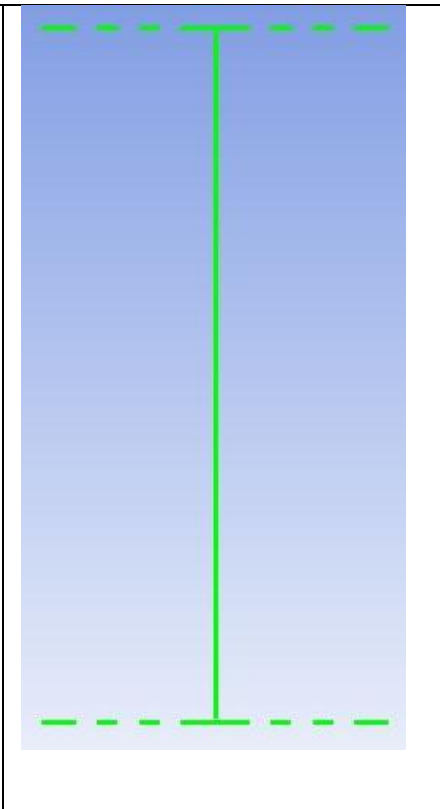
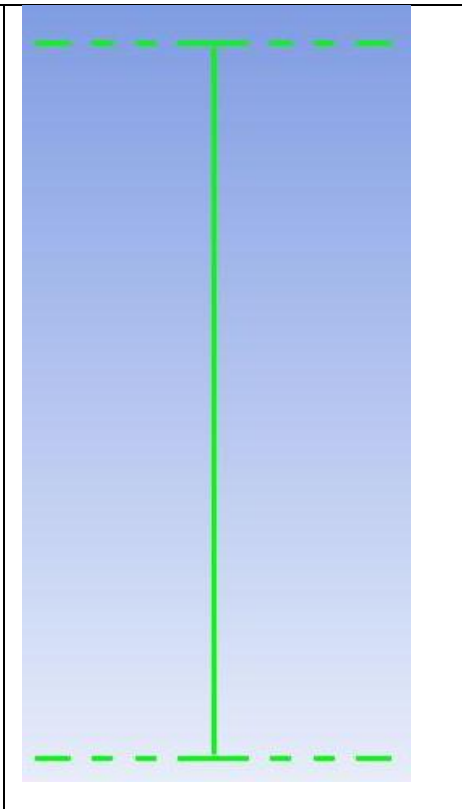
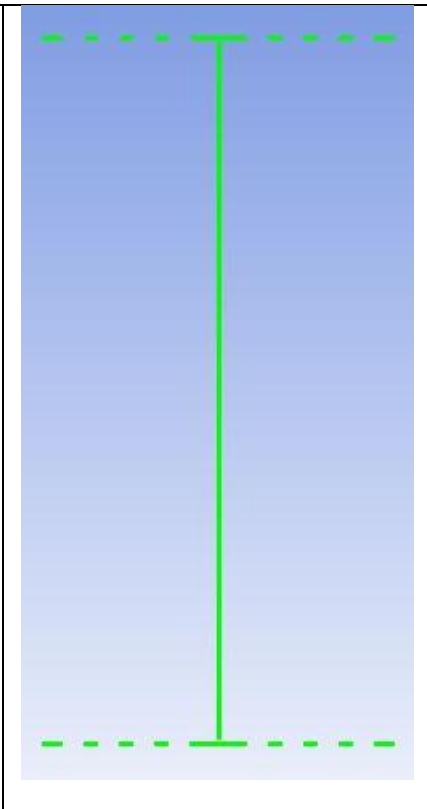
Wright Jr, George E., and E. Marc de Piolene. 2002. *Ducted Fan Design*. Millennial year Ed. Mass Flow.

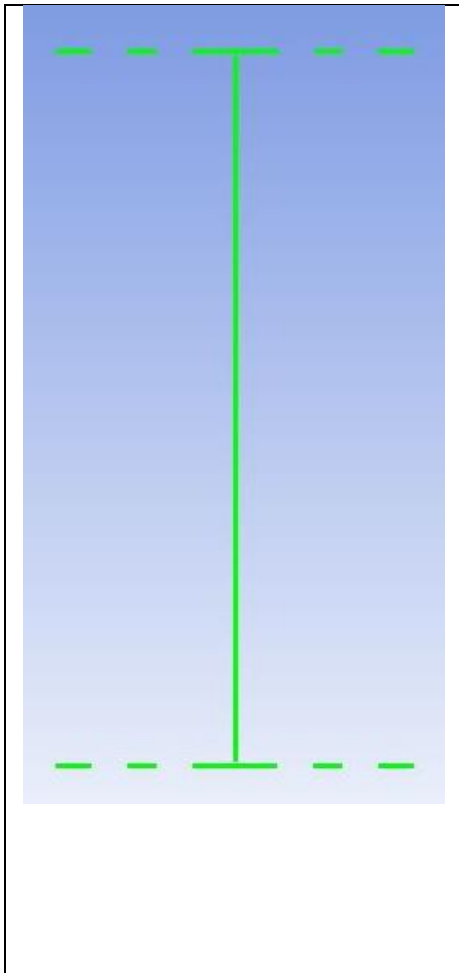
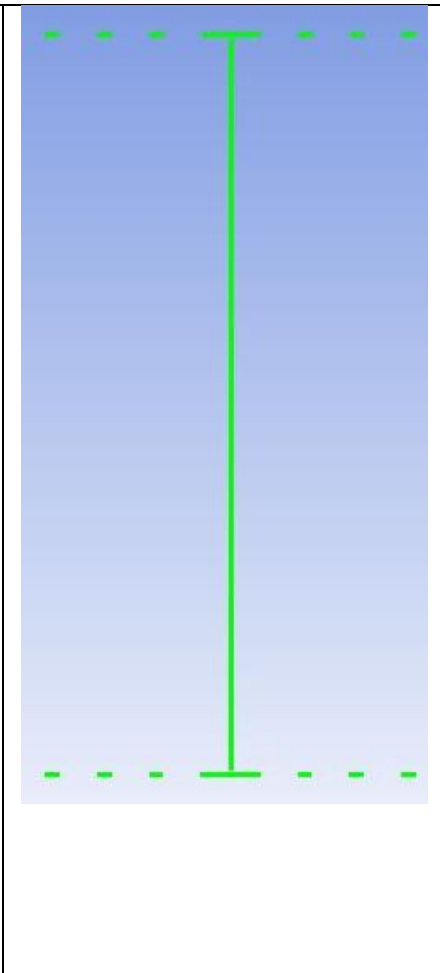
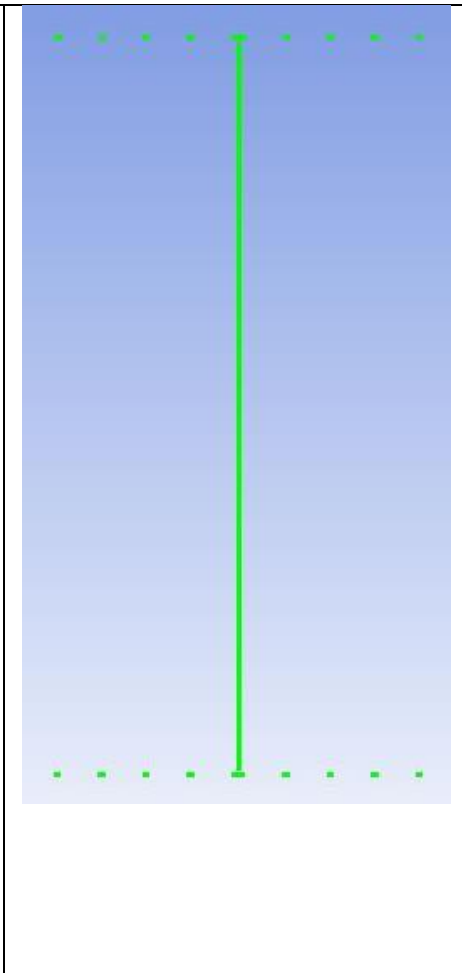
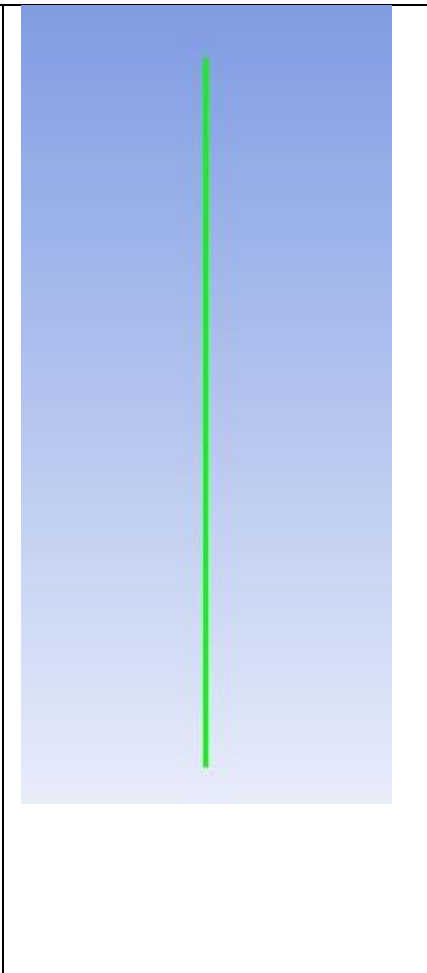
Chapter 6 : APPENDICES

Appendix I: Different Cases

The images of different cases is shown in the figures below.

 <p>Duct (10" Diameter)</p> <p>Propeller (4.95" radius)</p>			
<p>Figure 6-1 Duct with no Pores</p>	<p>Figure 6-2: Duct with four 0.1" Pores</p>	<p>Figure 6-3 Duct with six 0.1" Diameter Pores</p>	<p>Figure 6-4 Eight 0.1" Diameter Pores</p>

			
<p>Figure 6-5: Duct with four 0.3" Pores</p>	<p>Figure 6-6: Duct with four 0.3" Pores</p>	<p>Figure 6-7 Duct with six 0.3" Pores</p>	<p>Figure 6-8 Duct with Eight 0.3" Diameter Pores</p>

 <p>A vertical green line representing a duct is centered within a blue rectangular area. At the top and bottom of the duct, there are four short horizontal green dashes, representing pores. The dashes are arranged in two pairs, one pair at the top and one pair at the bottom, with a small gap between the two dashes in each pair.</p>	 <p>A vertical green line representing a duct is centered within a blue rectangular area. At the top and bottom of the duct, there are six short horizontal green dashes, representing pores. The dashes are arranged in two groups of three, one group at the top and one group at the bottom, with a small gap between the three dashes in each group.</p>	 <p>A vertical green line representing a duct is centered within a blue rectangular area. At the top and bottom of the duct, there are eight small green dots, representing pores. The dots are arranged in two groups of four, one group at the top and one group at the bottom, with a small gap between the four dots in each group.</p>	 <p>A single vertical green line representing a propeller is centered within a blue rectangular area. There are no horizontal dashes or dots at the top or bottom of the line, indicating no duct or pores.</p>
<p>Figure 6-9 Duct with four 0.5" Pores</p>	<p>Figure 6-10 Duct with six 0.5" Pores</p>	<p>Figure 6-11: Duct with eight 0.5" Diameter Pores</p>	<p>Figure 6-12 Propeller with no duct</p>

Appendix II: CFD Training

CFD: CFD is acronym for Computational Fluid Dynamics. CFD is a numerical method to solve and analyze problems that involve fluids flows. CFD software called FLUENT was used to solve the problems also to study effects of perforated ducts. The fluent training was divided into three parts:

1. Laminar Channel Flow (Flow between Fixed Parallel Plates)
2. Laminar Pipe Flow
3. Turbulent Pipe Flow

Laminar Channel Flow

The first part of the initial training in Fluent CFD was analyzing Channel Flow or the flow between fixed infinite Parallel Plates. The same basic problem statement was solved with different number of nodes. The Problem Statement is as follows:

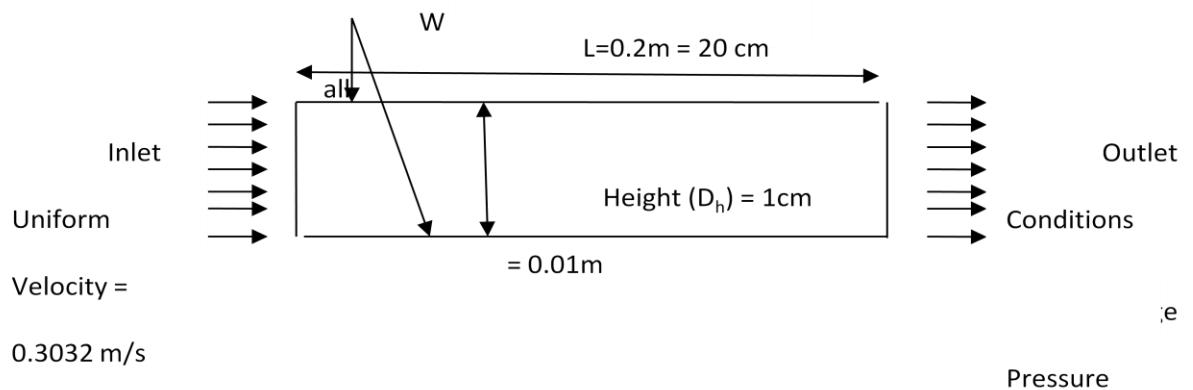


Figure 6-13: Channel Flow with Boundary Conditions at $T=20^\circ\text{C}$

Properties of air:

Density used (ρ): 1.204 kg/m³

Dynamic Viscosity (μ): 1.825 * 10⁻⁵ kg/ (m-s)

Reynolds Number:

Reynolds number is given by

$$Re_D = \frac{v D}{\nu} \quad (5 - 1)$$

Where, at Temperature = 20° C

v = velocity of the fluid = 0.3032 m/s

D = Height = 0.01 m

ν = Kinematic Viscosity = 1.516 * 10⁻⁵ $\frac{m^2}{s}$

Then,

$$Re_D = \frac{v * D}{\nu} = \frac{0.3032 * 0.01}{1.516 * 10^{-5}} = 200$$

The Flow is laminar.

Analytical Solution:

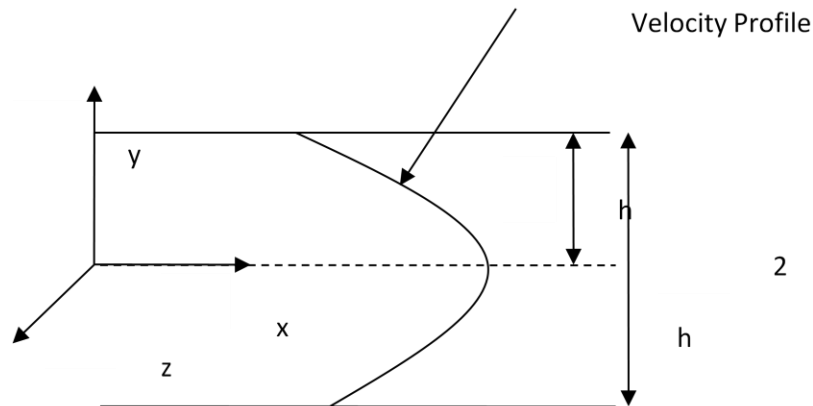


Figure 6-14: Channel geometry to calculate the velocity profile

Navier-stokes Equations are used to solve the fluid flow problem. They are given as:

$$\rho \left(\frac{\partial u}{\partial t} + u \frac{\partial u}{\partial x} + v \frac{\partial u}{\partial y} + w \frac{\partial u}{\partial z} \right) = -\frac{\partial p}{\partial x} + \rho g_x + \mu \left(\frac{\partial^2 u}{\partial x^2} + \frac{\partial^2 u}{\partial y^2} + \frac{\partial^2 u}{\partial z^2} \right) \quad (\text{x-direction}) \quad (5-2)$$

$$\rho \left(\frac{\partial v}{\partial t} + u \frac{\partial v}{\partial x} + v \frac{\partial v}{\partial y} + w \frac{\partial v}{\partial z} \right) = -\frac{\partial p}{\partial y} + \rho g_y + \mu \left(\frac{\partial^2 v}{\partial x^2} + \frac{\partial^2 v}{\partial y^2} + \frac{\partial^2 v}{\partial z^2} \right) \quad (\text{y-direction}) \quad (5-3)$$

$$\rho \left(\frac{\partial w}{\partial t} + u \frac{\partial w}{\partial x} + v \frac{\partial w}{\partial y} + w \frac{\partial w}{\partial z} \right) = -\frac{\partial p}{\partial z} + \rho g_z + \mu \left(\frac{\partial^2 w}{\partial x^2} + \frac{\partial^2 w}{\partial y^2} + \frac{\partial^2 w}{\partial z^2} \right) \quad (\text{z-direction}) \quad (5-4)$$

In the Laminar case, there is no flow in the y or z direction, i.e. $v=0$ and $w=0$. The flow is steady, meaning the velocity doesn't change with time. So, all the partial derivatives with respect to time become zero. Hence the Navier-Stokes equations for this case reduce to the following:

$$0 = -\frac{\partial p}{\partial x} + \mu \left(\frac{\partial^2 u}{\partial y^2} \right) \quad (\text{x-direction}) \quad (5-5)$$

$$0 = -\frac{\partial p}{\partial y} + \rho g_y \quad (y - \text{direction}) \quad (5 - 6)$$

$$0 = -\frac{\partial p}{\partial z} \quad (z - \text{direction}) \quad (5 - 7)$$

(5-6) can be integrated to get:

$P = -\rho g y + C$, This tells us that Pressure varies in y direction only.

(5-5) can be rewritten as:

$$\frac{1}{\mu} \frac{\partial p}{\partial x} = \left(\frac{\partial^2 u}{\partial y^2} \right)$$

Taking $\frac{\partial p}{\partial x}$ as constant from (5-6) and Integrating twice with respect to y,

$$u = \frac{1}{2\mu} \left(\frac{\partial p}{\partial x} \right) y^2 + C_1 y + C_2 \quad (5 - 8)$$

(5-8) is our governing differential equation. To solve it, the boundary conditions are:

$u(y = \pm h) = 0$ (Because of no-slip condition).

Which gives us $C_1=0$ and $C_2 = \frac{1}{2\mu} \left(\frac{\partial p}{\partial x} \right) (y^2 - h^2)$

Thus velocity at any point can be found as:

$$u = -\frac{1}{2\mu} \frac{dp}{dx} (h^2 - y^2) \quad (5 - 9)$$

$$u_{\text{avg}} * 2h = \int_{-h}^{+h} -\frac{1}{2\mu} \frac{dp}{dx} (h^2 - y^2) dy$$

But, $-\frac{1}{2\mu} \frac{dP}{dx}$ is constant so

$$u_{\text{avg}} * 2h = -\frac{1}{2\mu} \frac{dp}{dx} \int_{-h}^{+h} (h^2 - y^2) dy$$

$$u_{\text{avg}} * 2h = -\frac{1}{2\mu} \frac{dp}{dx} [h^3 + h^3 - \frac{h^3}{3} - \frac{h^3}{3}]$$

$$u_{\text{avg}} * 2h = -\frac{1}{2\mu} \frac{dp}{dx} [\frac{h^3 4}{3}]$$

$$u_{\text{max}} = -\frac{1}{2\mu} \frac{dp}{dx} (h^2)$$

$$\frac{u_{\text{avg}}}{u_{\text{max}}} = \frac{2}{3} \quad (5 - 10)$$

This velocity is compared to the profile obtained from Fluent to verify Fluent's solution.

Equations used by Fluent:

The Continuity equation is given by:

$$\frac{\partial \rho}{\partial t} + \nabla \cdot (\rho \bar{v}) = S_m$$

The momentum conservation equation is given by:

$$\frac{\partial}{\partial t} (\rho \bar{v}) + \nabla \cdot (\rho \bar{v} \bar{v}) = -\nabla p + \nabla \cdot (\bar{\tau}) + \rho \bar{g} + \bar{F}$$

Where,

$$\bar{\tau} = \mu \left[\left(\nabla \bar{v} + \nabla \bar{v}^T \right) - \frac{2}{3} \nabla \cdot \bar{v} I \right]$$

Entry Length:

The entry length is the length of the channel where the hydrodynamic boundary layers meet.

$$L_h = 0.05 \cdot \text{Re} \cdot D = 0.1 \text{ m}$$

Friction factor:

The Darcy friction factor can be found from the Reynold's number as:

$$f = 64 / \text{Re} = 64 / 200 = 0.32$$

Iteration 1: Laminar Channel Flow (very few nodes)

We start out with very few nodes.

Problem Statement:

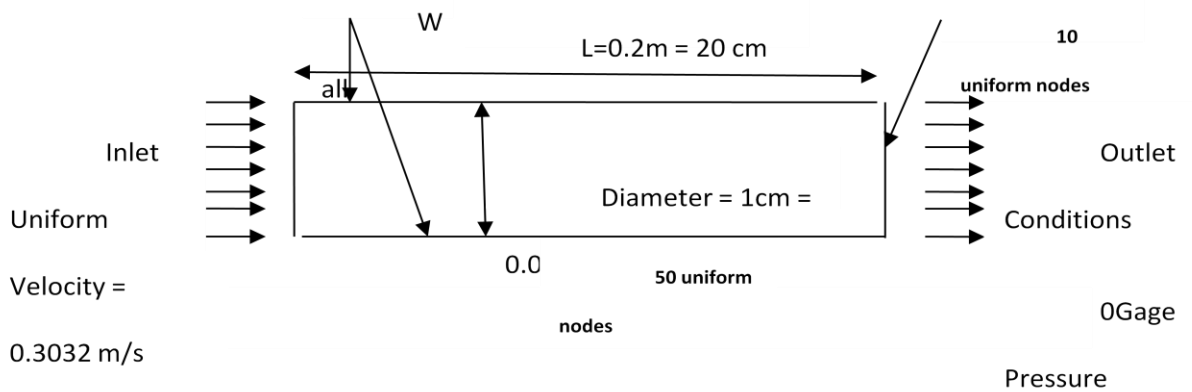


Figure 6-15: Channel Flow with Boundary Conditions

The Mesh was chosen as such to make sure that the a/b ratio was not bigger than 7.

Results:

Velocity Profile Development:

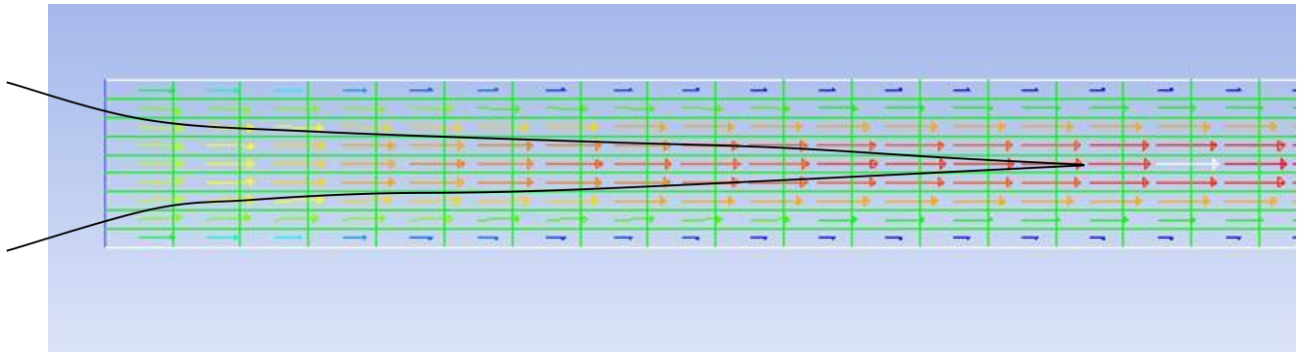


Figure 6-16 : Approximate shape of converging Boundary Layers.

From Figure 6-16, the velocity profiles (given by the velocity vectors) are blunt in the beginning but starts to grow into a parabolic shape. The blue lines are the velocity vectors close to the wall. The velocity near the wall is very small. It is because of the shear stress applied on the fluid because of the no slip condition in the wall.

The velocity profiles are shown in detail in the following figure:

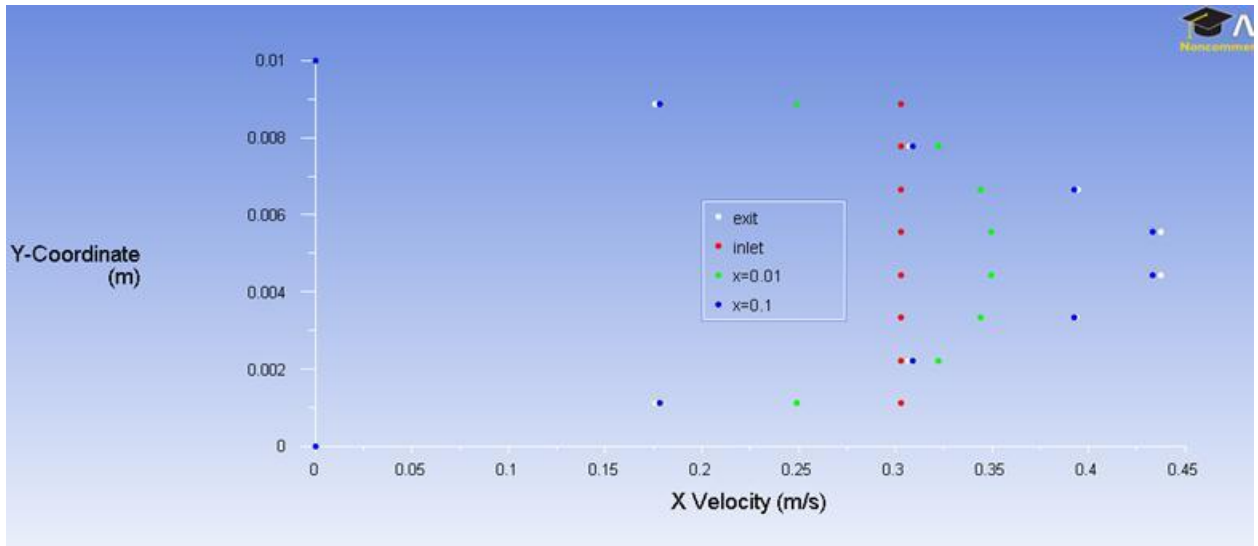


Figure 6-17 :The velocity Profile develops into parabolic velocity profile.

In the figure above, at inlet, the velocity is uniform. As it moves further inside the channel, the profile starts taking the shape of a parabola. The velocity in the center line is the maximum while velocity close to the wall is the smallest. This velocity profile at $x=0.1$ can be compared with the expected velocity profile to check its accuracy.

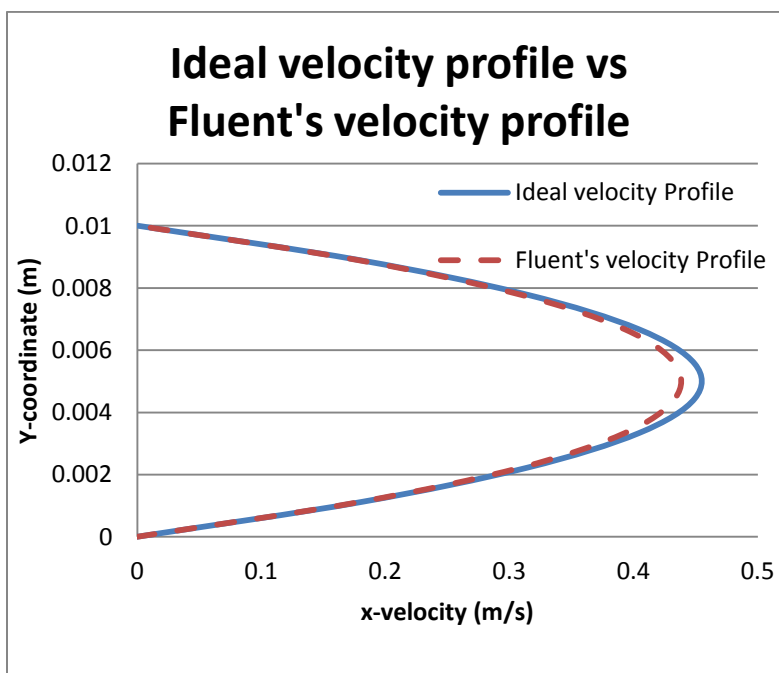


Figure 6-18: Comparison of Ideal velocity profile vs. the velocity profile from Fluent

The Max error in the velocity profile is 3.528%. Since this system has no convective acceleration, exact solution from Navier-Stokes equations is expected.

Next looking at the skin friction coefficient at the walls, the skin friction coefficient decreases all the way to zero; this is not what one would expect.

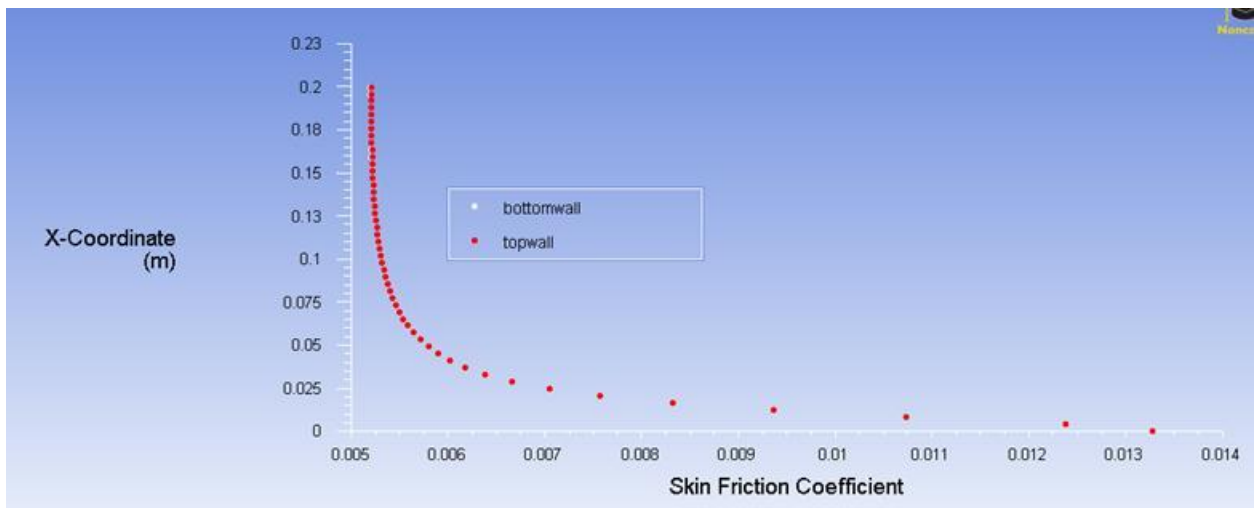


Figure 6-19 : Skin friction-coefficient

The mesh is coarse, and there are no nodes in the center of the channel, because of which the maximum velocity is not fully represented in this iteration. Hence A second iteration is done with more nodes to see if number of nodes matters. The comparative study will be presented at the end.

Iteration 2: Increased Mesh Density

In this iteration the number of nodes is bumped to check if the solution gets better:

Problem Statement:

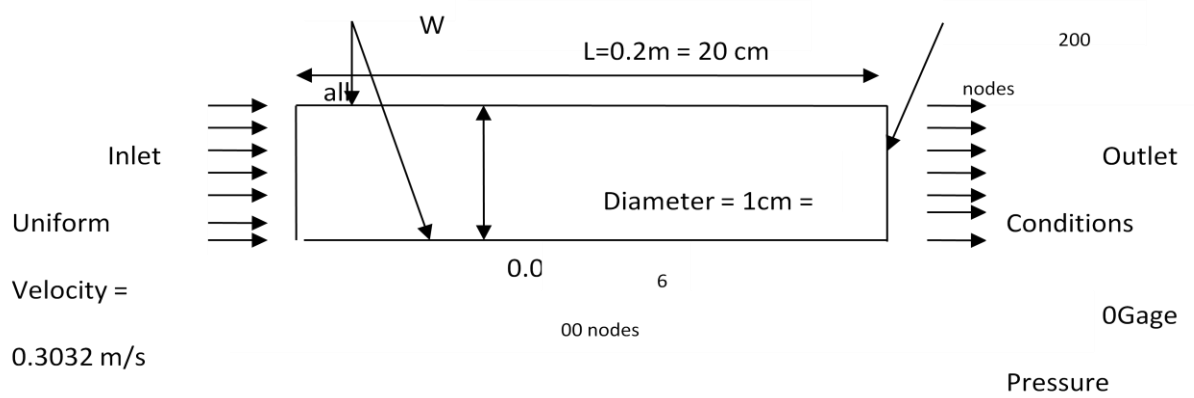


Figure 6-20 : Channel Flow with Boundary Conditions

Results:

For Iteration 2, velocity profile at $x=0.1\text{m}$ is compared with the analytical solution, friction coefficient is observed.

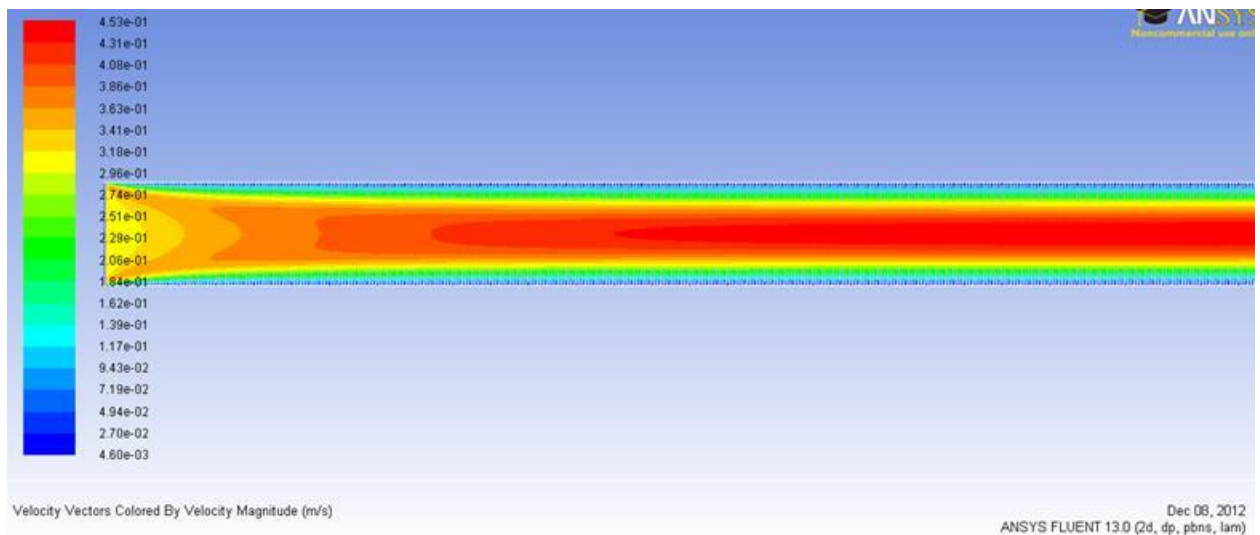


Figure 6-21 : Development of flow.

The velocity profiles at different locations are shown below:

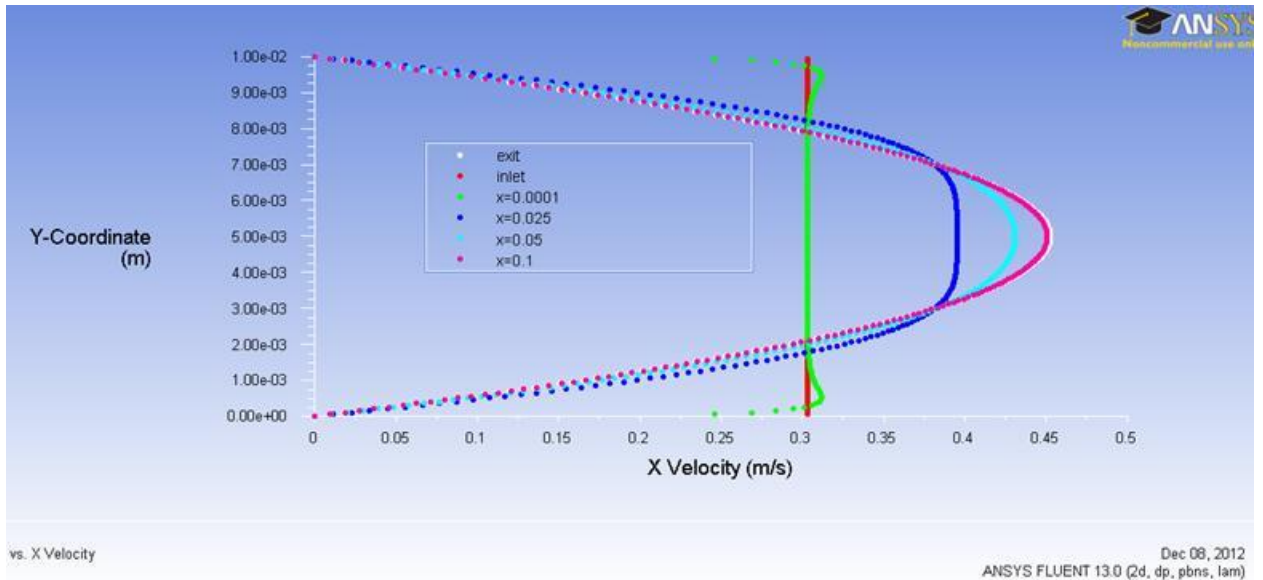


Figure 6-22 : Velocity profiles at different locations for a channel flow

In the picture above, the velocity profile starts developing right at the entrance of the pipe, and develops into a fully developed flow. The solution is as expected $U_{avg} = 2/3 * u_{max} = 2/3 * 0.45 = 0.3$ m/s. The velocity profile at $x=0.1$ m is compared to an ideal profile of a fully developed flow. The Max error % in this case is 1.53%. The max %error decreased from 3.528% to 1.53% with the increase in mesh density.

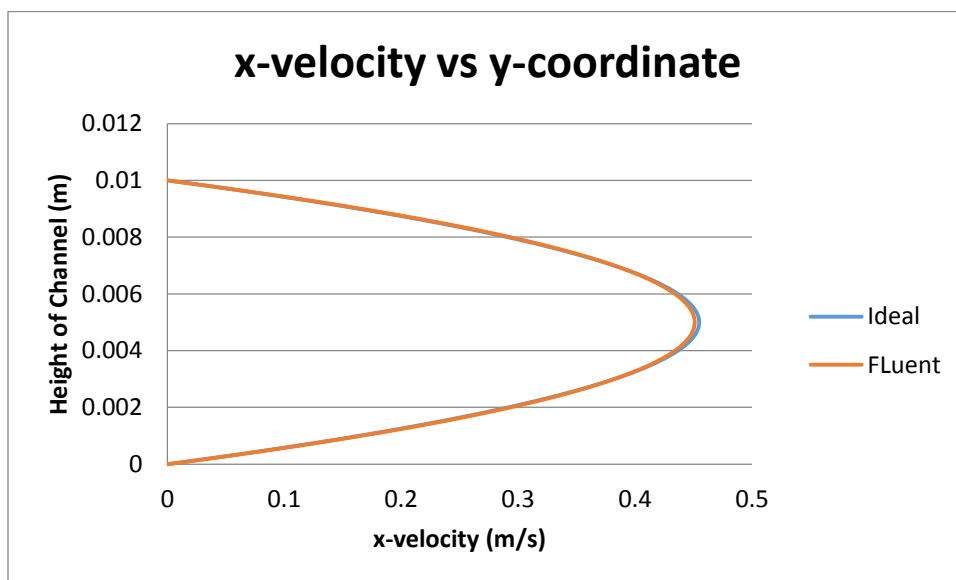


Figure 6-23 : Comparison of theoretical velocity profile with the one from Fluent

Fig 5.11 shows the comparison of ideal velocity profile and Fluent's velocity profile at $x=0.1$ meters. The accuracy increased with the increase in mesh density (after lowering the convergence criteria).

As expected, the skin friction coefficient remains constant once the flow becomes fully developed.

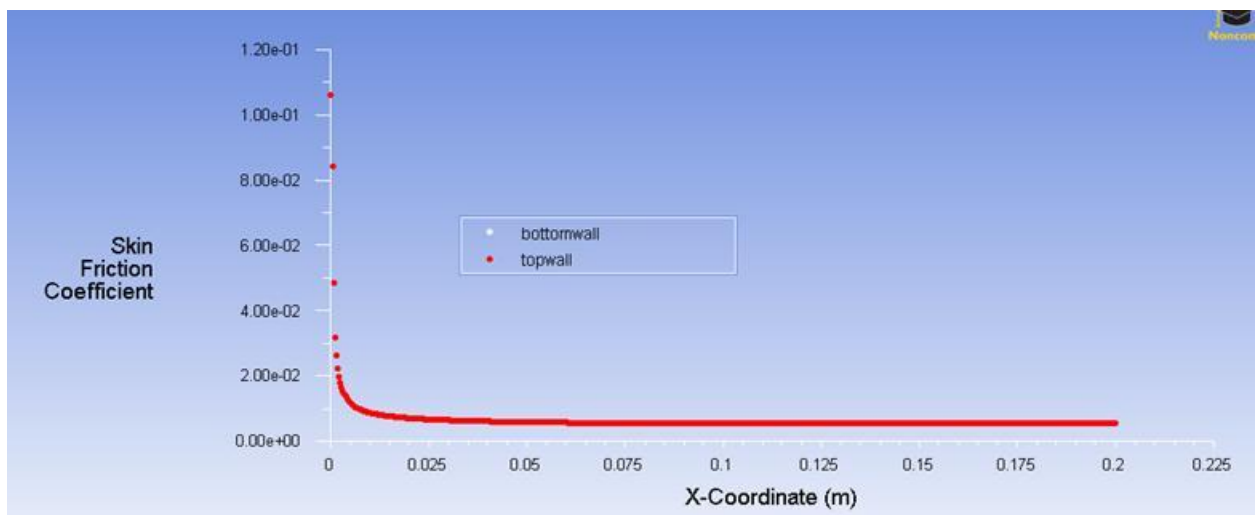


Figure 6-24 : Skin Friction Coefficient

The skin friction remains constant after $x=0.1$. This is where boundary layers meet.

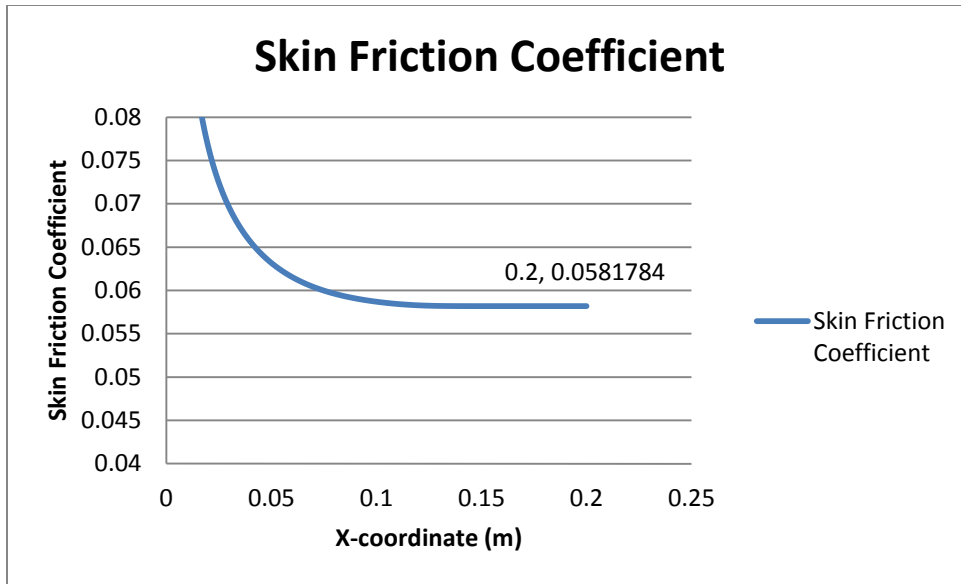


Figure 6-25 : A close look at the skin friction coefficient.

Skin Friction coefficient is a non-dimensional parameter defined as the ratio of wall shear stress and the reference dynamic pressure

$$Cf = \frac{\tau_w}{\frac{1}{2} \rho_{ref} (V_{ref})^2}$$

A higher skin friction coefficient is usually expected for low Reynold's number because the viscous forces are still prominent as compared to the inertial forces. However our mesh is not dense enough at the region close to the wall to fully capture the skin friction.

Iteration 3: Iteration 2 with increased convergence criteria

The absolute convergence criteria was increased to 10^{-8} and ran the analysis in fluent. The error of 1.49% was seen which is a small improvement from the previous Iteration with the convergence criteria of 10^{-6} .

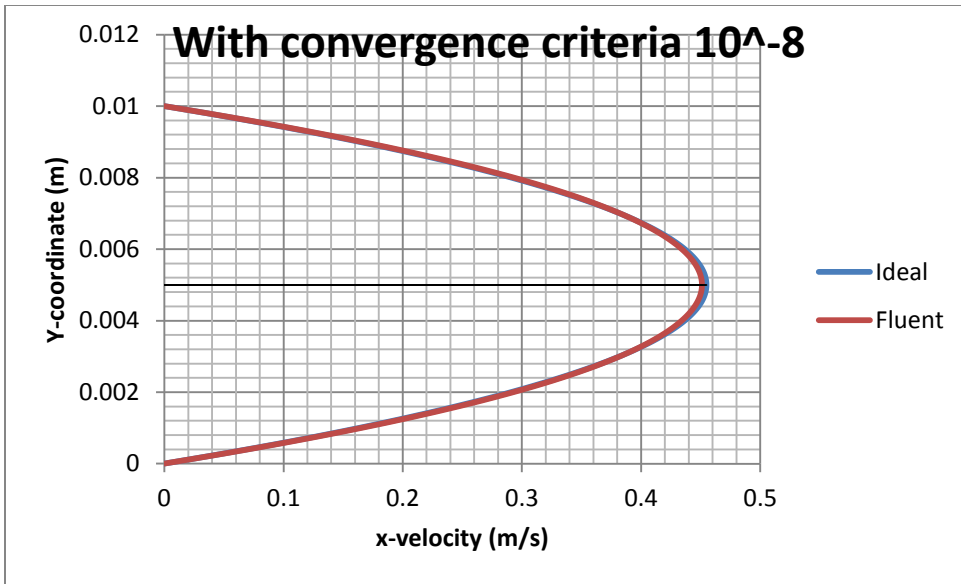


Figure 6-26 : Comparison with Ideal case for velocity profile

Fig: Comparing velocity profiles from fluent with the Ideal profiles, with refined mesh and very small convergence criteria for momentum and velocity.

A closer look at the skin friction coefficient at this point gives us the following results:

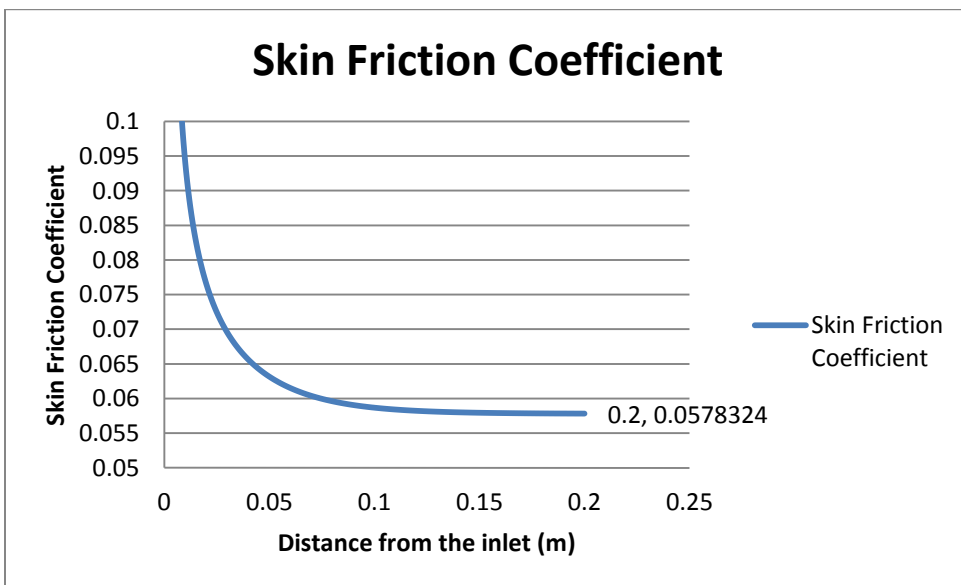


Figure 6-27 : Skin Friction Coefficient of $f = 0.057$ was found.

Because of these differences, a detailed study on f vs. convergence criteria was performed as follows:

Convergence Criteria	Skin friction coefficient
10^{-2}	0.176441
10^{-3}	0.100277
10^{-4}	0.073643
10^{-5}	0.0607
10^{-6}	0.0582
10^{-8}	0.057

Table 1 : Convergence criteria with skin friction coefficient

In General the skin coefficient was found to decrease with the decrease in convergence criteria. Since it stops decreasing much after reaching 10^{-6} , it is concluded that the value of skin friction coefficient of a fully developed flow must be close to 0.057. The skin friction coefficient is much lower than the expected value of 0.32. One of the reasons for this can be the fact that our mesh is not thin enough to fully capture the skin friction coefficient near the walls.

2.1: Steady, Laminar Flow in Circular Tubes and no Heat source.

Steady and laminar flow through circular tubes are commonly known as Poiseuille Flow. They are one of the most commonly studied flows by undergraduates. Fluent is used to solve the laminar pipe flow in circular tubes, and is compared with analytical solutions found by solving Navier-Stokes equations.

Problem Statement:

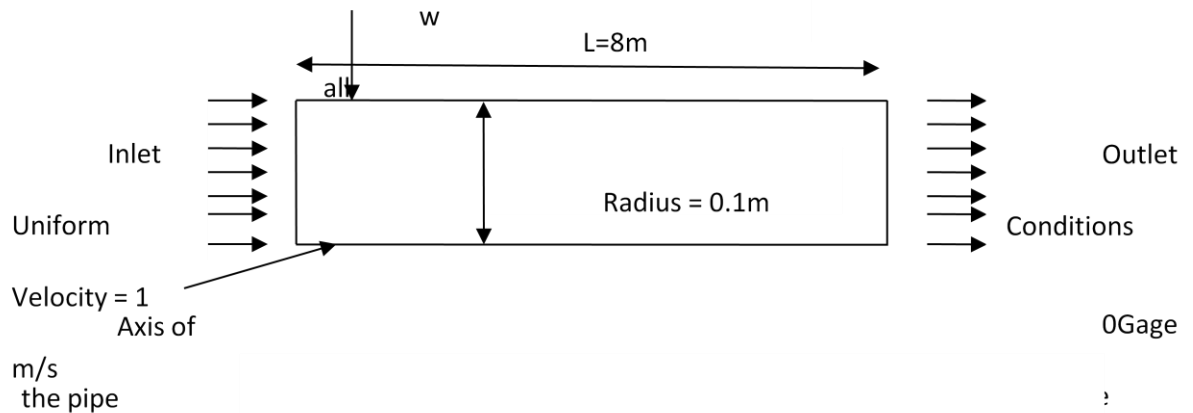


Figure 6-28 : Channel Flow with Boundary Conditions

The inlet condition is uniform velocity of 1 m/s which corresponds to the Reynolds's number of 200 for a fluid with the below mention properties. There is no temperature change throughout the system; hence the energy equation is turned off. In solving laminar flow, fluent uses two distinct equations to solve for energy and momentum. The energy equation is turned off. The outlet condition is 0 gage pressure, so the pipe is exiting outside. The lower edge is made the axis and upper edge is made the wall.

Reynolds Number:

$$V_{max} = 2 * 1 \frac{m}{s} = 2 \frac{m}{s}$$

$$\rho = 1 \text{ kg/m}^3$$

$$\mu = 2 * 10^{-3} \frac{\text{kg}}{\text{m} * \text{s}}$$

$$Re = \frac{\rho V D}{\mu} = \frac{1 * 2 * 0.2}{2 * 10^{-3}} = 200 < Re_{cr} = 2300$$

The Flow is laminar.

Hydrodynamic Entry Length:

$$L_{h,laminar} = 0.05 Re D = 0.05 * 200 * 0.2 = 2 \text{ m}$$

The velocity profile should converge at x=2m from the inlet.

Analytical Solution:

Navier-Stokes equations is solved to solve this Flow problem. The Navier-Stokes equation (5-2,5-3,5-4) can be written in the form of cylindrical polar coordinates as follows:

$$\begin{aligned} & \rho \left(\frac{\partial v_r}{\partial t} + v_r \frac{\partial v_r}{\partial r} + \frac{v_\theta}{r} \frac{\partial v_r}{\partial \theta} - \frac{v_\theta^2}{r} + v_z \frac{\partial v_r}{\partial z} \right) \\ & = - \frac{\partial p}{\partial r} + \rho g_r + \mu \left(\frac{1}{r} \frac{\partial}{\partial r} \left(r \frac{\partial v_r}{\partial r} \right) - \frac{v_r^2}{r^2} + \frac{1}{r^2} \frac{\partial^2 v_r}{\partial \theta^2} - \frac{2}{r^2} \frac{\partial v_\theta}{\partial \theta} + \frac{\partial^2 v_r}{\partial z^2} \right) \quad (\text{r - direction}) \quad (5 - 12) \end{aligned}$$

$$\begin{aligned} & \rho \left(\frac{\partial v_\theta}{\partial t} + v_r \frac{\partial v_\theta}{\partial r} + \frac{v_\theta}{r} \frac{\partial v_\theta}{\partial \theta} - \frac{v_r v_\theta}{r} + v_z \frac{\partial v_\theta}{\partial z} \right) \\ &= -\frac{1}{r} \frac{\partial p}{\partial \theta} + \rho g_\theta + \mu \left(\frac{1}{r} \frac{\partial}{\partial r} \left(r \frac{\partial v_\theta}{\partial r} \right) - \frac{v_\theta^2}{r^2} + \frac{1}{r^2} \frac{\partial^2 v_\theta}{\partial \theta^2} + \frac{2}{r^2} \frac{\partial v_r}{\partial \theta} + \frac{\partial^2 v_\theta}{\partial z^2} \right) \quad (\theta - \text{direction}) \quad (5 - 13) \end{aligned}$$

$$\begin{aligned} & \rho \left(\frac{\partial v_z}{\partial t} + v_r \frac{\partial v_z}{\partial r} + \frac{v_\theta}{r} \frac{\partial v_z}{\partial \theta} - \frac{v_\theta^2}{r} + v_z \frac{\partial v_z}{\partial z} \right) \\ &= -\frac{\partial p}{\partial z} + \rho g_z + \mu \left(\frac{1}{r} \frac{\partial}{\partial r} \left(r \frac{\partial v_z}{\partial r} \right) + \frac{1}{r^2} \frac{\partial^2 v_z}{\partial \theta^2} + \frac{\partial^2 v_z}{\partial z^2} \right) \quad (z - \text{direction}) \quad (5 - 14) \end{aligned}$$

Assuming that the direction of the flow is perpendicular to the inlet, i.e. in z direction, steady axisymmetric flow, the Navier-Stokes equation reduces to the following:

$$0 = -\frac{\partial p}{\partial r} - \rho g \sin\theta \quad (5 - 15)$$

$$0 = -\frac{1}{r} \frac{\partial p}{\partial \theta} - \rho g \sin\theta \quad (5 - 16)$$

$$0 = -\frac{\partial p}{\partial z} + \mu \left(\frac{1}{r} \frac{\partial}{\partial r} \left(r \frac{\partial v_z}{\partial r} \right) \right) \quad (5 - 17)$$

Integrating and solving the differential equations with the boundary conditions (wall velocity 0, and finite velocity in the center), the following equation is obtained for velocity distribution.

$$u = -\frac{1}{4\mu} \frac{dp}{dz} (r^2 - R^2) \quad (5 - 18)$$

Thus the velocity distribution of a fully developed flow is parabolic. Further integration and simplification just like the one in the case of Laminar flow results in the following equation for maximum velocity.

$$\frac{V_z}{V_{max}} = 1 - \left(\frac{r}{R}\right)^2$$

The velocity Profile of a fully developed laminar flow is given by

$$u(r) = 2 V_{avg} \left(1 - \frac{r^2}{R^2}\right) \quad (5 - 19)$$

This velocity profile is compared to the profile obtained from Fluent to verify Fluent's solution.

Equations used by Fluent:

For 2-D axisymmetric flow, the continuity equation is given by:

$$\frac{\partial \rho}{\partial t} + \frac{\partial}{\partial x}(\rho v_x) + \frac{\partial}{\partial r}(\rho v_r) + \frac{\rho v_r}{r} = S_m$$

The momentum conservation is given by:

$$\begin{aligned} \frac{\partial}{\partial t}(\rho v_x) + \frac{1}{r} \frac{\partial}{\partial x}(r \rho v_x v_x) + \frac{1}{r} \frac{\partial}{\partial r}(r \rho v_r v_x) = -\frac{\partial p}{\partial x} + \frac{1}{r} \frac{\partial}{\partial x} \left[r \mu \left(2 \frac{\partial v_x}{\partial x} - \frac{2}{3} (\nabla \cdot \vec{v}) \right) \right] \\ + \frac{1}{r} \frac{\partial}{\partial r} \left[r \mu \left(\frac{\partial v_x}{\partial r} + \frac{\partial v_r}{\partial x} \right) \right] + F_x \end{aligned}$$

And

$$\begin{aligned} \frac{\partial}{\partial t}(\rho v_r) + \frac{1}{r} \frac{\partial}{\partial x}(r \rho v_x v_r) + \frac{1}{r} \frac{\partial}{\partial r}(r \rho v_r v_r) = -\frac{\partial p}{\partial r} + \frac{1}{r} \frac{\partial}{\partial x} \left[r \mu \left(\frac{\partial v_r}{\partial x} + \frac{\partial v_x}{\partial r} \right) \right] \\ + \frac{1}{r} \frac{\partial}{\partial r} \left[r \mu \left(2 \frac{\partial v_r}{\partial r} - \frac{2}{3} (\nabla \cdot \vec{v}) \right) \right] - 2 \mu \frac{v_r}{r^2} + \frac{2}{3} \frac{\mu}{r} (\nabla \cdot \vec{v}) + \rho \frac{v_z^2}{r} + F_r \end{aligned}$$

Pipe Flow Iteration 1:

For a pipe flow problem, a very simplified problem is solved to verify our method.

Meshing:

The Mesh was created using ICEM CFD. It has 5 elements in the vertical lines and 100 elements in the horizontal lines. Total elements = 500. A coarse mesh was chosen on purpose to do a grid sensitivity study.

Results:

The solution was converged in 48 time steps. The convergence criteria was 10^{-6} for momentum and velocity. The axial velocity vs. the Y-coordinate looks as in the picture below. The V_{\max} is about 1.92 m/s. It is expected to be 2m/s.

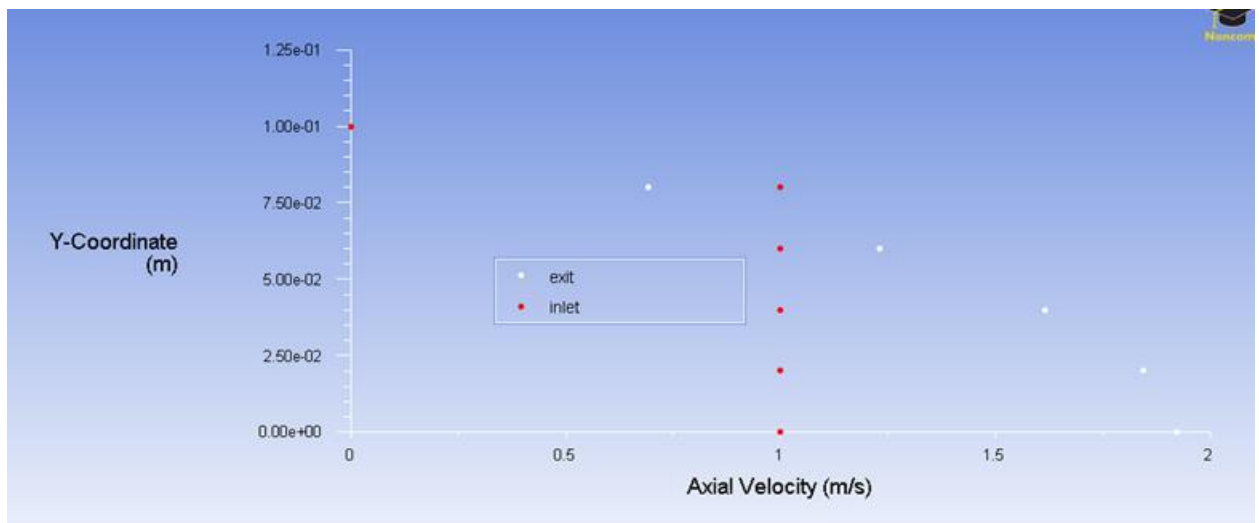


Figure 6-29 : Solution with only 500 elements

Iteration: 2 (Refined Mesh with the same boundary conditions and physical properties)

In this iteration, the mesh is refined, and the solution is compared with the coarse mesh's results.

10 elements on the inlet side, and 499 in the wall are added. The location of nodes was added based on geometric sequence with a ratio of 1.1.

Results:

Solution Converged in 40 time steps. The V_{\max} was about 1.95 m/s, a slight improvement.

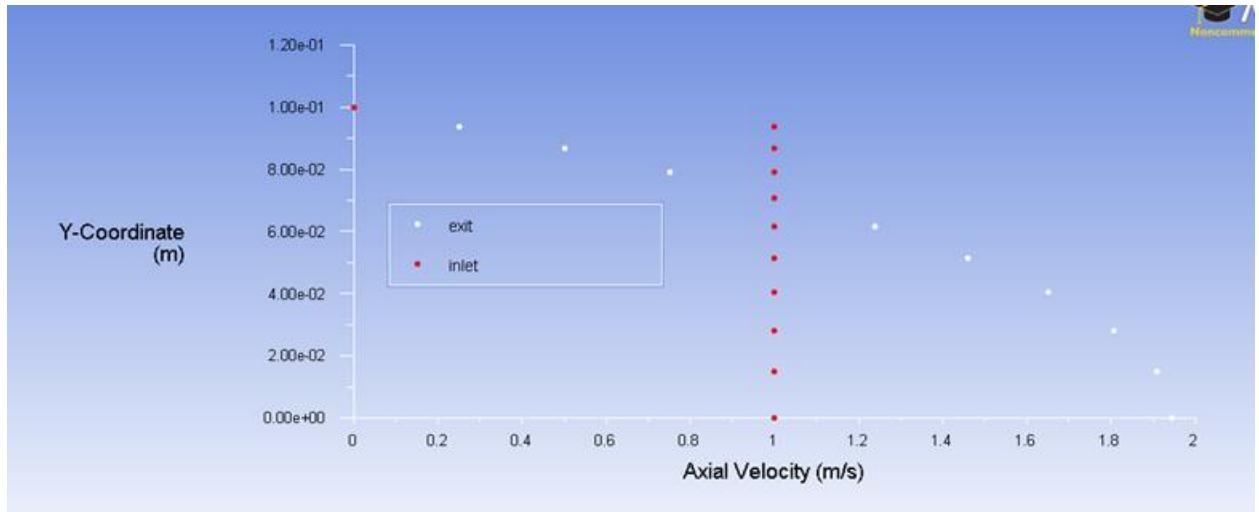


Figure 6-30 : Results from refined mesh

Iteration 3: (Same Mesh with our original problem Statement, different velocity)

Fluid Flowing through the Pipe (20 cm in diameter and 8 meters long) = air

Reynolds number is given by

$$Re_D = \frac{v D}{\nu}$$

Where, at Temperature = 20° C

$$v = \text{velocity of the fluid} = 0.015 \text{ m/s}$$

$$D = \text{Diameter} = 0.2 \text{ m}$$

$$\vartheta = \text{Kinematic Viscosity} = 1.516 * 10^{-5} \frac{m^2}{s}$$

Then,

$$Re_D = \frac{V * D}{\vartheta} = \frac{0.015 * 0.2}{1.516 * 10^{-5}} = 197.88 \cong 200 < Re_{critical, PipeFlow} = 2300$$

The Flow is laminar.

Hydrodynamic Entry Length:

$$L_{h,laminar} = 0.05 Re D = 0.05 * 197.88 * 0.2 = 1.979 m$$

The velocity profile should converge at x= 2m from the inlet.

Results:

Solution converged in 70 iterations. As expected, the solution converged and gave approximately close answer. The velocity profile will be compared to a curve obtained from analytical solution.

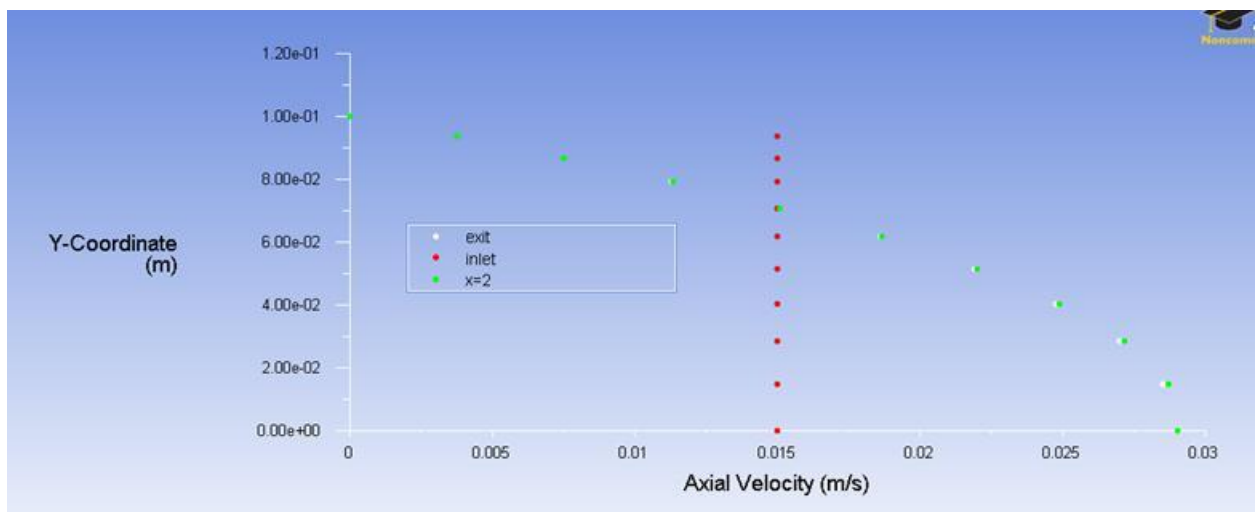


Figure 6-31 : Velocity Profile at inlet, exit and at x=2m

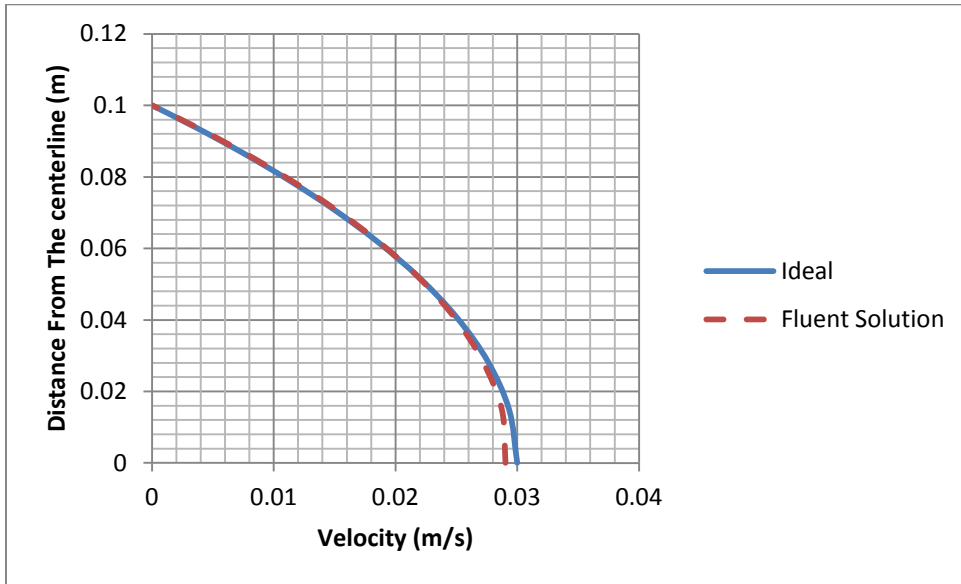


Figure 6-32 : Comparison of velocity Profile at x=2m with the Ideal velocity profile

The Maximum Error is 3.21%. Further mesh refinement will be done in the next part with constant temperature on the walls.

2.2.1: Pipe Flow with Laminar Flow and surface at a constant Temperature

Next consider a pipe, same geometry from above but has its outside surface temperature kept at a constant temperature. Consider air flowing through a pipe of diameter 1cm. The inlet temperature is 20 degree C, while the surface of the pipe is kept at a constant temperature of 90° C. The following figure explains the problem statement in more detail.

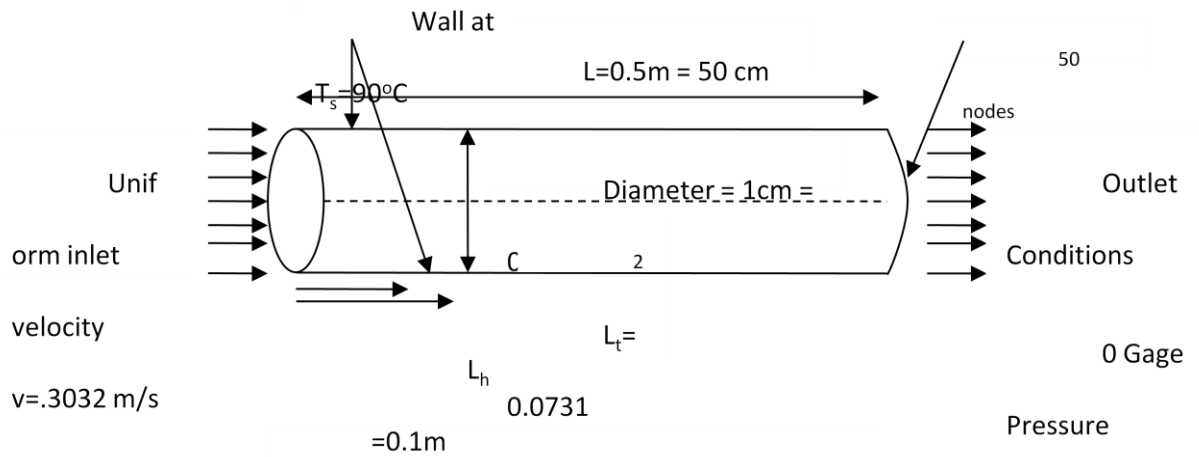


Figure 6-33 : Channel Flow with Boundary Conditions

Reynolds Number:

Reynolds number is given by

$$Re_D = \frac{vD}{\nu}$$

Where, at Temperature = 20° C

$$v = \text{velocity of the fluid} = 0.3032 \text{ m/s}$$

$$D = \text{Diameter} = 0.01 \text{ m}$$

$$\nu = \text{Kinematic Viscosity} = 1.516 \times 10^{-5} \frac{\text{m}^2}{\text{s}}$$

Then,

$$Re_D = \frac{v * D}{\nu} = \frac{0.3032 * 0.01}{1.516 * 10^{-5}} = 200$$

The Flow is laminar.

We expect the hydrodynamic boundary layer to converge at

$L_{h, \text{laminar}} = 0.05 \text{ Re } D = 0.08 * 200 * 0.01 = 0.1 \text{ m}$ and the thermodynamic boundary layer to converge at:

$L_{t, \text{laminar}} = 0.05 \text{ Re } \text{Pr } D = 0.05 * 200 * 0.731 * 0.01 = 0.0731 \text{ m}$

Meshing:

To mesh the axisymmetrical circular tube, only a very small part of the actual tube is modeled.

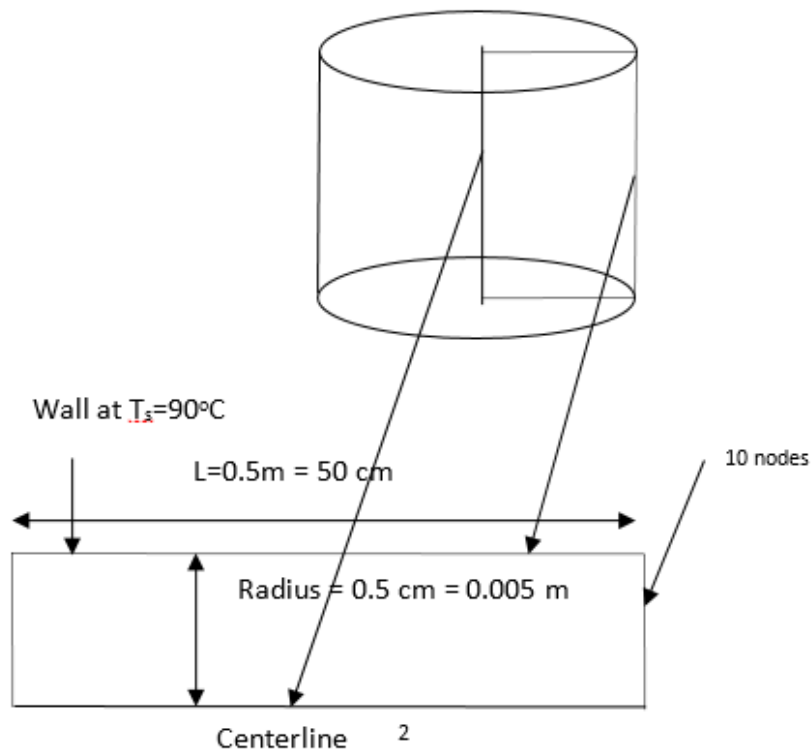


Figure 6-34 : Pipe Flow meshing

The mesh was created in CFD-ICEM. It had 10 nodes in the inlet/exit side and 130 nodes in the centerline/ top wall. The solution converged in 30 steps.

Solutions comparison:

Hydrodynamic entry length and velocity profile

The velocity profile of a fully developed flow is given by the equation

$$u(r) = 2 V_{avg} \left(1 - \frac{r^2}{R^2} \right)$$

Comparing the ideal velocity profile with the velocity profile at L_t the following curve is obtained:

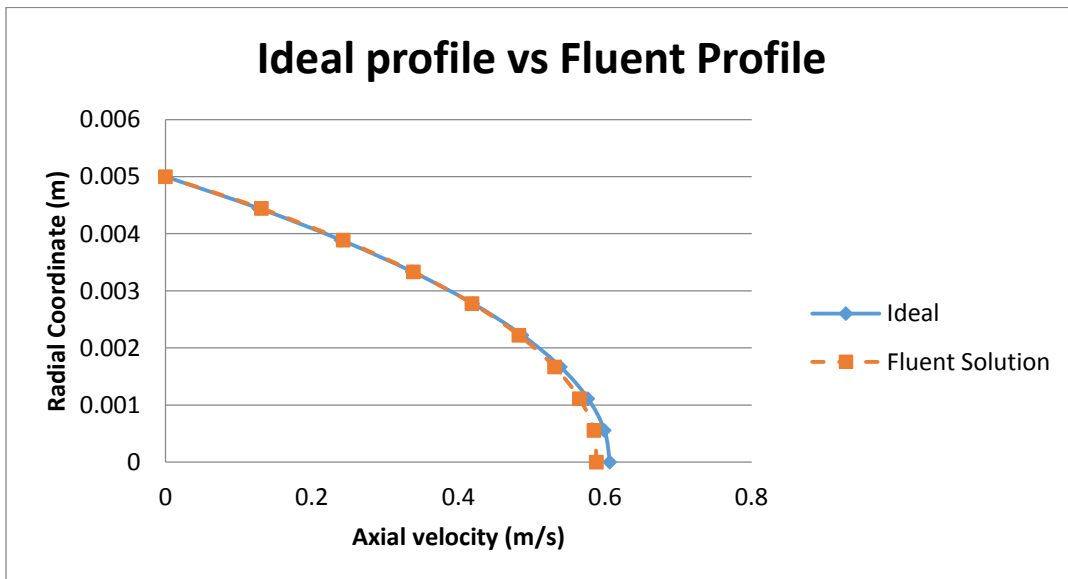


Figure 6-35 : Comparison of Ideal vs. Fluent's velocity Profile

Maximum error was 3.002 %.

The velocity profile of a fully developed flow (thermally) should remain the same after entry length. With temperature though, the temperature profile is found not from the actual temperature but from dimensionless time. The dimensionless time is defined as:

$$T_{\text{dimensionless}} = \frac{(T_s - T)}{T_s - T_m} \text{ where } T_s = \text{Surface Temperature,}$$

T = temperature

T_m = mean temperature at the cross section.

At the centerline, the temperature slowly increases with the distance to go up to $90^\circ \text{C} = 362^\circ \text{K}$.

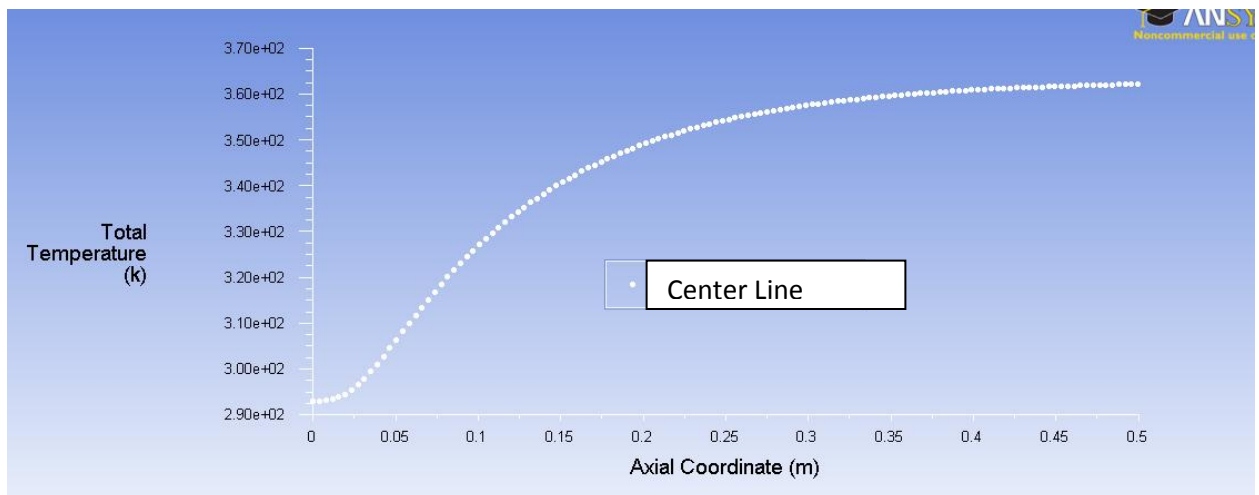


Figure 6-36 : Increasing Temperature

The temperature profile changes as follows:

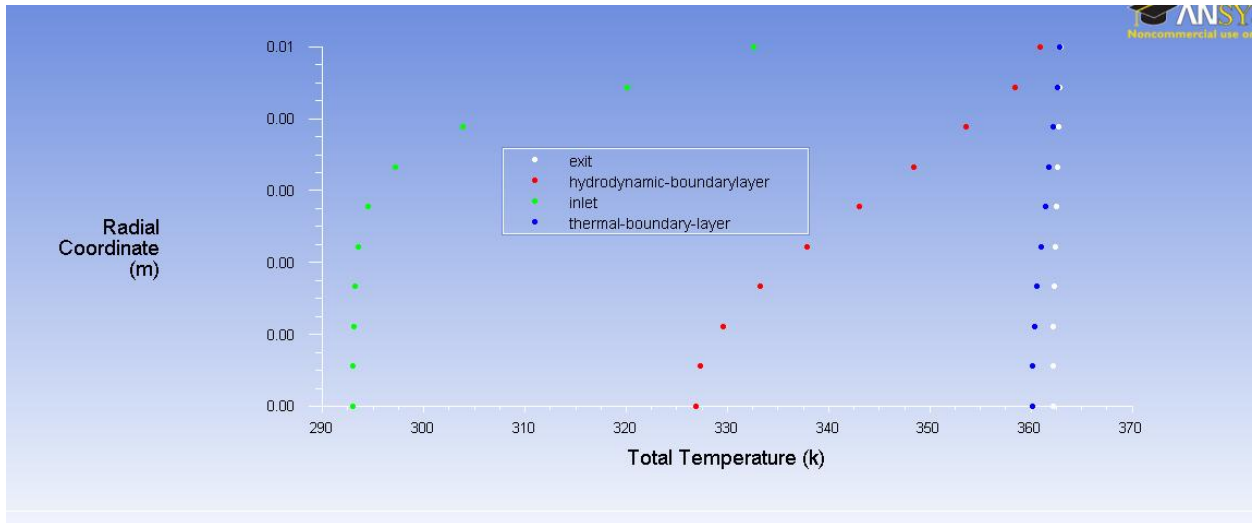


Figure 6-37 : Temperature Profiles

The temperature of the fluid changes only to get as closer to the surface temperature.

Nusselt's Number

Nusselt's number is defined as the ratio of heat convection over heat conduction.

Mathematically, $Nu = hL/k$

Where h = convective heat transfer coefficient

L = Diameter

K = thermal conductivity of the fluid.

In a circular tube, the Nusselt's number remains constant. For laminar flow in a circular tube, in the fully developed region, The Nusselts number is expected to be 3.66 when surface temperature is constant.

Skin Friction Coefficient

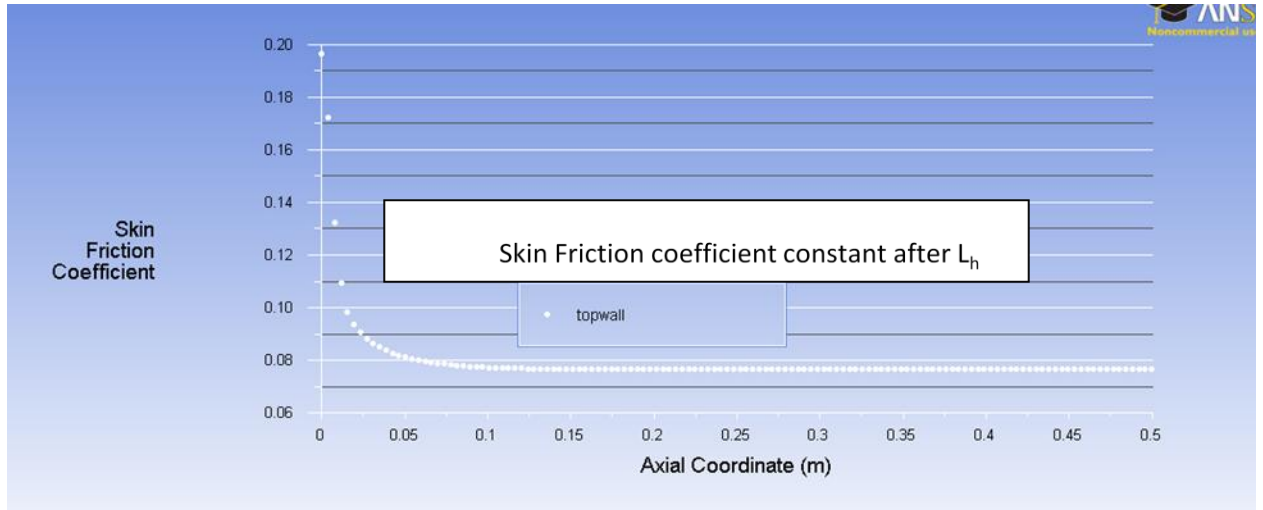


Figure 6-38 : Skin friction coefficient with Axial Coordinate

2.2.2: Pipe Flow with Laminar Flow and heat flux at the surface

Next, a much finer mesh is used for our last problem, and solved with constant heat flux applied on the surface of the pipe. The absolute convergence criterion was 10^{-6} for all momentum, velocity and energy.

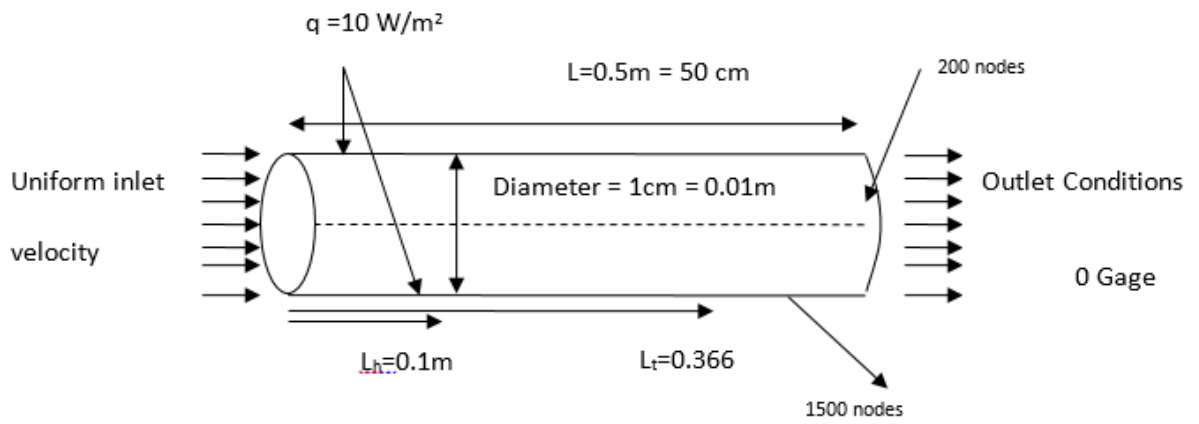


Figure 6-39 : Channel Flow with Boundary Conditions

Results:

Velocity Profile Developing:

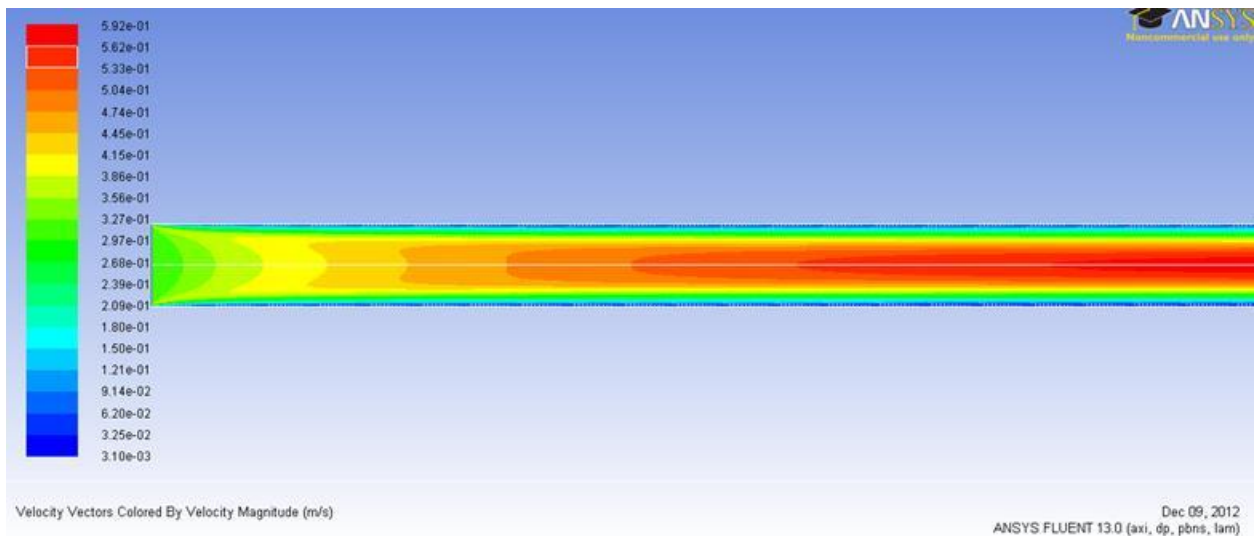


Figure 6-40 : Development of velocity profile

Comparison of Ideal velocity profile with the Fluent Solution

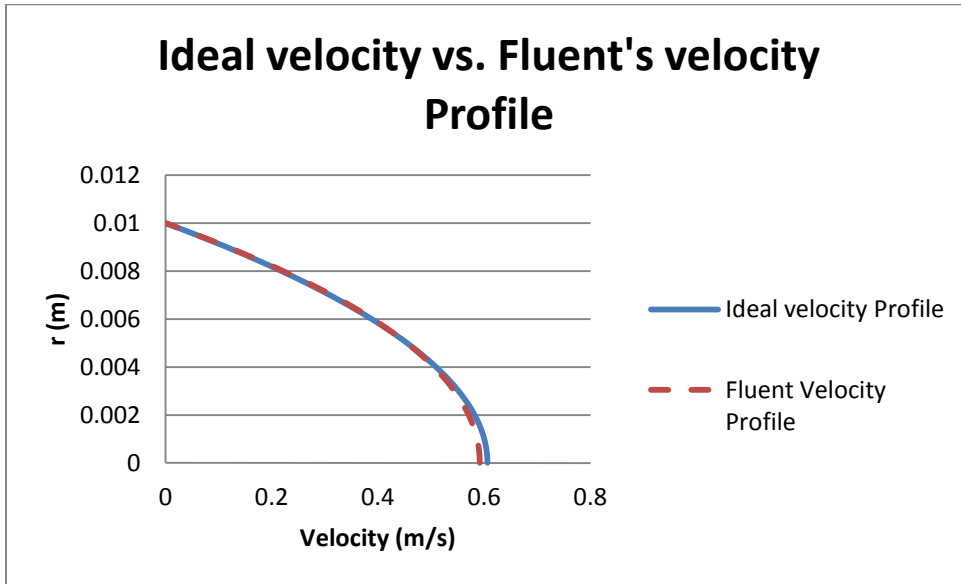


Figure 6-41 : Comparison of ideal vs. Fluent's velocity profile.

The max error % was 2.4%Skin Friction Coefficient

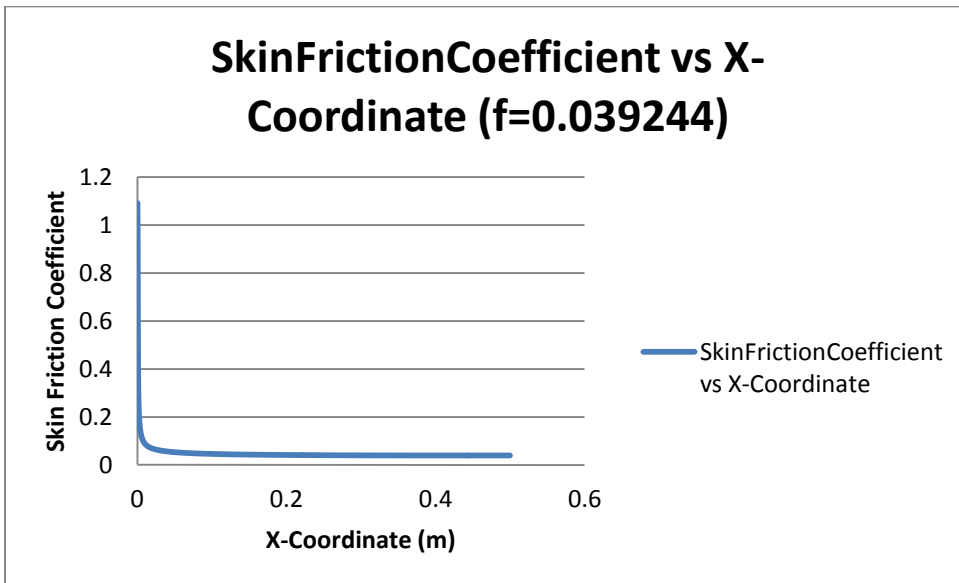


Figure 6-42 : Skin Friction Coefficient of 0.0392

Thermal Profile Developing:

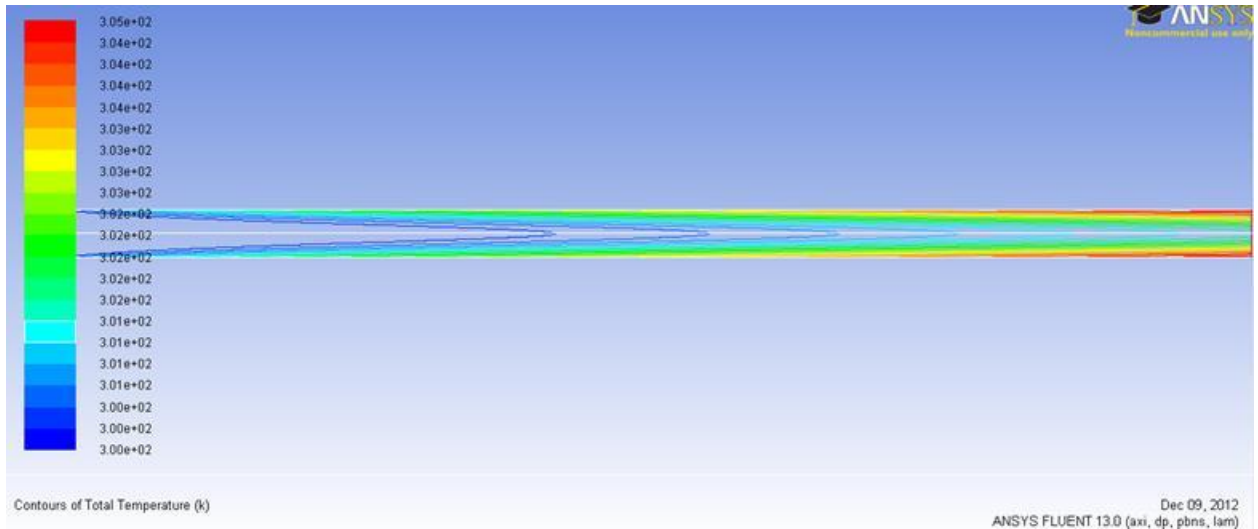


Figure 6-43 : Thermal Profile Developing

Constant heat flux is increasing the temperature of the fluid.

Comparison of Ideal thermal profile with the Fluent Solution

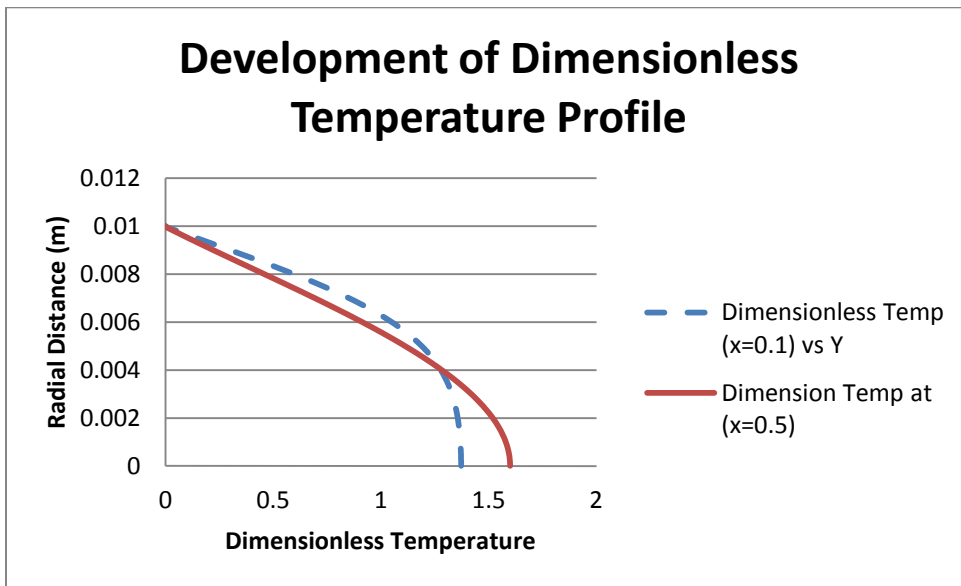


Figure 6-44 : Developing profile for Dimensionless Temperature

The profile of dimensionless Temperature is expected to be parabolic after being fully developed.

Nusselt's Number vs. increasing x-axis.

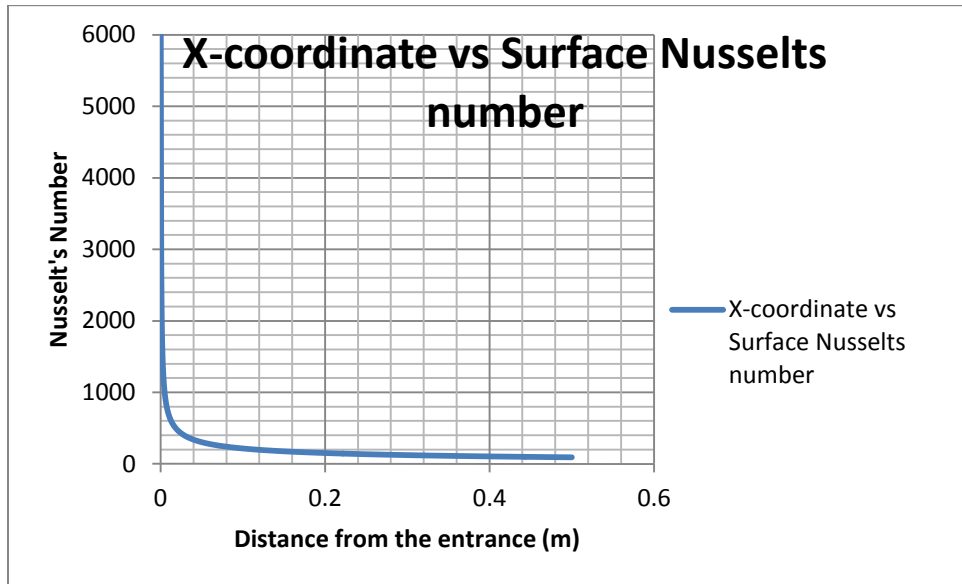


Figure 6-45 : Variation of surface Nusselt's number with the distance from the entrance.

The Nusselt's number is too high (94) and it was not constant even at the end of the pipe (0.5 meters). From talking to the ANSYS support, it was found out that it is because of the reference temperature. Nusselts number was expected to be 4.36 for a constant surface heat flux.

3: Turbulent Pipe Flow with Constant Temperature on the walls

Reynold's number is defined as the ratio of inertial forces to the viscous forces. In high Reynold's numbers, the inertial forces are so high that the viscous forces cannot stop the liquid from having random and unpredictable movements, thus called turbulent. In pipe-flow problems a flow starts to

become turbulent after the Reynold's number reaches 2300. It becomes fully turbulent at Reynold's number 10,000.

Here the same problem as the pipe flow is used, by increasing the velocity to make it turbulent.

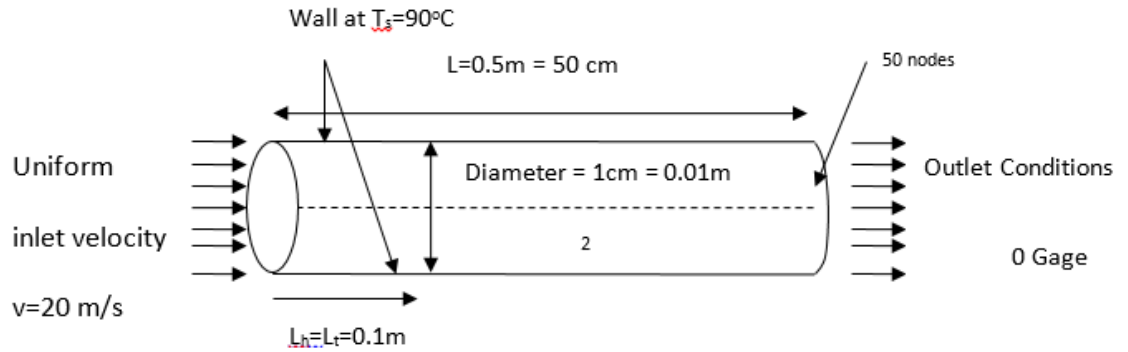


Figure 6-46 : Pipe Flow with Boundary Conditions

Reynolds number is given by

$$Re_D = \frac{vD}{\nu}$$

Where, at Temperature = 20°C

v = velocity of the fluid = 20 m/s

D = Diameter = 0.01 m

ν = Kinematic Viscosity = $1.516 \times 10^{-5} \frac{\text{m}^2}{\text{s}}$

Then,

$$Re_D = \frac{v * D}{\nu} = \frac{20 * 0.01}{1.516 * 10^{-5}} = 13192.6 > Re = 10000$$

So the Flow is Turbulent.

For Turbulent Flow, Both Hydrodynamic and thermal entry length is given by $L_t=L_h=10D=0.1m$.

A fluent model was ran to look at the entry length and study how the velocity profile changes.

Theory of fully developed turbulent velocity profile:

A fully developed turbulent flow in a pipe can be broken into three different sub-layers

(Munson):

Viscous sub layer is very close to the pipe wall and has a very dominant viscous shear stress. The second layer is overlap region, and the third region is the outer region. In the outer region, turbulent stress is dominant, while the overlap region is the region where the stress transforms from viscous to turbulent. In the analysis of the turbulent flow, viscosity is very important in the viscous sub layer while density of the flow is important in the outer layer.

The velocity profile is different in the viscous sub layer and the outer region. In viscous sublayer, the velocity profile can be written in dimensionless form as

$$\frac{\bar{u}}{u^*} = \frac{yu^*}{\nu} \quad (5 - 20)$$

Where, $y=R-r$ is the distance from the wall, \bar{u} is the time-averaged x-component of velocity and $u^* = (\tau_w/\rho)^{1/2}$ is the friction velocity. Equation (5-20) is commonly known as the *law of the wall*.

In the Overlap region, the velocity is given by the relation

$$\frac{\bar{u}}{u^*} = 2.5 \ln\left(\frac{yu^*}{\nu}\right) + 5.0 \quad (5 - 21)$$

Similarly, the velocity in the outer region is given by the following expression:

$$\frac{V_c - \bar{u}}{u^*} = 2.5 \ln \left(\frac{R}{y} \right) \quad (5 - 22)$$

Another common way to define the velocity profile in a turbulent flow is

$$\frac{\bar{u}}{V_c} = \left(1 - \frac{r}{R} \right)^{\frac{1}{n}} \quad (5 - 23)$$

$n=7$ is a commonly accepted value to define the velocity profile for turbulent flows. It needs to be clear that the equation 5-23 does not precisely tell us velocity near the walls and at the center line, however the approximate values are accepted.

The figure below clearly shows the difference between the laminar and turbulent flow in a pipe. The velocity profile of the turbulent flow is much blunt towards the center.

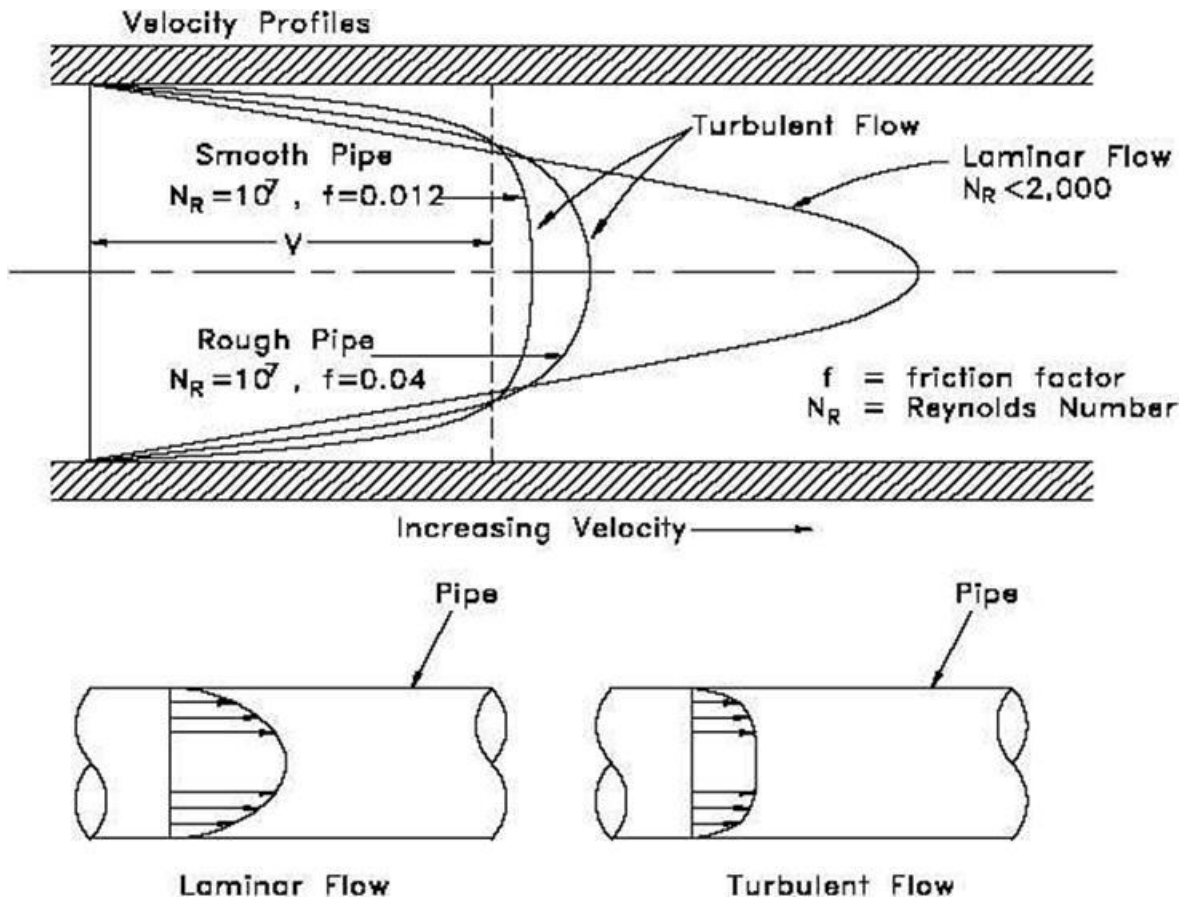


Figure 6-47 : Comparison of velocity profile in laminar and turbulent flow.

Fluent's Equations to solve turbulent Model (k-epsilon model)

k-epsilon model was used to solve the turbulent flow in the CFD training. K-epsilon method is known to be robust, economic and reasonably accurate for a wide range of turbulent flows, and is very popular in the research and industrial applications. K-epsilon model is based on model transport equations for turbulence kinetic energy(k) and its dissipation rate(ϵ). This model assumes that the flow is fully turbulent and the effects of molecular viscosity are negligible. Thus the k-epsilon model is valid only for fully turbulent model. Our flow had Reynolds number of 10000, making the flow fully turbulent.

Transport Equations for the Standard k-epsilon model:

The turbulence kinetic energy k , and its rate of dissipation ϵ are obtained from the following transport equations in Fluent (Fluent theory guide)

$$\frac{\partial}{\partial t}(\rho k) + \frac{\partial}{\partial x_i}(\rho k u_i) = \frac{\partial}{\partial x_j} \left[\left(\mu + \frac{\mu_t}{\sigma_k} \right) \frac{\partial k}{\partial x_j} \right] + G_k + G_b - \rho \epsilon - Y_M + S_k$$

and

$$\frac{\partial}{\partial t}(\rho \epsilon) + \frac{\partial}{\partial x_i}(\rho \epsilon u_i) = \frac{\partial}{\partial x_j} \left[\left(\mu + \frac{\mu_t}{\sigma_\epsilon} \right) \frac{\partial \epsilon}{\partial x_j} \right] + C_{1\epsilon} \frac{\epsilon}{k} (G_k + C_{3\epsilon} G_b) - C_{2\epsilon} \rho \frac{\epsilon^2}{k} + S_\epsilon$$

Where G_k, G_b represents the generation of turbulence kinetic energy due to the mean velocity gradients and due to buoyancy respectively. Y_m represents the contribution of the fluctuating dilations in compressible turbulence to the over dissipation rate. C 's are constants and σ 's are turbulent Prandtl numbers. S_k and S_ϵ are the user defined source terms.

Meshing: The same model as above with 10 nodes in the inlet and outlet and 150 nodes in the horizontal line was used.

Solution Comparison:

Velocity Profile at different locations is plotted.

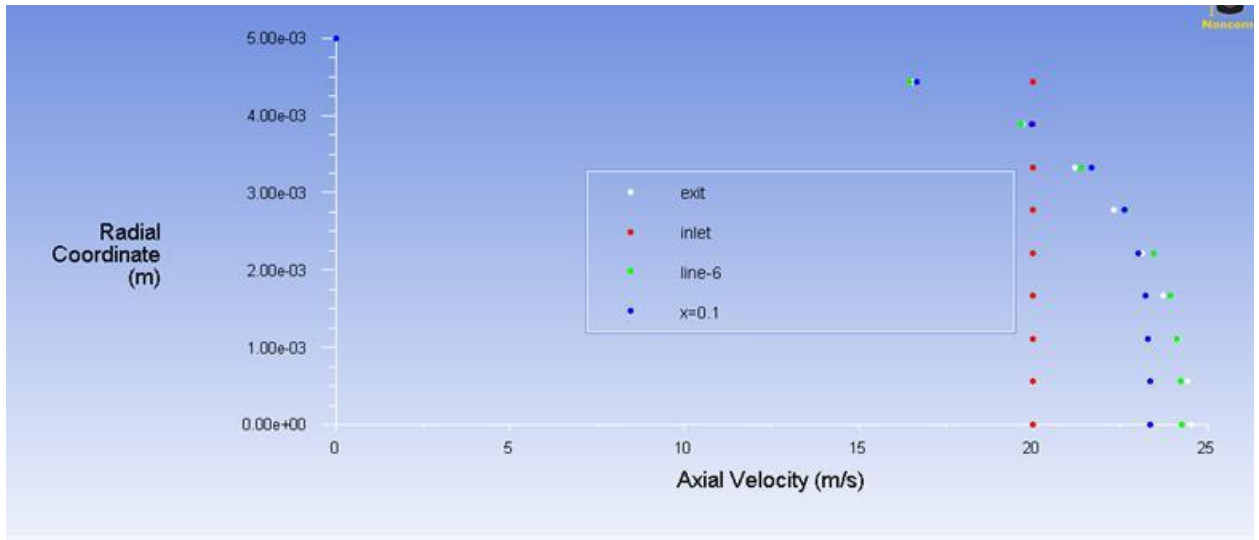


Figure 6-48 : Velocity Profiles of a turbulent Flow

The velocity profiles at different locations look about expected. The profiles of turbulent flow are known to have nearly a straight line at the core region, and have significant velocity gradient in the viscous sub layer.

Skin Friction Coefficient:

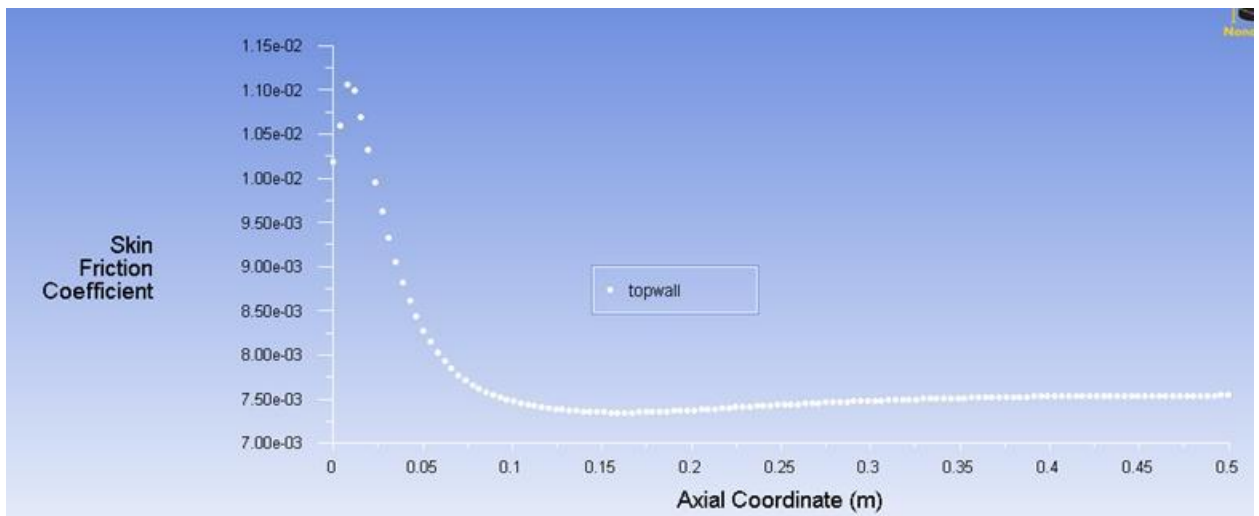



Figure 6-49: variation of Skin Friction Coefficient in turbulent flow

The curve for skin friction coefficient doesn't look very convincing, as it doesn't remain constant after the hydrodynamic boundary layers meet. This is mainly because the mesh is not dense enough to properly capture the skin friction near the wall. A denser mesh, or proper wall function should be used closer to the wall in the future.

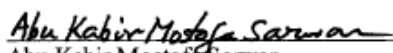
APPROVAL SHEET

This is to certify that Krishna Regmi has successfully completed his Senior Honors Thesis, entitled:

Investigation of Perforated Ducted Propellers to use with a UAV

 _____ Director of Thesis
Ting Wang

 _____ for the Department
Martin J. Guillot

 _____ for the University
Abu Kabir Mostofa Sarwar Honors Program

May 3, 2013
Date